POLITECNICO
MILANO 1863

SCUOLA DI INGEGNERIA INDUSTRIALE
E DELL'INFORMAZIONE

Preliminary development of a modelling framework for the prediction of hydro-abrasive wear in Pelton turbines.

Tesi di Laurea Magistrale in
Mathematical Engineering - Ingegneria Matematica

Author: **Laura De Giorgi**

Student ID: 10572776
Advisor: Prof. Gianandrea Vittorio Messa
Academic Year: 2022-23

Abstract

This thesis focuses on the hydro-abrasive wear of Pelton turbines working with sediment-laden water, which represents a significant issue in hydro-power plants. As a result of erosion, machinery could break down, and repair would be extremely expensive. Being able to estimate the useful lifetime of hydro-turbines operating in a sediment-laden environment could improve machine design and maintenance strategies. Since conducting experiments on real-scale devices is unfeasible, and open field data are scarce and often incomplete, the computer simulation, possibly complemented by a validation with respect to experiments on scaled prototypes, appears a valuable approach for the characterization of wear in hydro-turbines. However, the development of a suitable CFD framework which could become a tool at disposal of engineers is a very challenging task. The present thesis aims at providing a first contribution towards this goal. The key features which make the modelling of hydro-abrasive wear of Pelton turbines particularly complex are identified and discussed. Then, the development of the CFD framework has started following a step-by-step approach in which the elements of complexity are introduced one at a time. In this context, two test cases have been addressed, related with the modelling of a sediment-laden water jet over a cross section of a Pelton blade, and the evaluation of the hydro-abrasive wear of the actual blade geometry. The results have been discussed in the light of the relevant physical processes and, as far as possible, compared with other numerical solutions reported in the literature.

Abstract in lingua italiana

Questa tesi si concentra sull'usura idro-abrasiva delle turbine Pelton che lavorano con acqua carica di sedimenti, che rappresenta un problema significativo nelle centrali idroelettriche. A causa dell'erosione, i macchinari potrebbero rompersi e la loro riparazione sarebbe estremamente costosa. Riuscire a stimare la vita utile delle turbine idroelettriche, in quanto operano in un ambiente carico di sedimenti, potrebbe migliorare la progettazione delle macchine e le strategie di manutenzione. Poiché la conduzione di esperimenti su dispositivi in scala reale non è fattibile e i dati in campo aperto sono scarsi e spesso incompleti, la simulazione al computer, eventualmente integrata da una convalida rispetto a esperimenti su prototipi in scala, appare un approccio valido per la caratterizzazione dell'usura nelle idroturbine. Tuttavia, lo sviluppo di un'adeguata struttura CFD che possa diventare uno strumento a disposizione degli ingegneri è un compito molto impegnativo. La presente tesi intende fornire un primo contributo in tal senso. Vengono identificate e discusse le caratteristiche principali che rendono particolarmente complessa la modellazione dell'usura idro-abrasiva delle turbine Pelton. Quindi, lo sviluppo del framework CFD è iniziato seguendo un approccio graduale in cui gli elementi di complessità vengono introdotti uno alla volta. In questo contesto, sono stati affrontati due casi test, relativi alla modellazione di un getto d'acqua carico di sedimenti su una sezione trasversale di una pala Pelton e alla valutazione dell'usura idro-abrasiva dell'attuale geometria della pala. I risultati sono stati discussi alla luce dei processi fisici rilevanti e, per quanto possibile, confrontati con altre soluzioni numeriche riportate in letteratura.

Contents

Abstract **i**

Abstract in lingua italiana **iii**

Contents **v**

1 Introduction **1**
1.1 The problem of erosion in hydraulic turbines . . . 1
1.2 Structure of a Pelton turbine . . . 3
1.3 Available investigation approaches . . . 7
1.3.1 Practical erosion correlations . . . 7
1.3.2 Laboratory Testing . . . 8
1.3.3 Numerical simulation . . . 10
1.4 Aims and structure of the thesis . . . 11

2 Challenges in the numerical simulation of turbine erosion **13**
2.1 Multi-physics nature of hydro-abrasive wear . . . 13
2.2 Multi-scale nature of hydro-abrasive wear . . . 14
2.3 Challenges in the fluid dynamic modelling . . . 16
2.3.1 Modelling of the turbulent flow . . . 16
2.3.2 Modelling of the water jet in air . . . 17
2.3.3 Modeling of the sediment-laden water jet . . . 18
2.4 Modeling of the jet-blade interaction . . . 19
2.5 Challenges in the solid mechanics modelling . . . 19
2.6 Characterization of the sediments . . . 21

3 Description of the mathematical models **23**
3.1 Modelling of the turbulent, single-phase flow . . . 23
3.1.1 The RANS equations . . . 24

3.1.2 The standard $k-\varepsilon$ turbulence model . . . 25
3.1.3 Notes on the other turbulence models employed . . . 26
3.2 Modelling of the turbulent, air-water flow . . . 26
3.3 Tracking of the trajectories of the sediments . . . 27
3.4 Erosion models . . . 29

4 Case study 1: particle-laden flow in a 2D model of a fixed Pelton blade 31
4.1 Submerged water jet (single-phase flow) . . . 32
4.1.1 CFD set up . . . 33
4.1.2 Physical consistency of the CFD solution . . . 35
4.1.3 Convergence assessment study . . . 35
4.1.4 Sensitivity to the turbulence model . . . 39
4.1.5 Comparison against literature results . . . 41
4.1.6 Conclusion . . . 45
4.2 Free water jet (two-phase flow) . . . 48
4.2.1 CFD set up . . . 48
4.2.2 Physical consistency of the CFD solution . . . 49
4.2.3 Convergence assessment study . . . 51
4.2.4 Sensitivity of the CFD results on modelling parameters. . . . 53
4.2.5 Comparison against literature results . . . 57
4.2.6 Conclusion . . . 59
4.3 Sediment-laden, free water jet (three-phase flow) . . . 61
4.3.1 Particle tracking model and procedure . . . 61
4.3.2 Physical consistency of the DPM solution and evaluation of the particle-wall impact statistics . . . 62
4.3.3 Sensitivity of the particle-wall impact statistics with respect to numerical parameters . . . 65
4.3.4 Conclusion . . . 70

5 Case study 2: hydro-abrasive wear of a Pelton blade 73
5.1 Blade geometry and testing conditions . . . 74
5.2 CFD set up . . . 76
5.2.1 Fluid dynamic models and simulation strategy . . . 76
5.2.2 Computational domain, boundary conditions, computational mesh, and other solution settings . . . 77
5.2.3 Calculation of the particle-wall impact statistics and of the hydro-abrasive wear . . . 79
5.3 Physical consistency of the numerical solution . . . 80

5.4 Convergence assessment study 83
5.4.1 Effect of the mesh on the particle-wall impact statistics 83
5.4.2 Effect of the number of particles on the particle-wall impact statistics 85
5.4.3 Effect of the mesh on the erosion predictions 87
5.4.4 Comparison against literature results 88
5.5 Conclusion 91

6 Concluding remarks and future developments **93**

Bibliography **97**

A Appendix A **99**

B Appendix B **109**

List of Figures **113**

List of Tables **117**

List of Symbols **119**

Acknowledgements **123**

1 | Introduction

The objective of this chapter is to identify the reasons why the hydro-abrasive wear in Pelton turbines is so relevant and should be further investigated. In the following sections, the problem is introduced by looking at the problem of hydroabrasive wear in turbines, with a focus on Pelton turbines and why this is still an open problem. In particular, in section 1.1 is introduced the problem and its importance, in section 1.2 is presented the structure of a turbine to define the parameters of the problem, in section 1.3 are presented the available investigation methods and finally in section 1.4 the aims and structure of the thesis.

1.1. The problem of erosion in hydraulic turbines

Hydropower takes a key role in the electricity production, as it accounts for 62% of global renewable energy [7]. However, most electricity generation is related to non-renewable energies which cause high greenhouse gas emissions. This in past years has brought to a 1.5° increase in global temperature, as well as a series of climate changes that have led to migrations due to food and water shortages. In addition, the demand for electricity is always increasing, for instance for the electrification of the transportation. Moreover, compared to other forms of renewable energy, hydropower is not intermittent so is available at all times of the day. In contrast, solar energy is intermittent as its availability depends on weather conditions. In addition, at the time of greatest demand, i.e. in the evening, it is not available, due to the lack of sunlight. And that is the reason why hydropower assumes a key role in the renewable energy production. An example of a hydroelectric plant is shown in Figure 1.1.

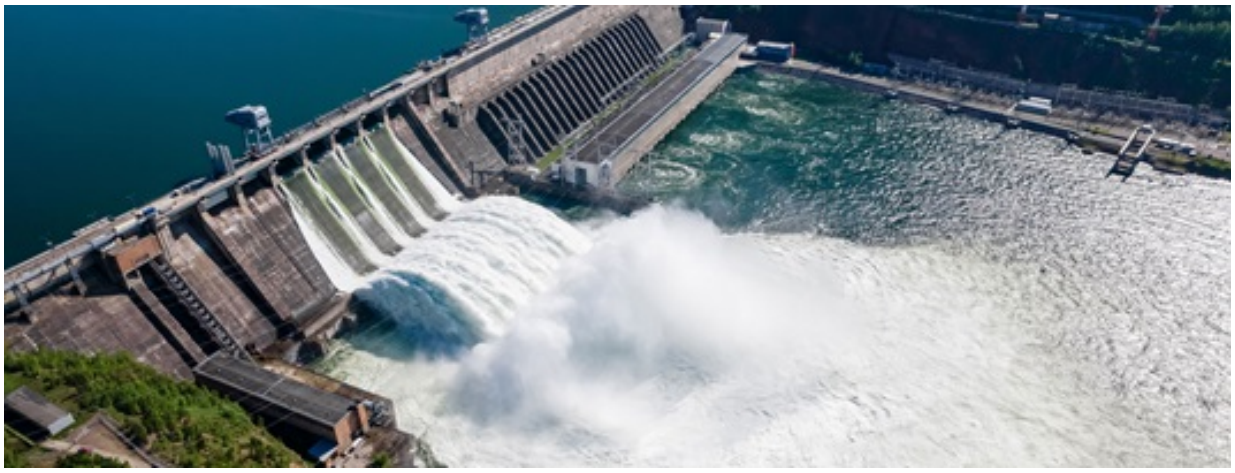

Figure 1.1: Irena hydropower plant in Abu Dhabi (picture from irena.org).

Based on the considerations above, it is not surprising to see that hydropower is a quite hot research topic. Particularly, studies are aimed at improving the efficiency of the technology through design optimization and process management. In this context, a major issue is the removal of material from vulnerable turbine components, such as and not limited to the blades, owing to the presence of sediment-laden water. This phenomenon is called hydro-abrasive wear, or impact erosion. In general, all turbines used in hydroelectric plants are subject to erosion due to the presence of sediments in the water, which cannot be completely removed. Consequently, this problem affects different types of turbines such as Francis Kaplan and Pelton. In this thesis This thesis focused on Pelton turbines, because, as pointed out by [7], the problem of hydro-abrasive wear is particularly relevant because most of the hydro-power plants are located in regions which are characterized by an elevated presence of sediments in the water to their relatively young geological formations. However, the blades of turbines are not exposed to large sediments as they can be removed either through reservoirs or sand traps. In fact, all sediments larger than about $300\mu m$ are removed from the system [7]. For this reason, small sediments will be considered in the discussion.

Hydro-abrasive wear produces structural damages to the turbine components, possibly leading to machinery breakdown. By way of example, in Figure 1.2, it is possible to see the effect of erosion on two blades of a Pelton turbine.

Figure 1.2: Process of erosion of a Pelton turbine blade. Different jet velocities, silt sizes and concentrations are considered in the two cases. The blade is shown at different time instants (picture from Ge et al. [5]).

Eventually, the process of hydro-abrasive erosion might produce failure of the turbine. Given that the cost of replacing the damaged components is extremely high, being able to estimate the useful lifetime of a hydro-turbines working in sediment-laden water would be definitely helpful to improve the design of the machines and develop strategies of scheduled maintenance of the plants. This requires being able to characterize the wear processes occurring in turbine components. However, running experimental on the wear failure of real machines is practically impossible, because of the large sizes and long time involved, resulting in high costs and technical issues. At the same time, it is not easy to conduct small-scale experiments in which the erosion process is accelerates, as this would result in similarity issues. The problem of erosion is therefore very complicated to analyse experimentally, but significant challenges arise also from the point of view of the numerical simulation. All aspects of complexity and ways to overcome them will be analysed in detail in the following sections.

1.2. Structure of a Pelton turbine

Among the different types of hydro-turbines, like Kaplan, Francis and Bulb, this thesis focuses on the Pelton turbine because Pelton turbines are widely used in regions such

as Himalayas, Andes, Alps and the Rocky Mountains where, due to their recent geological formation and the retreat of glaciers that imply a high formation of sediments, are particularly affected by the erosion phenomenon [7]. In particular they are used in the high mountains because they are suitable for high heads and low flow. Consequently, this phenomenon is very significant in this case.

Some examples of Pelton turbines can be found in Figure 1.3. In particular in Figure 1.3b it is show an example of Pelton turbine with more than one injector. The main feature of a Pelton turbine is the impeller-injector system, i.e. the system whereby a turbine is set in motion by the jet of water impinging on the turbine blades, and the work produced is converted into electrical energy. A broad description of a Pelton turbine is reported below. A sketch of its structure is represented in Figure 1.4.

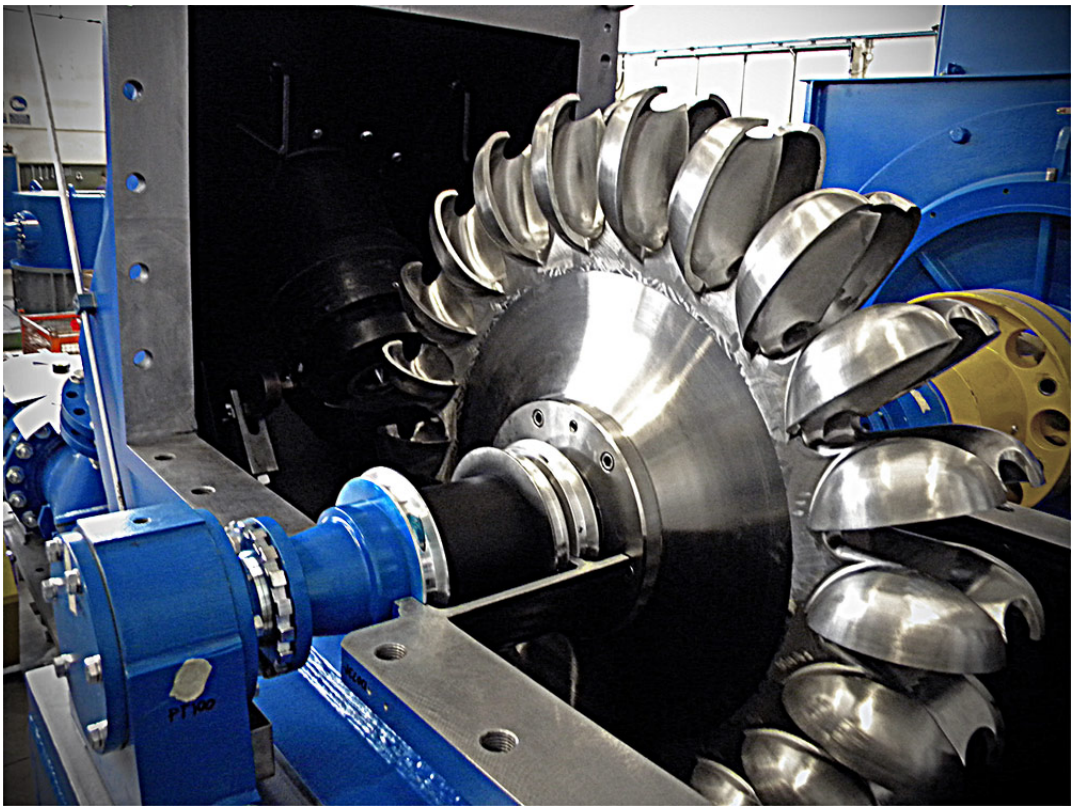

(a) Example of Pelton turbine (picture from Zeco Turbine zecohydropower.com).

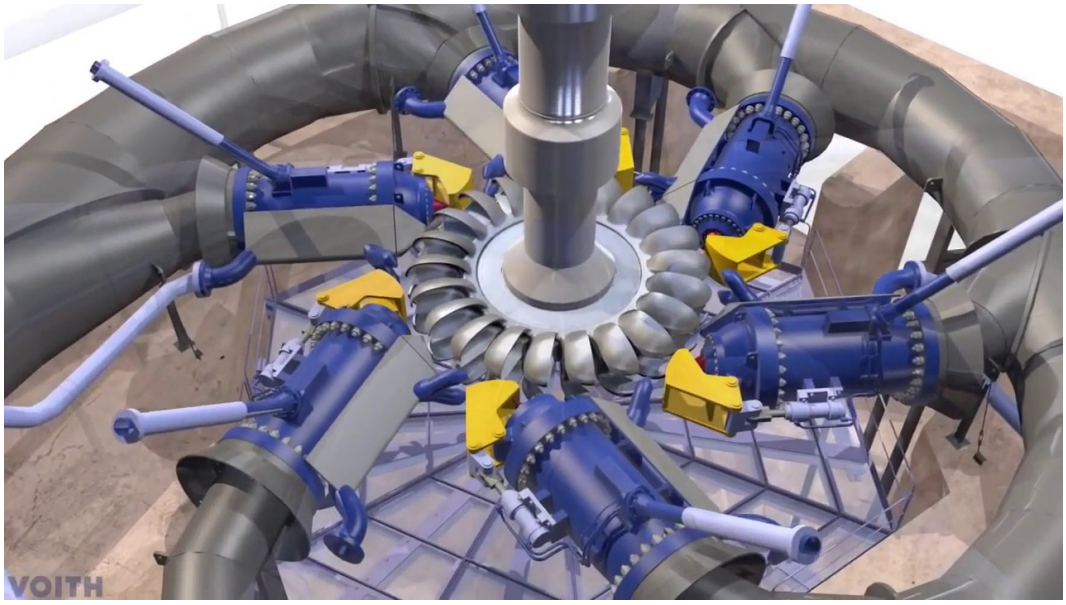

(b) Example of Pelton turbine with six injectors.

Figure 1.3: Examples of Pelton Turbines.

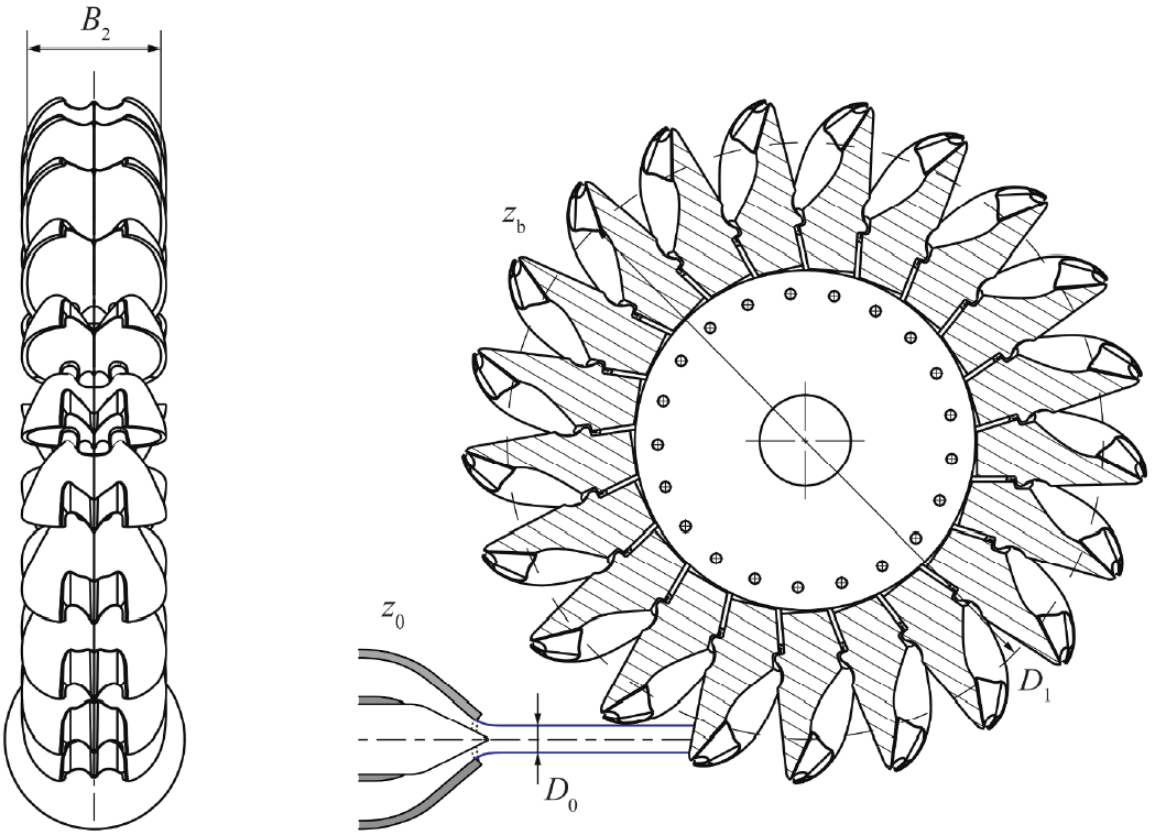

Figure 1.4: Pelton runner with one injector (picture from Leguizamon [7]).

.

Pelton runners are composed by a number of buckets z_b with characteristic size B_2, which is typically defined as the maximum internal width of a Pelton bucket. Then the buckets are impinged by a number of jets z_0(the number of jets) defined by a velocity C_1(the absolute jet bulk-mean velocity) and a diameter D_0. D_1 is the turbine pitch diameter to which the jet is tangent, as it seen in Figure 1.4. Specifically, the jet strikes the turbine blade, after which its direction is reversed. The thrust of the water sets the rotation of the turbine in motion. Some of the energy is dissipated in the impact, so the water will exit at a reduced speed as it exits the bucket as shown in Figure 1.5. In this way, the turbine is subject to a torque that is converted into mechanical energy.

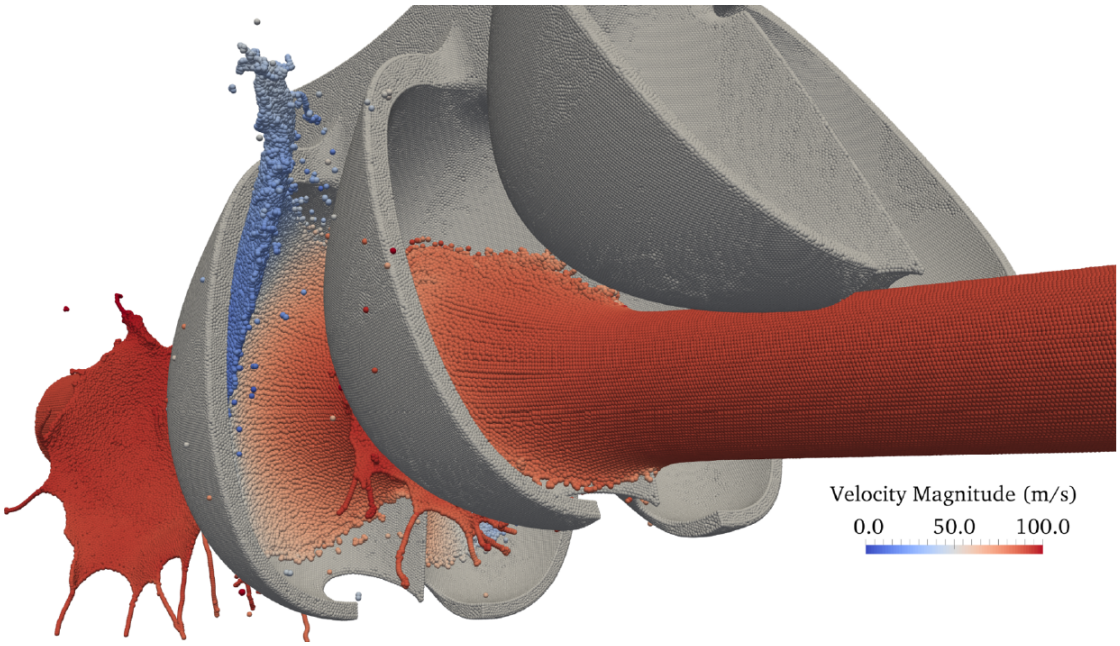

Figure 1.5: Impact jet on the blades of a rotating turbine (picture from Leguizamon [7]).

1.3. Available approaches for the characterization of hydro-abrasive wear in hydro-turbines

Several methods can be used to estimate erosion in Pelton turbines, as a necessary information for optimized design and management of hydropower systems. However, they suffer from a number of limitations and criticisms that severely limit their applicability, because to have erosion correlations that predict the case under analysis very accurately, there is a reduction in the applicability of these formulae to different contexts. On the other hand, to have erosion correlations that can be adapted to more contexts, there is a loss of accuracy in predicting erosion. The following section will explain strengths, weaknesses and challenges of the basic approaches for the characterization of hydro-abrasive wear of Pelton turbines.

1.3.1. Practical erosion correlations

A number of *erosion correlations* have been developed for the practical estimate of turbine wear in hydraulic turbines starting from a set of input parameters. These formulas are very simple from a mathematical point of view, thereby easy-to-use, but none of them is applicable to a wide set of conditions because they are very case-specific. According to Leguizamon et al. [7], 28 out of the many practical erosion correlations available are

applicable to Pelton turbines. By way of example, the erosion correlation proposed by Okamura and Sato [14] is:

$$\eta_m = (1 - 0.085C)\eta_w \tag{1.1}$$

where, η_m is the turbine peak efficiency with sediment laden flow, η_w is turbine peak efficiency with clean water and C is the fraction of solid by weight. As already remarked, the main issue of formulas like the above one is that no equation is general, but they are very case-specific and involve several empirical parameters that can be estimated only after a first erosion assessment. In particular all these parameters have to be experimentally determined. In conclusion, their advantages lie in their ease of use, while their disadvantages lie in the fact that, in order to have very precise erosion correlations, they lack applicability and are generally unreliable.

At this point, it is possible to go on to define erosion on the geometry under analysis. This is due to the combination of all the impacts that the particles exert on the blade, which involve the removal of material from the blade. At this point, as will be detailed in the 2.5, it is possible from the mass flow rate of removed material given by the individual impact to calculate the integral erosion ratio, i.e. the sum of all impacts occurring on a given cell divided by the mass flow rate.

1.3.2. Laboratory Testing

In order to explain how to predict the erosion through experiments it is necessary to define some parameters that represent the similarity between a reduced size and a full scale turbine. As a matter of facts, the large size of Pelton turbines makes it impossible to test the actual devices in a laboratory, but the experiments are conducted on a reduced-scale model. Therefore, in order to ensure that the prototype and the reduced-scale model have the same geometric structure and operate under the same flow conditions, relationships are defined that must be fulfilled [7].

As a consequence the objective is to predict the behavior of a prototype through a reduced scale model that is able to reproduce the same conditions. However, it is not possible for all these relationships to be satisfied at the same time. Moreover, even assuming that all similarity requirements are met, there are other problems in reducing the scale because a smaller model of 10-20 would require smaller particles, but the erosion is very different here because particles with different sizes have different energy content during impact at fixed velocity and the interaction with the turbulent flow is also different. For this reason,

a reduced-scale model will not be able to reproduce the same phenomenon.

In addition, the erosion wear is a slow process accentuated by the fact that in reduced scale models the velocities involved are lower, so the time required for the erosion process is even longer. Hence this method is not applicable both because it is not really possible to reproduce a small scale model that operates in the same way, both because the low velocity involved in reducing the scales imply that the time required for the experimental testing is too long.

Two examples of experimental setups are shown in Figures 1.6, 1.7.

Figure 1.6: An example of experimental setup for testing turbine erosion (picture from Ge et al. [5]).

Figure 1.7: Another example of experimental setup for testing turbine erosion (picture from Padhy [13]).

1.3.3. Numerical simulation

Another way to predict erosion is to carry out numerical simulations. This method is very useful in all cases when experiments are unfeasible, e.g. when the process considered is too slow or too long, or whenever it involves extremely small or large spatial scales.

In the specific case of Pelton turbines, the computer simulation allows virtual testing of the full scale prototype without the need of referring to a reduced scale model. In this way, the similarity issues highlighted in the previous section, e.g. those related with the reduction in sediment size, do not arise. In addition, the numerical simulation provides a lot of distributed information, in contrast with laboratory experiments which provide only a limited number of measurements at selected locations. However, there are also several issues associated with numerical simulations. The first one is that equations are approximate in nature. In fact, a set of equations relying only on the very physical principles would result in resulting in unfeasible simulations. Thus, in order to be practically solvable the equations are manipulated introducing coefficients, closures, sub-models and parameters to be practically solvable. Experimental data are needed to validate to approximated model and to calibrate the model. This requires to set up an experimental validation, so all problems related to experimental testing would arise again.

The discussion of the pros and the cons of the investigation approaches confirmed that, despite its challenges, the numerical simulation is the most appropriate for the engineering handling of hydro-abrasive wear of Pelton turbines. Thus, it is necessary to analyse it carefully to make it an effective engineering tool, reaching the best compromise between accuracy and feasibility, and develop criteria and best practices to identify the most appropriate modelling choices. As it will be further clarified in the next section, this is the long-term objective of the research project of which this thesis is a first step.

1.4. Aims and structure of the thesis

So the engineering need that the research project to which this thesis belong to aims to address is to produce an effective tool for the handling of hydro-abrasive wear of Pelton turbines at the design and management stages. The discussion presented in the previous section yield to the decision of adopting the computer simulation as the investigation approach. Due to the multi-physical nature of the problem, in order to better investigate the phenomenon under analysis, it would be necessary to further analyse the problem from both a computational fluid dynamics and solid mechanics perspective. In the following discussion, the focus is on computational fluid dynamics related to the phenomenon of erosion. Thus, the goal of this thesis is to identify the most critical aspects of CFD (Computational Fluid Dynamics) applied to turbine erosion to better understand how to address these issues and study their relevance in an application-oriented context. As already mention, the main problem with CFD models is that, in order to be practically applicable, they are approximate in nature, for which several modelling choices have to be made and several parameters decided by the end-user. In addition, strict validation cannot be carried out because, given the size of the turbine, setting up an experimental validation in the laboratory would be too expensive. However, it is possible to perform a qualitative validation either by comparing the results obtained with those of a laboratory experiment with a reduced-scale model or by comparing them with blades ruined in real cases. At the same time, it is possible to validate a CFD model in a reduced-scale model and then use the results obtained to carry out simulations in a full-scale case. In conclusion, there are several methods to validate the model that do not require to setup an experimental validation through a full scale prototype, however, these methods imply a loss in accuracy. This makes achieving reliable simulation results very challenging. Some preliminary steps towards the development of an engineering-effective predictive tool have been undertaken in this thesis through an increasing complexity approach. The procedure considers different test cases starting from a fixed blade modeled as 2D in single-phase (water-only) condition up to a fixed blade modeled in 3D in multi-phase (water-

air-particle) condition. In this way, all features of the modelling framework are assessed individually, limiting their mutual interaction. By verifying the physical consistency of the obtained solution and providing a validation as allowed by the available information, the modelling tool could be constructed step-by-step.

The thesis consists of five chapters in addition to the present introductory one.

The second chapter analyses all the aspects that make the modelling of hydro-turbine wear particularly complex (e.g. its multi-physics nature, its multi-scale nature, the existence of fluid-structure iteration processes, the multi-phase flow). All modelling choices that must be main for building a predictive model are also listed and discussed.

In the third chapter, the main models used throughout the thesis are presented, in particular the models for simulating the single-phase water flow, the two-phase air-water flow, the tracking of the trajectories of the sediments, and the erosion model for predicting the loss of material produced by the impacts of the sediments against the turbine components.

The fourth chapter presents the first test case, a fixed blade modeled as 2D. This chapter will then be divided into sub-chapters according to the fluid dynamic characteristics, namely, a submerged water jet, the free water jet in air and the free water jet in air with particles.

The fifth chapter presents the case of a three-dimensional fixed blade. This chapter will then be divided into sub-chapters analysing the case of free water jet in air with and without particles. Then the erosion is computed.

Finally, the sixth chapter sets out conclusions and possible future developments.

2 | Challenges in the numerical simulation of turbine erosion

The goal of the present chapter is to identify the most critical aspects of the numerical simulation of hydro-abrasive wear of turbines. In particular, the idea is to span over all the aspects that make the numerical predictions highly uncertain and complex. Due to the reasons explained in the introduction, the experimental characterization of turbine erosion is very hard if not impossible to achieve, so that the numerical simulation is the only viable approach to produce the engineering-effective tool required by designers. Therefore, it is necessary to understand all uncertainty factors of the simulation approach in order to find a way to manage them. These relate with the multi-physics and multi-scale nature of the problem, in addition to the multi-phase nature of the flow and the jet-blade interaction. Therefore, in the following sections, these elements will be analysed one after the other.

2.1. Multi-physics nature of hydro-abrasive wear

The erosion of hydro (Pelton) turbines involves different physical processes. In particular, the core problem consists of a sediment-laden free jet impinging on the blade and producing removal of material. It is emphasised that in this context, there is a free jet of water in the air, so the phases involved are both water and air. So, on one hand, there is a fluid dynamic side of the problem concerning the hitting of the sediment-laden jet on the blade and its subsequent lateral deflection. This process is described through complex fluid-dynamic models, solved numerically through CFD (Computational Fluid Dynamics) techniques. On the other hand, there is the material damage caused by the solid particles that collides with the walls of the blade. This is the solid mechanics side of the problem, which relates with the mechanical interaction between the particles and the wall. In order to handle this processes in the context of the computer simulation, the basic equations of damage and fracture mechanics should be solved numerically through CSM (Computational Solid Mechanics). The multi-physical nature of the problem is shown in

Figure 2.1. While a completely multi-physics approach to the erosion of Pelton turbine blades is desirable, it is not feasible due to the computational cost and complexity of such simulations. The multi-physics approach would require solving the fluid dynamics equations and the solid mechanics equations simultaneously, which is computationally expensive and requires significant computational resources. As a result, most studies focus on either the fluid dynamics aspects or the solid mechanics aspects of the problem, rather than both. Moreover, the physics involved in the erosion of Pelton turbine blades are highly nonlinear and can lead to a wide range of behaviors that are difficult to capture in a single model. This variability makes it challenging to develop a single multi-physics model that can accurately capture all the phenomena involved in the erosion process. Instead, researchers typically develop simplified models that focus on specific aspects of the problem. In conclusion, the erosion of Pelton turbine blades is a complex and challenging problem due to its multi-physics nature. CFD and CSM are powerful tools for understanding the fluid dynamics and solid mechanics.

Figure 2.1: Shown on the right is the microscopic scale of the problem of particle impact causing surface erosion, which is solved with a solid mechanics model. On the left, the mascroscopic scale is shown where the flow of water with particles inside is represented, which is solved with a fluid-dynamic model.

2.2. Multi-scale nature of hydro-abrasive wear

Another element of complexity is given by the the fact that multiple scales are involved in the problem of hydro-abrasive wear of turbines. These span from the macroscopic scale of the turbine blade to the microscopic scale of the particles that collides against the surface of blade. All scales are relevant to the process in analysis. In particular, the micro-scale problem cannot be neglected, as the small pits caused by the continuous collision of particles against the surface of the blade cause the visible structural damage.

Indeed there is a huge difference in size between particle that have a mean diameter d_{50} of the order of μm and turbine that has width and depth of the order of m. In Figure 2.2 is possible to see the dimension of the sediment that collides against the surface. However, the multi-scale nature of turbine wear does not limit to the space scales, but it also extends to the time ones. In fact, the failure of a machine in a sediment-laden environment might happen after approximately 3 years [7], whereas the individual particle-wall collisions are very quick and might take only milliseconds to occur as shown in Figure 2.2; thus, the process involves very different timescales.

The many space and time scales which play a role on the wear process have an impact on the requirements of a simulation model. Indeed, to capture all spatial scales and all temporal scales, the mesh should be extremely fine and the time step extremely small. In particular, to capture all scales of the turbulent problem, the cell size and time step should be smaller than the lifetime and size of the smallest turbulent eddies. However, accounting for all those scale would produce excessive computational cost. The modelling assumptions and approximations made to overcome this problem might result in numerical errors, so that an acceptable compromise must be searched between accuracy and computational feasibility.

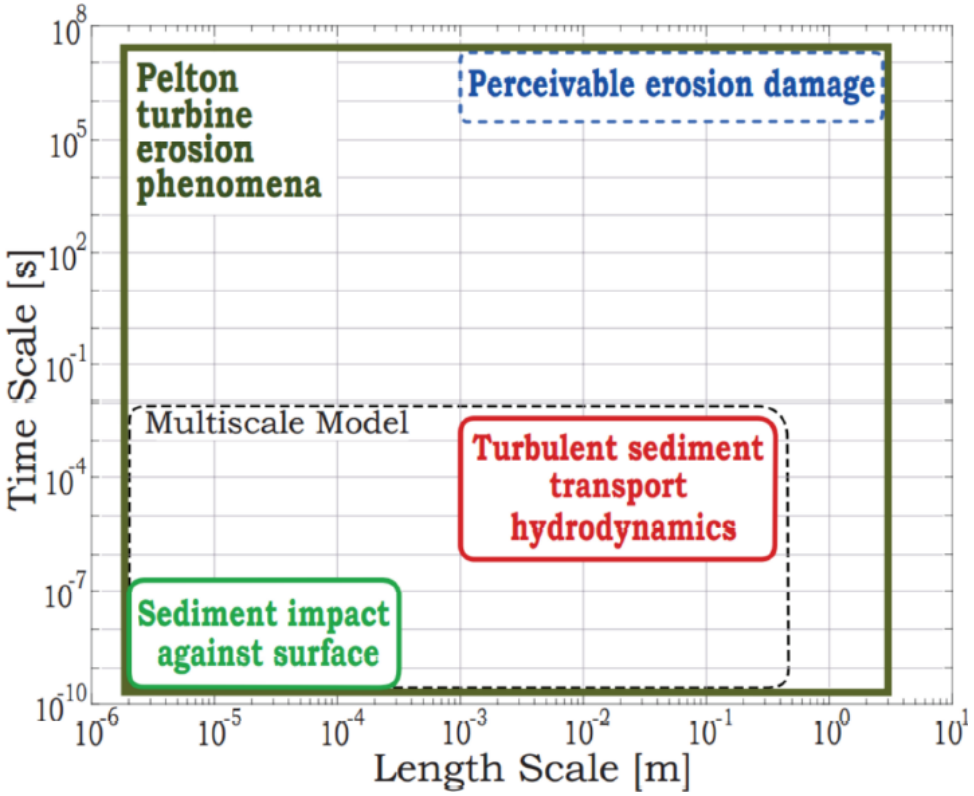

Figure 2.2: Multi-scale nature of the hydro-abrasive wear of a Pelton turbine (picture from Leguizamon [7]).

2.3. Challenges in the fluid dynamic modelling

Specific challenges are found regarding the modelling of the fluid dynamic processes governing hydro-abrasive wear of turbines. These are primarily due to the fact that the flow is turbulent and multi-phase. In fact, the operation of the turbine consists of a sediment-laden water jet released in an air environment and hitting the turbine blades. Hence, the flow is a turbulent three-phase one, consisting of water, air, and sediment. Modelling such a type of flow is extremely difficult, and demands for the most appropriate method within the multi-phase Computational Fluid Dynamics framework. In the following sections, the basic available approaches to handle all these complexity are analyzed.

Figure 2.3: Sediment-laden-river (picture from hydrosustainability.org).

2.3.1. Modelling of the turbulent flow

The flow in Pelton turbines is turbulent. Turbulent flows are very complex and chaotic in nature, which makes it is difficult to simulate them. Reproducing all the space and time scales of a turbulent flow is substantially unfeasible because of the excessive computational burden. Consequently, in some cases only the larger scales are resolved and the other

are modelled (LES), in others only the mean flow (RANS). These are the only feasible engineering approaches as a direct numerical simulation (DNS) would be computationally too expensive. In some contexts, even LES would be computationally too expensive, which is why a RANS model was used in this thesis to simulate the fluid problem. There are different RANS-based turbulence models available, each of which is best suited to certain conditions. Given the fact that all these models are, in the end, (semi)-empirical in nature, without an experimental validation it is difficult to say which is the most suitable to simulate the flow inside a specific Pelton turbine. Another critical aspect of the RANS framework is the modelling of the near-wall turbulence. Different approaches (wall function vs low-Re) are available, as well as different option within each approach. Once again, depending on the specific test case and on the information to be obtained, some options work better than others, but only experiment data allow establishing the most appropriate one. In the lack of experimental data, a practical approach is to compare different turbulence modelling options through a sensitivity analysis. Even if this does not allow determining the best option in a strict sense, at least, it gives some idea of the impact of this feature of the CFD framework, as it is carried out in section 4.1.4.

2.3.2. Modelling of the water jet in air

Another challenging step is the simulation of the water jet in the air environment, which requires a two-phase fluid dynamic model. There are two main methods to simulate processes like the one under consideration, namely, the homogeneous models and the inhomogeneous models according to the *Ansys* documentation [8]. The former are based on the assumption of immiscible fluids and a single set of momentum equations is shared by the fluids. Conversely, inhomogeneous models solve a set of n momentum and continuity equations for each phase. Coupling is achieved through the pressure and interphase exchange coefficients. This method leads to an increase in the number of uncertain coefficients and parameters compared to homogeneous methods, thus making the solution more uncontrollable, whereas homogeneous methods, although less accurate, are more robust. Moreover, the occurrence of air entertainment phenomena is generally rare in the water jets of Pelton turbines. Thus, a homogeneous model is chosen in this thesis, in particular the Volume of Fluid (VOF) on the grounds of a literature review [3, 4, 6, 9, 12, 15, 17, 18, 20, 21]. Indeed, the following articles have shown that the most commonly used model in the literature is the VOF for the study of Pelton turbines.

2.3.3. Modeling of the sediment-laden water jet

The hydro-abrasive wear of the turbine blades occurs due to the presence of sediments in the water jets, which makes the flow a three-phase water-air-solid one. A method must therefore be chosen to calculate the motion of the sediments dragged by the fluid and, in this thesis, a Lagrangian modelling approach was used.

In Lagrangian-based models, the particle equation of motion are solved for a certain number of computational particles. An example of particles trajectories is shown in Figure 2.4.

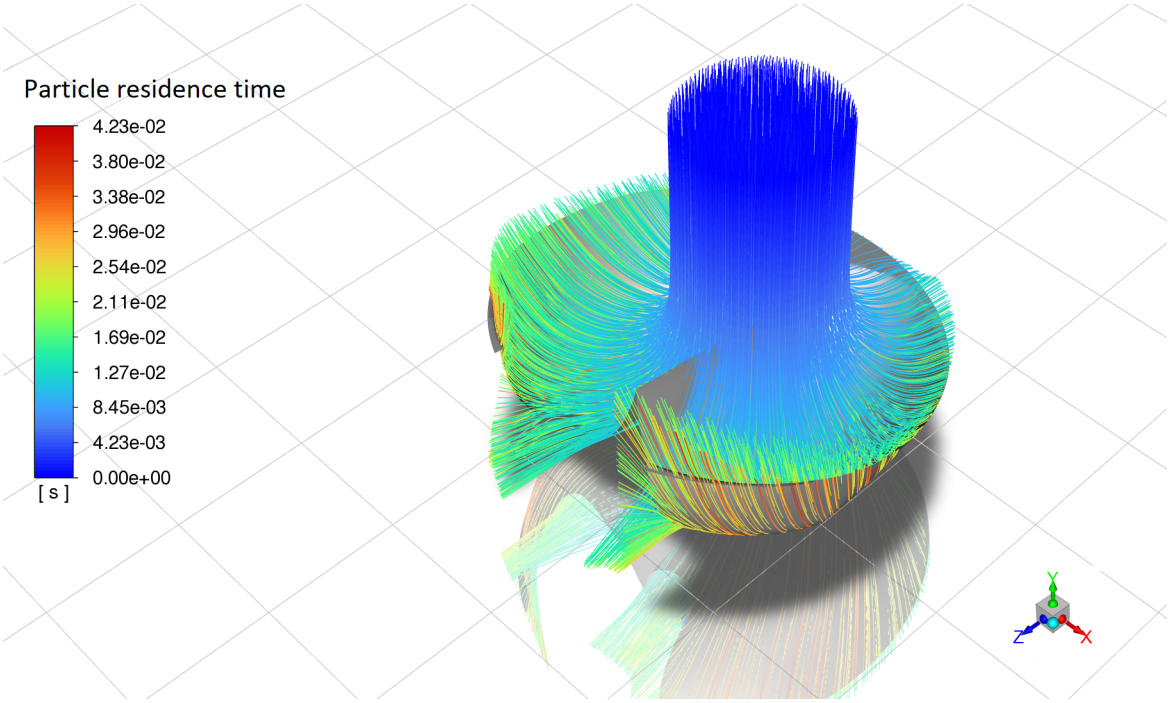

Figure 2.4: Trajectories of sediments. In this Figure the variable under analysis is the particle residence time.

In this thesis, a volumetric concentration of 0.1% was used as a reference value, referring to the thesis of Leguizamon [7] from which the parameters for the test case chapters were taken. This models are useful to simulate phenomena wich occurs at the scale of the individual particles, as it is the case of wear processes.

The great advantage of this method is that the tracking is done a posteriori, that is, after the flow field has been calculated. This greatly reduces the computational burden. Otherwise, every time different particle configurations are to be tracked, the flow field would have to be recalculated.

2.4. Modeling of the jet-blade interaction

Another element of complexity is given by the modeling of the jet blade interaction. Specifically, the blade moves as a consequence of the impact of the jet on it; thus, the speed at which the blade rotates is not defined a priori, but it is a consequence of this interaction. Accounting for the full fluid-structure interaction is potentially feasible but in practice there are no available studies where is simulated the water-jet that sets in motion the blade. So, alternative approaches are made when dealing with the simulation of hydro-abrasive wear of Pelton turbine blades. In the former, the blade is modeled as fixed, namely, the fluid-structure interaction is completely removed. For example, in Leguizamon's thesis, a test case with a fixed blade was considered [7]. This is the approach used in this thesis, mainly due to the preliminary nature of the work and to the need of keeping the computational cost within acceptable limits. As a more accurate (yet computationally more expensive) alternative, it is possible to impose a fixed rotation. Even in this case, however, it would be necessary to introduce moving mesh techniques that would increase the computational cost. Clearly, this is an approximation because, in reality, the rotation is not imposed a priori but a consequence of the interaction with the jet. Summing up, in this thesis has been considered a fixed blade. However, considering a fixed blade implies changes to the characterisation of erosion. It is therefore important to understand how relevant these changes are, so as to know whether reducing the computation cost still leads to an accurate prediction of erosion on the blade. At the same time, making these approximations runs the risk of losing the engineering sense of the problem, in fact you risk straying too far from the real case. The only way to analyse this problem in detail is to compare the results obtained in the fixed and stationary rotation cases with the real results, to see if the prediction is more or less accurate.

2.5. Challenges in the solid mechanics modelling

Solid particle erosion is the removal of material arising from its interaction with solid particles transported by a carrier fluid. There are two types of erosion : *impact erosion* and *abrasion erosion*. In the case of Pelton turbines there is the *impact erosion*, that consist in individual particles that collides against the blade, causing removal of material.

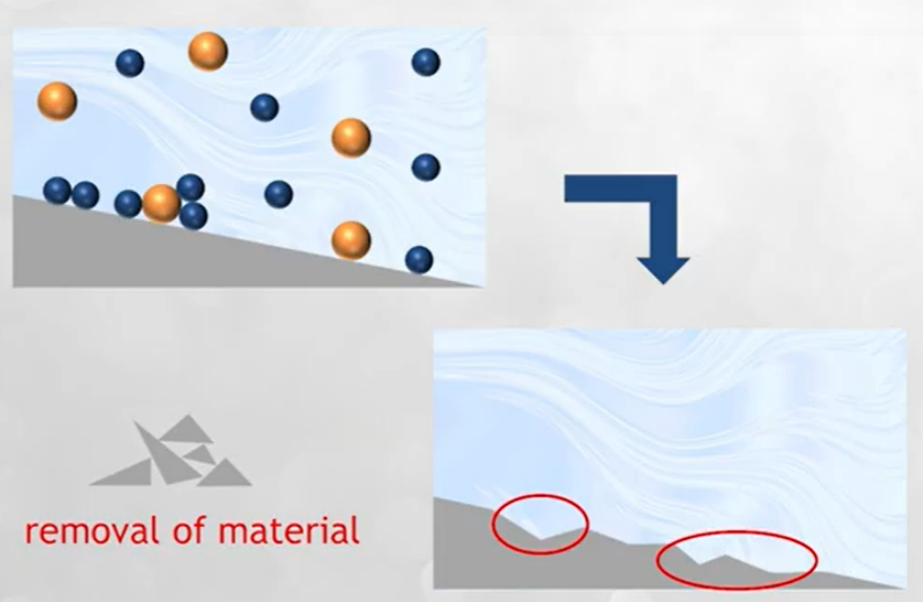

Figure 2.5: Micro-scale process of erosion.

Since a fully multi-physical, multi-scale modelling is not feasible as explained in the sections, at this point the mechanics of solids is replaced with an empirical erosion model. There are several correlative equations that relate impact parameters to the relative damage caused. This is affected by many parameters that are the impingement velocity, the angle of impingement, the particle size, the particle shape, the material properties. All these features with both a direct or indirect effect affects the erosion process.

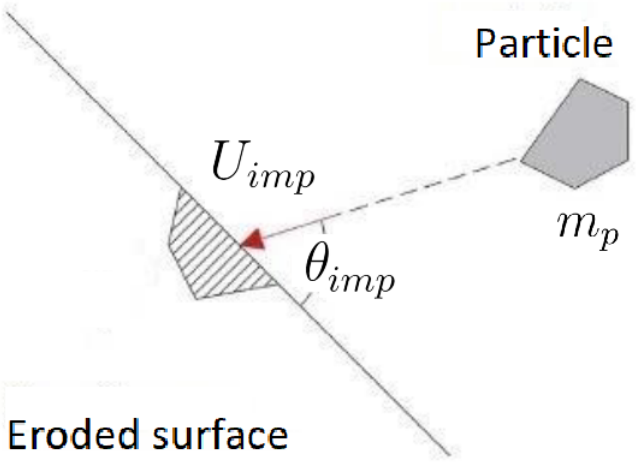

Figure 2.6: Velocity and impact angle (adapted from Panico [16]).

where, U_{imp} is the impact velocity and θ_{imp} is the impact angle.

The assumption made in this context is that of steady-state erosion, i.e. that the mass of material removed is linear with respect to time. This approximation is only acceptable within a certain time interval. In fact, for both low and high times a departure from the steady state condition occurs. In the first case this is due to the change in the mechanical condition of the material after the first impact, in the second case because a large part of the surface has been eroded.

The most common erosion models, that are empirically obtained by fitting the experimental result of dry direct impact test, assume steady state erosion and neglect particle interaction.

One way to predict erosion is to consider these following parameters. At each time position and parcel velocity are store, so that the erosion models turns these quantities into these new quantities:

1. $\dot{E}_{imp}$ that is the mass flow rate of removed material
2. $\dot{E}_{cell} = \sum_{imp \in cell} \dot{E}_{imp}$ that is the mass flow rate of removed material from a cell

In this way it is possible to compute the integral erosion ratio that is:

$$IER = \frac{\sum_{imp \in cell} \dot{E}_{imp}}{\dot{M}_p} \tag{2.1}$$

where $\dot{M}_p$ is the total solid mass flow rate.

2.6. Characterization of the sediments

A final particularly critical issue relates with the characterization of the sediments that are dragged by the water jet and hit the blade causing its erosion. Providing a characterization of sediment-related quantities like the concentration, the shape, the size, and material properties is very difficult for real cases involving natural solids. At the same time, the sediment properties significantly affect the erosion process in several ways. The *shape* off the sediments affects the erosion process because angular particles cause more damage than rounded ones. Moreover, nearly spherical particles are less affected by the drag compared to highly angular ones, and this has an effect on the location, the velocity, and the angle of the impacts. The *size* determines the energetic content of the impact, so that, for the same impact velocity and angle, a bigger particle cause more damage than a smaller particle. However, the size of the particles affects their trajectories, because finer

particles follow the fluid streamlines more closely, whereas bigger particles tends to move more freely. This affects the way in which the particles hit the blade, namely, the location of the impacts, the impact velocities, and the impact angles. Also the *concentration* of the sediments in the jet affects the severity of erosion. Indeed, the higher the number of particles the higher the erosion. However, above a certain threshold, the particles might collide with each other in the near wall region, reducing the number of impacts on the blade and the impact velocities. Finally, the *material properties* such as the particle density affects the wear process through modifying the interaction of the particle and the flow field and energetic content of the impact. All these features are shown in the Figure 2.7.

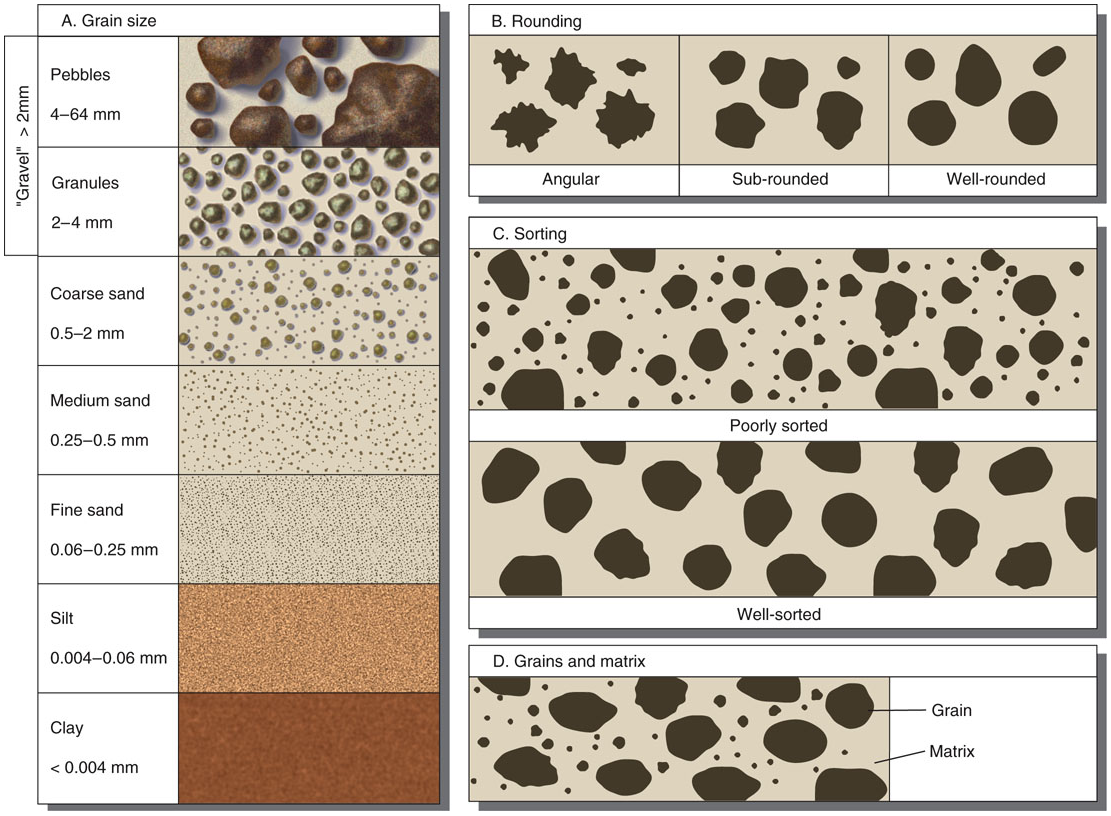

Figure 2.7: Example of sediments with different size and shape (picture from nps.gov).

However, in the following thesis, a one-way coupling regime has been considered, due to the low concentration of sediments, so that these information are not captured. Finally, in this thesis, the values of these parameters, like sediment diameter, sediment concentration, were taken from the relevant literature and that, in any case, through CFD the impact of each of them can be explored by means of appropriate sensitivity analyses. In fact, if a sensitivity analysis shows the results to be independent of a particular parameter, there is no need to investigate its true value further.

3 | Description of the mathematical models

The modelling approaches for the CFD simulation of Pelton turbines will be now discussed. To avoid discussions that would go beyond the scope of this dissertation, only the main models used will be presented in detail. For the others, the reader is referred to the Fluent Guide [8].

3.1. Modelling of the turbulent, single-phase flow

A complex aspect of CFD is the modeling turbulent flows. This flow is characterized by a strong mixing of particles so that it is inherently unsteady and 3D. A turbulent flow is defined as the superposition of turbulent eddies (coherent rotational patterns), that have a characteristic size, velocity and lifetime. Particularly relevant in this case are the biggest turbulent structures and the smallest turbulent structures. This is because the time step and mesh size must be on the order of magnitude of the smaller turbulence structures, while the system has a size on the order of the larger turbulence structures.

There are different methods available to model turbulent flows. The first one is the DNS method (direct numerical simulation) where all the scales of turbulence are resolved. However this would require very small time steps and cells sizes, namely smaller than the lifetime and size of the smallest eddies, respectively. In most of the practical applications, this approach is unfeasible due to the excessive computational cost.

The second approach is the LES (large eddy simulation) where only the turbulence scales up to a certain threshold are resolved, and all the others are modeled. However, due to the size of the system, most of the times also this method would be unfeasible in many applications computationally too expensive.

Finally, the RANS (Reynolds Averaged Navier Stokes Equations) method solves only for the average flow field, so that the computational cost is significantly reduced.

Accordingly, the steady RANS method was used in this thesis to solve the fluid problem in order to keep the computational cost under control.

3.1.1. The RANS equations

RANS models are steady-state in nature, and they can be 1D, 2D, and 3D. They rely on the Reynolds decomposition that is:

$$\phi(\vec{r},t) = \langle\phi\rangle(\vec{r}) + \phi'(\vec{r},t) \tag{3.1}$$

where $\vec{r}$ is the position vector, t is the time, ϕ is the generic fluid-dynamic variable, $\langle\phi\rangle$ is the Reynolds average of ϕ, ϕ' is the fluctuating component of ϕ and

$$\langle\phi\rangle(\vec{r}) = \lim_{x\to+\infty}\frac{1}{T}\int_0^T \phi(\vec{r},t)\mathrm{d}t \tag{3.2}$$

is the Reynolds averaging operator. In particular T have to be greater than the time scales of fluctuations because they must be removed. This average operator is applied to the instantaneous Navier-Stokes equations obtaining the Reynolds Averaged Navier-Stokes Equations that, for incompressible flow, have the following form:

$$\begin{cases} \nabla\cdot\vec{V} = 0 \\ \dfrac{\partial\rho U\vec{V}}{\partial x} + \dfrac{\partial\rho V\vec{V}}{\partial y} + \dfrac{\partial\rho W\vec{V}}{\partial z} = -\nabla P + \Delta\vec{V} + \nabla\cdot\bar{\bar{\phi}}^{Re} \end{cases} \tag{3.3}$$

where, $P = \langle p\rangle$, $\vec{V} = \langle\vec{v}\rangle$ and the Reynolds stresses tensor:

$$\bar{\bar{\phi}}^{Re} = \begin{bmatrix} -\rho\langle u'u'\rangle & -\rho\langle v'u'\rangle & -\rho\langle w'u'\rangle \\ -\rho\langle u'v'\rangle & -\rho\langle v'v'\rangle & -\rho\langle w'v'\rangle \\ -\rho\langle u'w'\rangle & -\rho\langle v'w'\rangle & -\rho\langle w'w'\rangle \end{bmatrix} \tag{3.4}$$

This one is the formulation effectively used in this thesis. However, the total number of scalar equations is equal to 4 while the number of unknowns is equal to 10, namely, U, V, W, P and all the independent components of $\bar{\bar{\phi}}^{Re}$. So this is not a closed system of equations. In order to close the system, the RANS must be coupled with some turbulence model. There are several models of turbulence, each of which has a strong empirical component. Each of these therefore has its validity under certain conditions, but these conditions are not always clearly and are unambiguously defined.

3.1.2. The standard $k-\varepsilon$ turbulence model

One of the most widely used turbulence models in engineering CFD calculations is the standard $k-\varepsilon$ of Launder and Spalding [8]. This model relies on the eddy viscosity assumption of Boussinesq, which states that the Reynolds stresses tensor can be expressed as

$$\bar{\bar{\phi}}^{Re} = \frac{1}{3} tr(\bar{\bar{\phi}}^{Re}) + 2\mu_{\text{turb}} \langle \bar{\bar{D}} \rangle \tag{3.5}$$

where

$$\langle \bar{\bar{D}} \rangle = \frac{\nabla \vec{V} + \nabla \vec{V}^T}{2} \tag{3.6}$$

is the Reynolds-averaged strain rate tensor and μ_{turb} is the eddy viscosity, which is not a physical property of the fluid (like μ), but a property of the flow.

Substituting 3.5 into the system of equations 3.4, one obtains:

$$\begin{cases} \nabla \cdot \vec{V} = 0 \\ \dfrac{\partial \rho U \vec{V}}{\partial x} + \dfrac{\partial \rho V \vec{V}}{\partial y} + \dfrac{\partial \rho W \vec{V}}{\partial z} = \rho \bar{f} - \nabla P^* + \nabla \cdot [\mu_{\text{turb}} \nabla \vec{V}] + \nabla \cdot [\mu_{\text{turb}} \nabla \vec{V}^T] \end{cases} \tag{3.7}$$

where $P^* = P + \dfrac{2}{2}\rho k$ and k the turbulent kinetic energy per unit mass, $k = \dfrac{1}{2}(\langle u'u' \rangle + \langle v'v' \rangle + \langle w'w' \rangle)$.

A turbulence model is then required to evaluate μ_{turb}. The standard $k-\varepsilon$ expresses μ_{turb} as a function of two variables, namely, the already mentioned turbulent kinetic energy per unit mass k and the rate of dissipation of k per unit mass, called ε as shown in equation 3.8.

$$\mu_{\text{turb}} = \rho C_\mu C_{\text{d}} \frac{k^2}{\varepsilon} \tag{3.8}$$

Two A-D-R equations are then solved for k and ε, as follows,

$$\begin{cases} \nabla \cdot (\rho \vec{V} k) = \nabla \cdot [(\mu + \dfrac{\mu_{\text{turb}}}{\sigma_k}) \nabla k] + 2\mu_{\text{turb}} \langle \bar{\bar{D}} \rangle : \langle \bar{\bar{D}} \rangle - 2\rho\varepsilon \\ \nabla \cdot (\rho \vec{V} \varepsilon) = \nabla \cdot [(\mu + \dfrac{\mu_{\text{turb}}}{\sigma_\varepsilon}) \nabla \varepsilon] + 2\dfrac{\varepsilon}{k} C_{1\varepsilon} \mu_{\text{turb}} \langle \bar{\bar{D}} \rangle : \langle \bar{\bar{D}} \rangle - C_{2\varepsilon} \rho \dfrac{\varepsilon^2}{k} \end{cases} \tag{3.9}$$

The values of the numerical coefficients have been set as recommended in [7], namely, $C_\mu = 0.09$, $\sigma_k = 1.0$, $\sigma_\varepsilon = 1.3$, $C_{1\varepsilon} = 1.44$, $C_{2\varepsilon} = 1.92$.

Then since it will be considered in the test cases it is necessary to define the turbulence

intensity as:

$$TI = \frac{\sqrt{\frac{2}{3}k}}{v} \tag{3.10}$$

where v is the velocity magnitude.

3.1.3. Notes on the other turbulence models employed

The other model considered are the $k-\varepsilon$ relizable, $k-\varepsilon$ RNG, $k-\omega$ SST. All these models are based on the Boussinesq assumption, and also in this case with transport equations for k and ε. The main difference of these methods are related to the method of calculating the turbulent viscosity, the generation and the destruction term. However, these models are well-known and commonly used in the CFD practice. As a consequence, the following will not be presented. All the explanation can be found in [8].

3.2. Modelling of the turbulent, air-water flow

The Volume of Fluid (VOF) model was employed for the simulation of the water jet in air. Although in the used code a multi-phase formulation of the VOF is available [8], for the purpose of this dissertation only the two-fluid formulation was employed and thus presented. The information reported here below was obtained from [1, 8].

The VOF relies on the assumption that the fluids involved are immiscible, so that they are rigidly separated by an interface without a region where the two fluids are mixed. With respect to the RANS equations, another variable is added into the system: the volume fraction of each fluid in every computational cell. The volume fraction of phase q=w,a (where w is water and a is air) is defined as:

$$\alpha_q = \frac{\text{volume of phase q in one element}}{\text{whole volume of the element}} \tag{3.11}$$

Clearly, the sum of the volume fractions of the two phases in each computational cell is equal to 1. Namely, if we consider the phase q, the volume fraction α_q can be:

1. $\alpha_q = 1$, when the cell is entirely occupied by phase q
2. $\alpha_q = 0$, when the cell is empty of phase q
3. $0 < \alpha_q < 1$ when in the cell there is the interface between the two phases.

Then to track the interface the continuity equation is solved: In this case we are consid-

ering the RANS formulation of the VOF because the test case considered are steady:

$$\nabla \cdot (\alpha_w \rho \vec{V}) = 0 \tag{3.12}$$

The volume fraction will not be solved for both phases. The other one is computed through the following constraint:

$$\alpha_a = 1 - \alpha_w \tag{3.13}$$

The material properties in each cell will be a weighted average of the properties of the two fluids. So the density and dynamic viscosity in each computational cell will be:

$$\rho = \rho_a \alpha_a + (1 - \alpha_a)\rho_w \tag{3.14}$$

$$\mu = \mu_a \alpha_a + (1 - \alpha_a)\mu_w \tag{3.15}$$

A single momentum equation is solved. Just one velocity field is determined, and the volume fraction appears in the equations described above through μ and ρ:

$$\nabla \cdot (\rho \vec{V} \vec{V}) = -\nabla P + \nabla \cdot \bar{\bar{\phi}}^{Re} + \nabla \cdot [\mu(\nabla \vec{V} + \nabla \vec{V}^T)] + \vec{F} \tag{3.16}$$

where $\vec{F}$ is the surface tension force. $\vec{F}$ represents the interfacial surface tension, modeled as a function of the surface tension coefficient as explained in [1, 8]. Then also this model must be coupled with a turbulence models which provides a closure to the Reynolds stresses tensor. A VOF-variant of the models presented in sections 3.1.2 was employed, which uses the space-variable density and viscosity calculated as in equations 3.14, 3.15 .

3.3. Tracking of the trajectories of the sediments

The best way to determine the flow field of particles in this context is that of considering an Eulerian-Lagrangian approach, in which the fluid field is solved via an Eulerian model and the particle field via a Lagrangian model. In this case the particles equation of motion are solved for each "parcel" individually. Often, in DPM calculations each trajectory is not associated to a single particle but to a group of particles called "parcel". This because particles that are injected more or less in the same position will have the same trajectory. In this way the computational burden is reduced. In the context of Pelton turbines, DPM particle tracking was the best choice for determining the particle flow field,

as information is provided that could not be obtained otherwise, such as velocity and impact locations.In addition, "one-way-coupling" regime coupling was chosen because the sediment C concentration is well below the threshold value of 1%. In the DPM approach with "one-way-coupling" regime, the effect of sediment on fluid and sediment interactions are neglected.

So, firstly, the water jet in air is simulated without the sediment using the VOF. Then, the sediments' are injected into the domain one after the other and the Lagrangian equations of motion are integrated to determine their trajectories in the VOF flow field.

The equations solved for each computational particle are:

$$\frac{\partial \vec{r}_p}{\partial t} = \vec{v}_p \tag{3.17}$$

$$m_p \frac{\partial \vec{v}_p}{\partial t} = \sum \vec{F} \tag{3.18}$$

where $\vec{v}_p$ is the particle velocity, $\vec{r}_p$ is the position vector of the particle, and $\sum \vec{F}$ is the sum of all the forces exerted by the air-water system on the particles.

In this context the point-particle approximation was made, namely particles are much smaller than the integral scale of turbulence. The RANS-based formulation of the VOF presented in section 3.2 provides the Reynolds averaged fluid parameters of the air-water system in the center of the computational cells (bigger than the size of the particles). Therefore, these models cannot provide the pressure and shear stress distributions over the particle surface, which, once integrated, determine the particle motion. As a consequence of the above, the particle equation of motion must be coupled with force models, that estimate the forces exerted by the fluids to the particle starting from the VOF solution. These force models include the drag force $\vec{F}_d$, the pressure gradient force $\vec{F}_{pr}$, the buoyancy force $\vec{F}_b$, and so on. For sediment-laden water jets, the drag force is the dominant one and this is given by:

$$\vec{F}_d = \frac{1}{2}\rho C_d \left(\pi \frac{d^2}{4}\right) |\vec{u}_{@p} - \vec{v}|(\vec{u}_{@p} - \vec{v}) \tag{3.19}$$

where, ρ is the fluid density, C_d is the drag coefficient, d is the particle size, $\vec{u}_{@p}$ is the *unhindered fluid velocity*, namely the fluid velocity that can be hypothetically extrapolated to the particle centroid while ignoring disturbances caused by the particle itself and $\vec{v}$ is the fluid velocity. $(\vec{u}_{@p} - \vec{v})$ represent the relative velocity between the air-water system

and the solid particle. In this context, due to the non negligible effect, also the pressure gradient force has been considered. The force is given by:

$$\vec{F}_{pr} = -Wp\nabla p_{@p} \tag{3.20}$$

where W_p is the volume of the particle. The pressure gradient force quantifies the effect of a non-uniform pressure field in the absence of the particle itself. This force causes a body to tend to escape the pressure gradient, i.e. it tends to repel the particle by deflecting it laterally. This force goes from the region where the pressure is highest to the regions where it is lowest, in the absence of particles.

3.4. Erosion models

Single-particle erosion models are equations relating the material removal produced by a single particle-wall impact as a function of relevant parameter, such as the impact velocity, the impact angle. It is possible to see these features in Figure 2.6.

Many erosion models have been proposed in the literature. Most of them are empirical or semi-empirical algebraic formulas, which are obtained by fitting of experimental data. A widely used correlation was proposed by Det Norske Veritas (DNV). In practice the erosive wear is defined as material loss resulting from impact of solid particles on the material surface.

Then knowing the impact velocity and the impact angle the erosion rate is computes as:

$$e_r = \dot{M}_p K U_{imp}^n F(\theta) \tag{3.21}$$

where,

$$F(\theta) = \sum (-1)^{(i+1)} A_i \left(\frac{\theta\pi}{180}\right)^i \tag{3.22}$$

where, A_i, K are constants of the problem and can be found in **??** and U_{imp} is the impact velocity. Finally, emphasize that using one erosion model rather than another brings variations in the estimate of eroded material that are also significant [10].

However, the erosion pattern is less affected by the choice of erosion pattern [11].

4 | Case study 1: particle-laden flow in a 2D model of a fixed Pelton blade

In the first test case, only a transversal section of a Pelton blade was simulated as fixed in time through a steady-state, 2D model. Clearly, this setup is a simplification of the real case where the blade is three-dimensional and rotates.

Thus, the computational burden is reduced due to the very simple geometry, and the model is approximated because the blade-jet interaction is not considered. However, already in this case fundamental elements of the problem are considered such as the presence of the three-phase jet and the reproduction of the blade geometry in two dimensions. Therefore, this test case is crucial in the development of the model because it contains the essential elements, but at the same time allows the analysis to be carried out in controlled computation time.

Following the usual step-by-step approach, the elements of complexity of this preliminary 2D case were addressed one after the other. Compared to handling the complex problem at a glance, addressing one complex feature at a time allows a stronger assessment of the predictive capacity of the model. A number of analyses, such as the sensitivity to turbulence model analysis, will be carried out in the two-dimensional case and will be taken as a reference in the three-dimensional case.

Based on the above, the water jet was first simulated as submerged, so that a single-phase model could be used. Then, the air environment was introduced, switching to a two-phase (air-water) model. Finally, the trajectories of the sediments dragged by the water jet are calculated. The three configurations are described in Sections 4.1, 4.2, and 4.3, respectively.

4.1. Submerged water jet (single-phase flow)

Initially, the water jet was modeled as fully submerged in water, so that single-phase simulations were performed.

A sketch of the case study is presented in Figure 4.1 and has been reproduced from Figure 4.8.

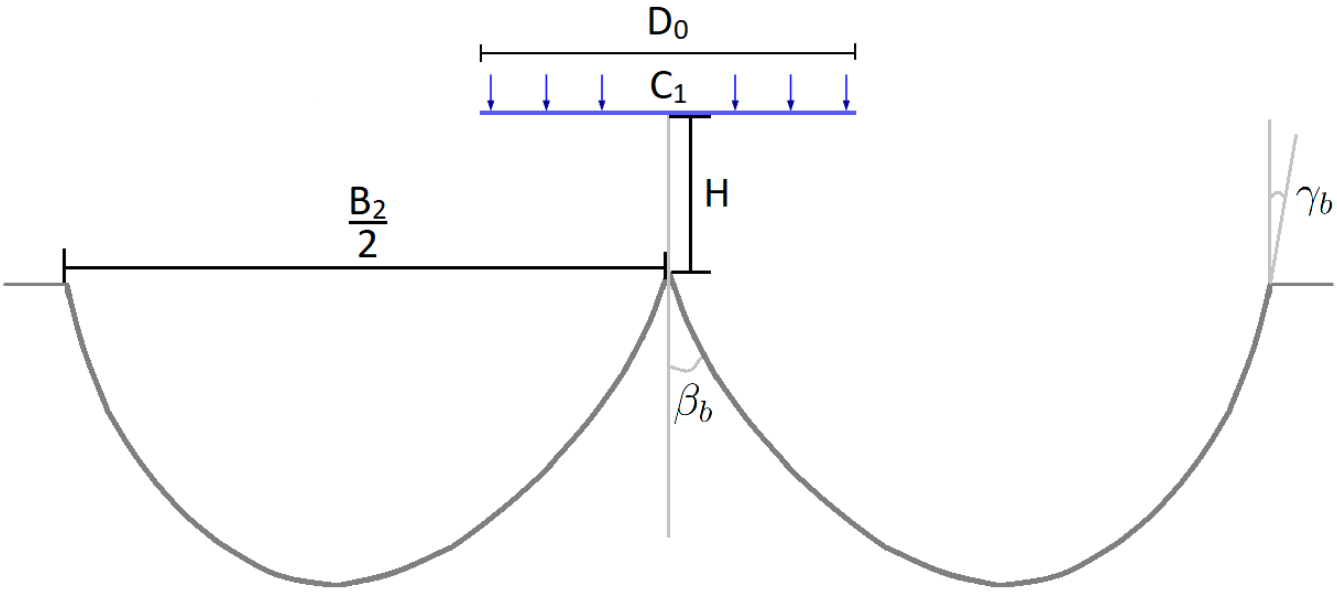

Figure 4.1: Sketch of the case study and relevant parameters.

All the parameters in Figure 4.1 are reported in Table 4.1.

Name	Parameter symbol	Value	Unit
Jet velocity	C_1	40.0	[m/s]
Jet Diameter	D_0	0.10	[m]
Bucket width	B_2	0.323	[m]
Bucket depth	B_3	0.008	[m]
Inlet distance	H	0.05	[m]
Bucket half-splitter angle	β_b	18.0	[°]
Bucket outlet angle	γ_b	12.0	[°]

Table 4.1: Geometric parameters case 1.

The objective of this case study is to obtain some results, such as those of the grid independence study, that can be exploited to reduce the burden of the following, more complex cases. For example, in the transition from single-phase to two-phase, the number of Grids was reduced from 7 to 4.

The analysis will be presented starting from the definition of the CFD setup (section 4.1.1), including the definition of the fluid dynamic model, the computational domain and the boundary conditions, and the other relevant numerical settings. Then, after verification of the physical consistency of the solution (section 4.1.2), the convergence study was carried out (section 4.1.3), followed by a sensitivity analysis upon the choice of the turbulence model (section 4.1.4). Finally, the test case will be validated (section 4.1.5) with respect to numerical results found in the literature.

4.1.1. CFD set up

The single-phase RANS equations, already presented in section 3.1.1 were solved coupled with an appropriate turbulence model. In particular, the standard $k-\varepsilon$ turbulence model (see section 3.1.2) with standard wall function was chosen since it is well suited for flows with high Reynolds number like the one under consideration, in addition to being one of the simplest and most widely used.

The computational domain of the 2D Pelton blade is then represented in Figure 4.2, together with the imposed boundary conditions. The symmetry of the geometry and of the mean flow has been exploited by considering only half of the nozzle-blade system, imposing a symmetry condition over the yellow boundary.

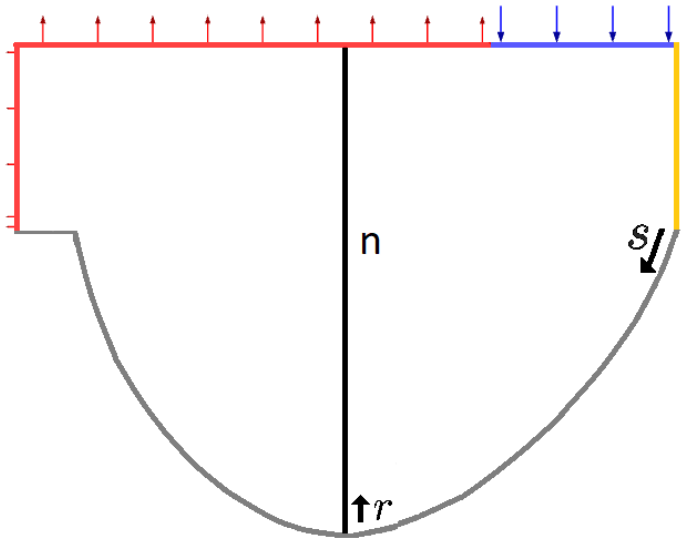

Figure 4.2: Computational domain and boundary conditions. The blue boundary corresponds to the inlet, the red one to the outlet, the grey one to the wall and the yellow one to the symmetry.

The case study parameters of this problem are specified in Table 4.1.

The geometry was created in Ansys Design Modeler starting from the geometric data reported in Table 4.1, namely, the bucket half-splitter angle, bucket outlet angle and the bucket depth ($0.025B_2$). The position of two additional points along the wall of the bucket was also determined from Figure 11.1 in the thesis of Leguizamon 4.8, and introduced into the sketch to better capture the profile of the blade.

In Figure 4.2, the blue boundary corresponds to the inlet, the red one to the outlet, the grey one to the wall and the yellow one to the symmetry. The inlet was placed adjacent to the outlet, after verifying that this choice did not produce any convergence issue. Since the distance between jet and blade is not known it was placed 5 cm from the blade taking the Figure 4.8 as reference for this distance. Specifically, an edge normal velocity of $C_1 =$ 40 m/s was imposed on the inlet, turbulent kinetic energy of 3.25 % and turbulent length scale of $0.03D_0$ taking as reference the values used in the thesis of Leguizamon [7]. At the output, however, a relative pressure of zero and a no-slip boundary condition for the wall were set.

Then to solve the problem the method used in this case was the SIMPLE with second order upwind for both turbulent kinetic energy and turbulent dissipation rate. The other options were the default fluent options.

4.1.2. Physical consistency of the CFD solution

As a necessary step to understand whether all the assumptions and approximations made to solve the problem are reasonable, it is necessary to analyze the simulation results qualitatively and interpret them in the light of the physical phenomena that govern this process. In this case, this is done by inspecting the velocity and turbulent kinetic energy fields.

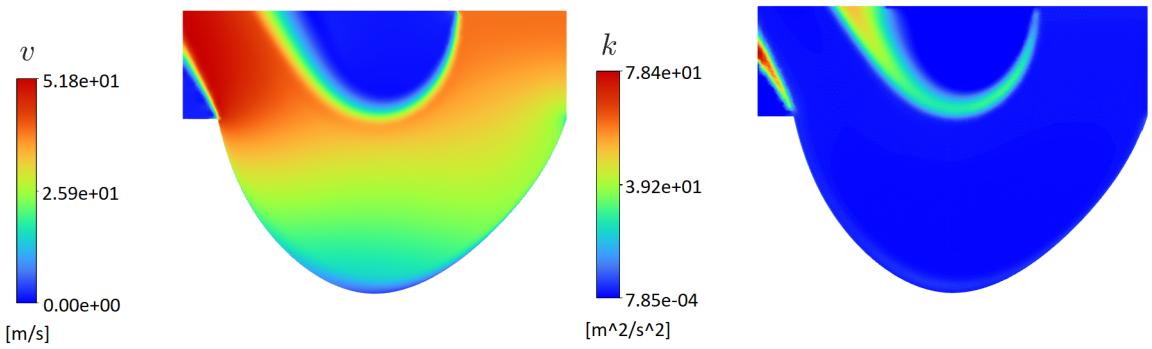

(a) Velocity magnitude (v). (b) Turbulent kinetic energy (k).

Figure 4.3: Some simulation results obtained.

The pictures in Figure 4.3b are obtained using Grid 7 that is reported in Table 4.2.

Regarding the velocity, shown in Figure 4.3a, this turns out to be zero at the wall due to the no slip boundary condition, and increases rapidly moving away from it. Thus, a boundary layer is observed, as expected from fluid mechanics considerations. So the numerical results are consistent with the underlying physical phenomenon.

From picture 4.3b the kinetic energy turns out to be higher in regions where moving water is in contact with still water and close to the solid wall, but this is not clearly visible in the plot as the values are quite low. This can be interpreted as a consequence of the frictional stresses acting between the jet and the surrounding still water, and those exerted on the jet by the blade.

4.1.3. Convergence assessment study

Then, a study was carried out to assess the numerical convergence of the simulation results. This required focusing on both the convergence with respect to the iterative solution algorithm and the convergence with respect to the computational mesh. In relation with the first aspect the residuals are set to 10^{-5} and the maximum number

of iterations to 5000. The maximum number of iterations chosen is sufficient for the normalized residuals to fall below the chosen threshold for all meshes.

As far as the grid independence study is concerned, seven different tetrahedral meshes obtained by halving the area of each element starting from the coarsest to the finest were considered. All meshes have an inflation layer along the wall, which consists of a number of parallel layers of prismatic cells with increasing thickness. Notably, the inflation layer was defined for all the Grids and refined by increasing the mesh resolution. Adding an inflation layer is a common approach in CFD simulations, which allows capturing more accurately the high transversal velocity gradients occurring in the proximity of solid walls, avoiding unnecessary grid refinements in the bulk flow region. The number of elements of each computational grid are summarized in Table 4.2.

Mesh	**Number of Elements**
Grid 1	2381
Grid 2	5039
Grid 3	7619
Grid 4	10099
Grid 5	12565
Grid 6	15082
Grid 7	17586

Table 4.2: Characteristics of the meshes used in the grid independence study.

By way of example, Figure 4.4 shows three meshes , the coarsest (Grid 1), the finest (Grid 7) and an intermediate one (Grid 4). The other meshes considered are shown in Appendix A.

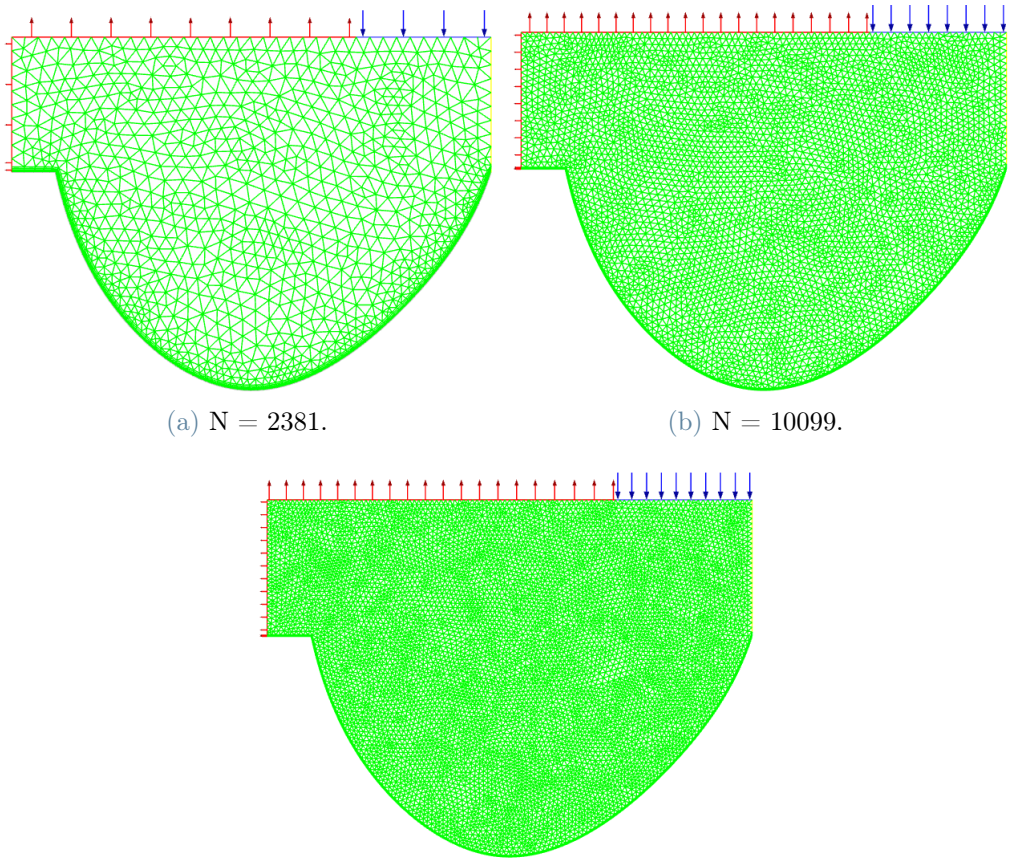

(a) N = 2381.

(b) N = 10099.

(c) N = 17586.

Figure 4.4: Exemplary meshes used in the convergence analysis.

The target parameters of the grid independence study were the mean and maximum value of k over the entire computational domain, and the profiles of velocity magnitude and k along the n-axis that is shown in Figure 4.2.

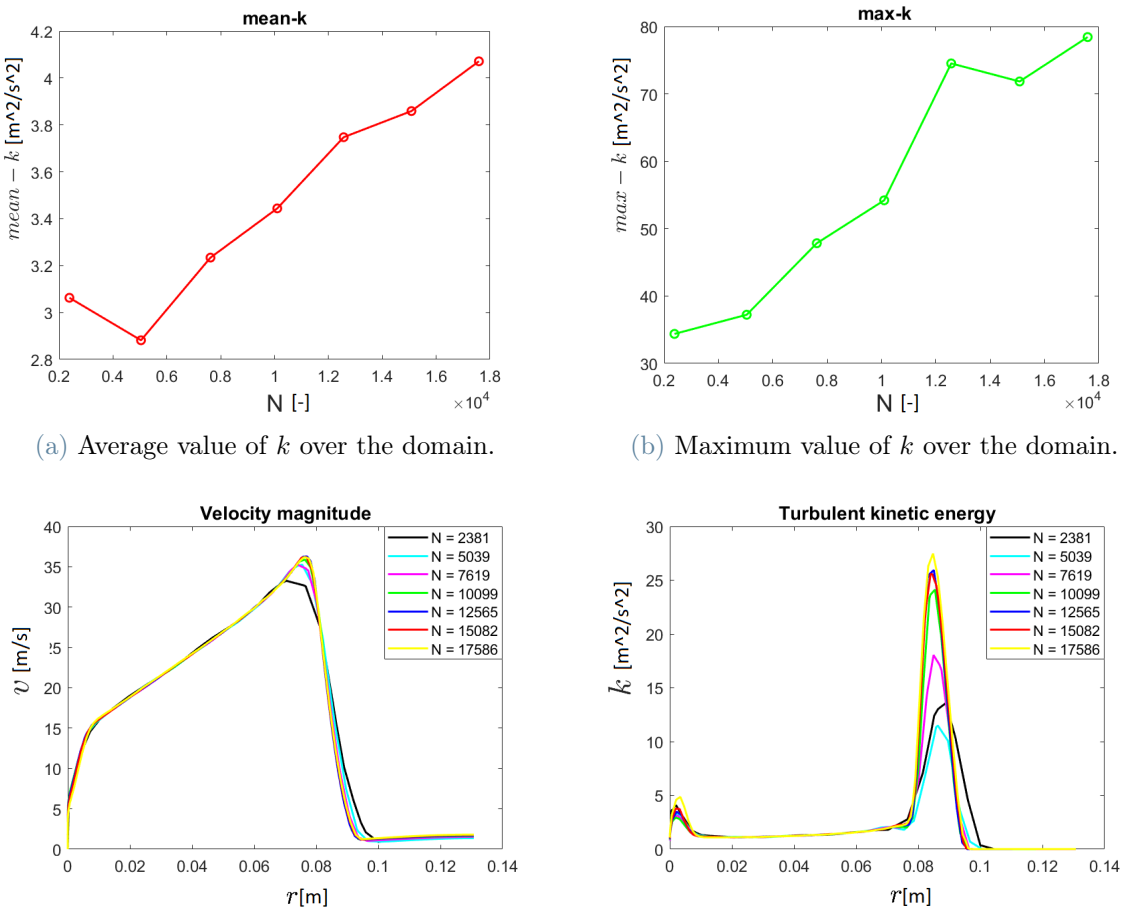

(a) Average value of k over the domain.

(b) Maximum value of k over the domain.

(c) Velocity magnitude over the n-axis.

(d) Turbulence intensity over the n-axis.

Figure 4.5: Some results of the grid independence study.

In Figure 4.5a it is possible to see that the mean value of k slightly increases with the mesh resolution. This could be due to the fact a finer grid allows more accurate estimation of k in the regions where this parameter is very high. And, indeed, Figure 4.5b clearly shows that the maximum value of k in the domain increases with the mesh resolution. Note that, in any case, the mean value of k ranges between about 3.8 to about 4.1 for the three finest meshes. Clearly, exploring finer meshes would have allowed a more obvious grid independence, but at the price of a higher computational cost. However, its opportunity would be reduced bearing in mind that the scope of the CFD framework subject of this thesis is the prediction of hydro-abrasive wear rather than the accurate determination of difficult-to-measure turbulence characteristics of the jet flow. For this reason, the section 4.3 will show the independence of impact statistics with respect to the considered grid, which is the most relevant parameter for determining erosion. Thus, the variability of k on the finest meshes could be accepted.

This is even more true as the velocity magnitude (the velocity profile along a significant section is shown here) in Figure 4.5c exhibits the same qualitative trend for all the different meshes, and the curves basically overlap for Grids 4 to 7. Also the profiles of k in the same section in Figure 4.5d show the same trend for all the different meshes. However, the two peaks in the k distributions are rather grid dependent. These two peaks that are the one observed in Figure 4.5d are other than those due to the boundary layer and the interface between the jet and the surrounding still water. It is especially the second peak, which is particularly steep, that is very sensitive to the grid used, which makes it difficult to accurately predict its. Anyway, it can be seen that in the more refined Grids (from Grid 4 to Grid 7) the peaks get closer than in the coarser ones.
In conclusion, it is possible to say that the solution of this problem is grid independent for the four finest meshes that will then be considered in the following sections. In fact, for these cases, the analyses will be retraced for these Grids, after which the most appropriate grid will be selected from them upon further analysis to calculate the impact statistics. however, even in this case the statistics will be compared with those of other meshes to reduce the computational cost.

4.1.4. Sensitivity to the turbulence model

Having assessed that the CFD solution is numerically converged, it was decided to investigate the actual impact of the choice of the turbulence model on the simulation results. A comparison of different turbulence models was therefore made to see if they all produce broadly the same results. Conversely, understanding which model is the most appropriate for the case study under investigation would require an experimental validation. Since carrying out an experimental campaign was not feasible in the context of this thesis, a comparison was made only with respect to findings reported in the published literature for similar cases. The lack of information did not allow reproducing exactly the literature cases and, therefore, the comparison made was mostly qualitative than quantitative in nature. Thus, the goal that could be reached was to understand up to which extent the results are affected by the model considered, and whether some models are "better" or "worse" than others. The chosen models are the standard $k-\varepsilon$, the $k-\varepsilon$ Realizable, the $k-\varepsilon$ RNG, and the $k-\omega$ SST which were presented in section 3.1.3.

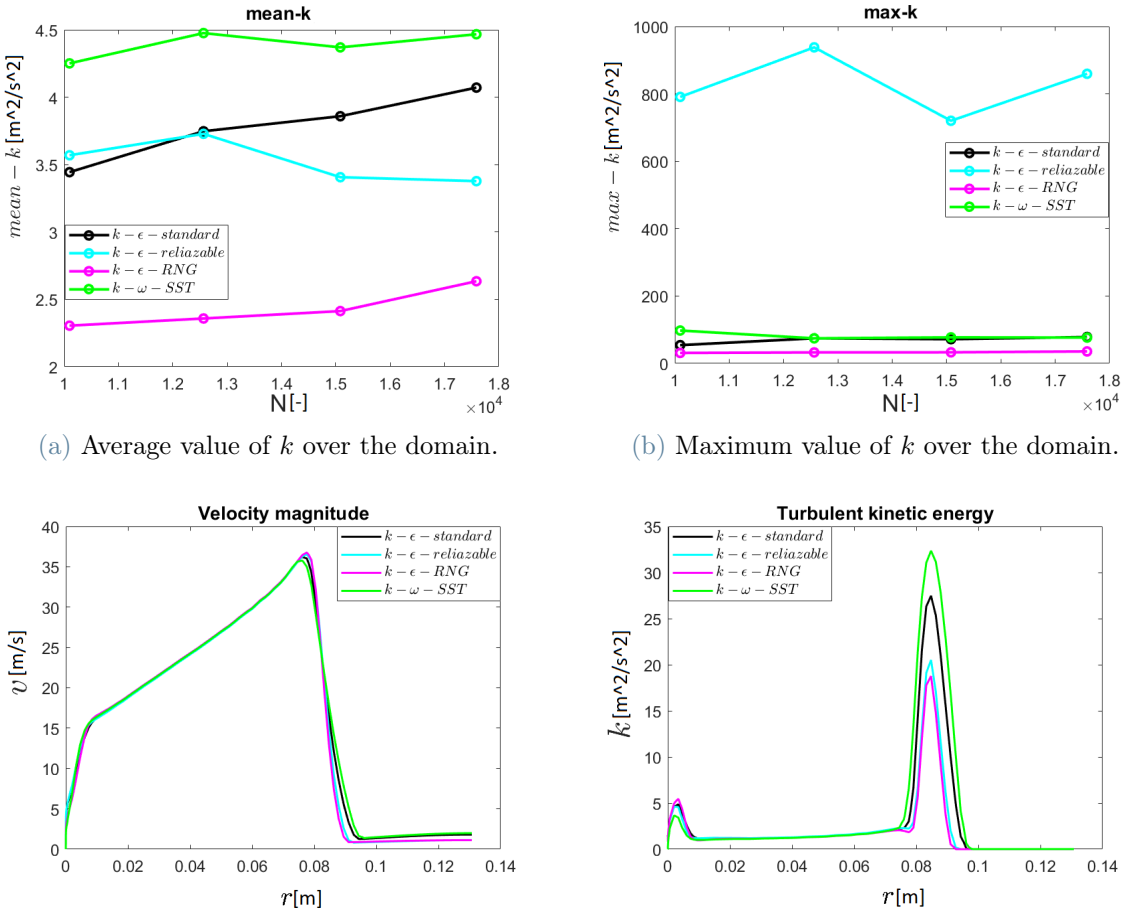

(a) Average value of k over the domain.

(b) Maximum value of k over the domain.

(c) Velocity magnitude over the n-axis (Grid 7).

(d) Turbulent kinetic energy over the n-axis (Grid 7).

Figure 4.6: Comparison turbulence.

The comparison of the turbulence models, shown in Figure 4.6, was done by considering the four most refined meshes (from Grid 4 to Grid 7), and the same target parameters of the grid independence study. The results obtained along the n-axis for Grid from 4 to 6 has been reported in Appendix A.In this way, in addition to checking a comparison of turbulence models, there is also a comparison for different meshes, in order to be sure that the result does not depend on the choosen Grid. The maximum value of k in Figure 4.6b seems to be comparable in all the models except for the $k-\varepsilon$ Relizable. Anyway since the mean value is similar to that of the other models as shown in Figure 4.6a this doesn't show really a different behaviour in this model.
Conversely, the maximum value of k predicted by the $k-\varepsilon$ Realizable is much higher than those estimated by the other turbulence models, which is more similar in terms of order of magnitude.

For graphical clarity, only the velocity profile of Grid 7 has been reported in Figure 4.6c. The results of the other cases have been reported, in the Appendix A, but the same considerations can be performed for these Grids. The velocity profile along the n-axis as shown in Figure 4.6c is predicted in the same way by all the turbulence models, both qualitatively and quantitatively. The greatest deviations are observed at the interface between the jet and the surrounding still water. This is not surprising, as it is the region where the k peak is located, which is estimated differently by the various models and being steep is more subject to variation due to model change (Figure 4.6d).

And, indeed, looking at the profiles of k over the same line in Figure 4.6d, it can be seen that the qualitative trend is captured in the same way in all the models but the magnitude of the peaks (in particular the second one) is strongly on the model considered. Indeed the $k-\omega$ SST shows a highest second peak while the $k-\varepsilon$ RNG the lowest one.
The results shows that the turbulence model has little effect on the mean velocity field, which is the "primary" variable for determining particle trajectories. Instead, it has a greater effect on k, which, however, has no direct effect on particle trajectories. In fact, if turbulent scattering is not activated like the case under analysis, the value of k does not go to have a direct impact on them. In light of the considerations above, the turbulence model used in the remainder of the simulations is the standard $k-\varepsilon$, which, in addition to be the simplest, in the comparisons shown in Figure 4.6 produces a solution which lies in the middle.

4.1.5. Comparison against literature results

As already mentioned, a validation in strict sense could not be carried out since experimental testing was unfeasible. Thus, reference was made to numerical results reported in the literature. Additionally, due to the lack of information and/or of suitable modelling tools, it was not possible to reproduce the literature cases; therefore, mostly a qualitative comparison was made by referring to Figures 4.8 and 4.9, reported in [7] and [2], respectively.

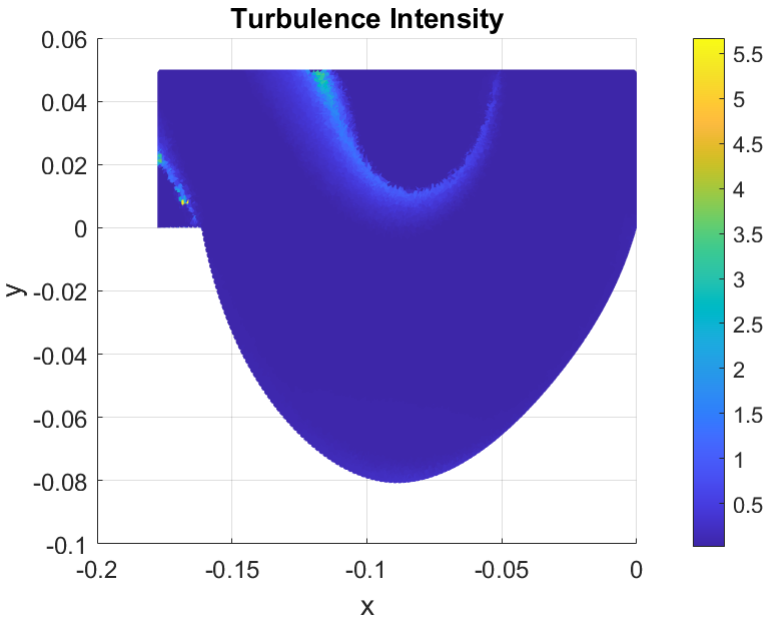

(a) Turbulence intensity from 0 to 5.5.

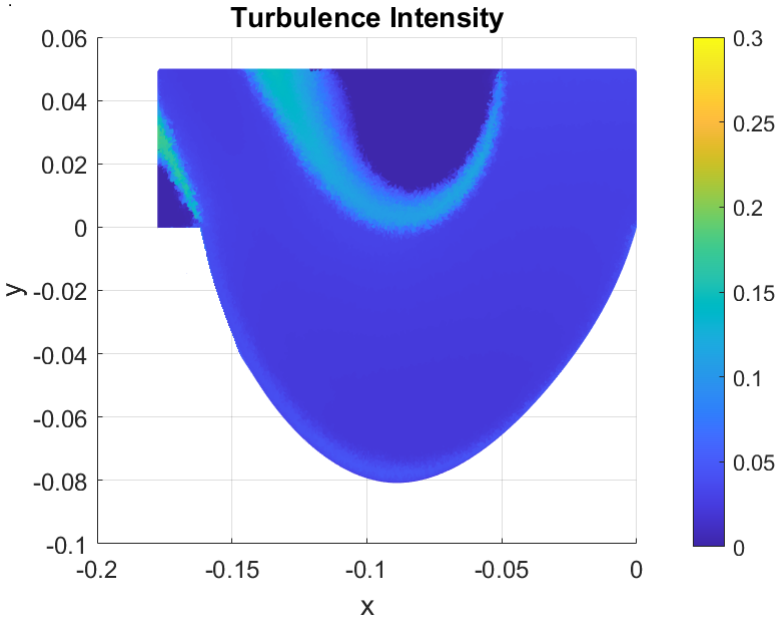

(b) Turbulence intensity from 0 to 0.3.

Figure 4.7: Distribution of the turbulence intensity obtained in the present CFD simulations.

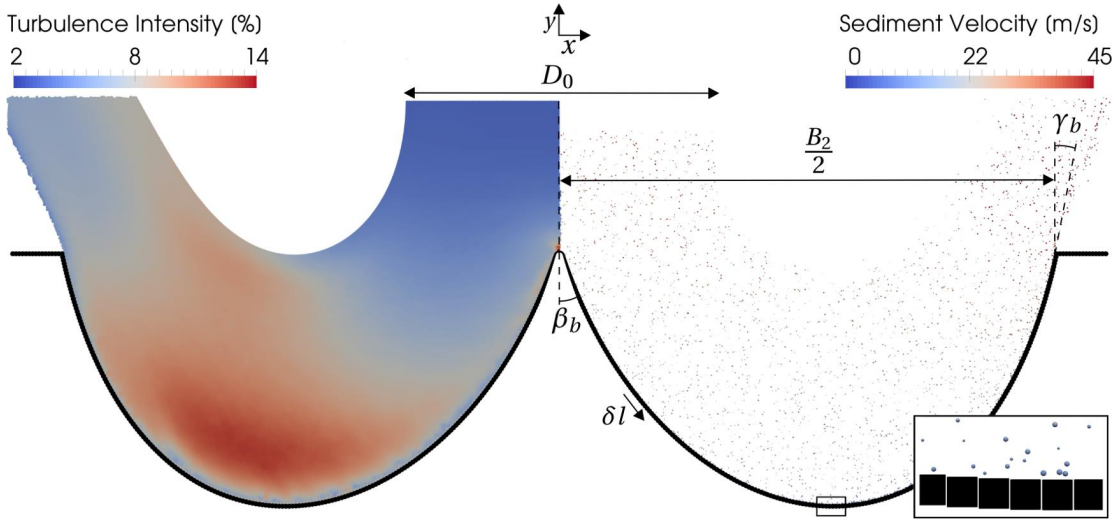

Figure 4.8: Distribution of the turbulence intensity as reported in the PhD thesis of Leguizamon [7].

Figure 4.7 represents the turbulence intensity calculated in the present numerical simulation. The color plot obtained by Leguizamon for the same variable is shown in Figure 4.8. The two color plots are not directly comparable, since use was made of a different fluid dynamic model. In fact, Leguizamon used a Lagrangian to simulate the flow of water in the vacuum, and he also accounted for the effect of the sediments on the fluid flow using the two-way coupled particle tracking. In the present simulation, use is made of a single-phase Eulerian model to simulate the water jet in still water. In Figure 4.7, the turbulence intensity shows some peaks in the region where the moving water is in contact with the still water, that were not detected by Leguizamon in Figure 4.8. This is reasonable because, in the simulation performed by Leguizamon, the water jet is in the vacuum. At the same time, a second region of higher turbulent intensity is found close to the blade in both Figures 4.7 and 4.8, where the turbulent kinetic energy is relatively high and the velocity is small. Looking at Figure 4.7 it is possible to say that the turbulence intensity that is defined in equation 3.10 is higher in the region where the still water is in contact with the moving water. This is reasonable because the frictional stress between water and air generates turbulence. Looking at Figure 4.7b is possible to see that near the wall the turbulence intensity is higher because of the boundary layer. However, the values obtained are lower than the reference values in the figure of 4.8. This is probably due to the fact that in that case the flow is simulated with particles inside which generate

turbulence, or also due to the different fluid dynamic model considered. Moreover it is not clear how the TI is defined in the Phd thesis of Leguizamon [7].

From the right hand side of Figure 4.8, it is possible to notice that, in the simulation of Leguizamon, the sediment velocity ranges between 0 to 45 m/s, reaching the maximum value at the bucket outlet angle. The color plot of the fluid velocity magnitude obtained in the present calculations, already shown in 4.3a, indicates the range from 0 to 51.8 m/s, with an increase near the bucket outlet angle. Clearly, a direct comparison of the two Figures is not possible as the variables are different (fluid velocity versus sediment velocity). Nonetheless, the results obtained in the present simulations could be reasonably claimed comparable with those of Leguizamon. The comparison made here is geometrically consistent because the domain of the Figure 4.6 has been reproduced exactly. The selected boundary conditions are also the same. Therefore, the two graphs are comparable.

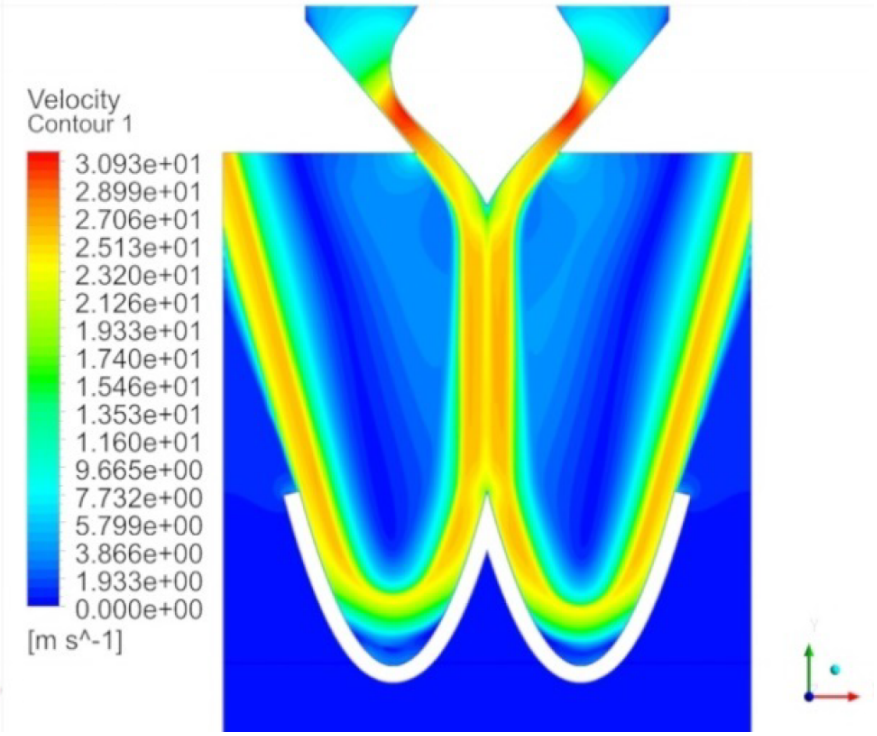

Figure 4.9: Velocity magnitude (picture from Adhikari et al. [2]).

A second qualitative comparison was made by referring to the previous Figure 4.3a and Figure 4.9 from [2]. In this case, the simulated geometries are different; whereas the geometrical settings of the present simulations are those reported in Table 4.1, those of the simulations of [2] are summarized in Table 4.3.

Name	Parameter symbol	Value	Unit
Jet Diameter	D_0	0.139	[m]
Bucket width	B_2	0.461	[m]
Bucket half-splitter angle	β_b	27.5	[°]
Bucket outlet angle	γ_b	15.0	[°]

Table 4.3: Geometric parameters from [2].

The inlet velocity could be estimated as 28 m/s from the color plot in picture 4.9, while in this thesis the inlet velocity considered i of 40 m/s. The value has been estimated from the colour plot since it has not been declared in the paper of Adhikari et al. [2] simulated the water jet in air using the VOF model coupled with the $k-\varepsilon$ Realizable turbulence model and standard wall function. The geometry of the blade, that is simulated as 2D in this case, is slightly different from the one considered in the case study of this thesis, both in terms of shape and size. For the two reasons mentioned here above, it is clear that the comparison between the results in [2] and those obtained in the present study could be only qualitative. Having said that, it is possible to see that the water velocity distribution, that is shown in Figure 4.9 and Figure 4.3a, is qualitatively similar in the two cases, approaching zero along the wall and increases rapidly moving away from it, as a result of the presence of the boundary layer. It is recalled that this comparison is weak, because it is not possible to perform a quantitative comparison. However, two-dimensional simulations on Pelton turbine blades are difficult to find in the literature.

In summary, being aware of the limitations of the comparison carried out here above, which could not be avoided due to the lack of tools and information, it could be reasonably claimed that the CFD model is capable to produce a physically sound prediction of the development of the turbulent water jet in the system.

4.1.6. Conclusion

The following considerations could be made about the findings of the submerged 2D case described above.

1. The solution is consistent with the underlying physical processes (Figure 4.3). The velocity approaches to zero at the wall and increases rapidly moving away from it showing a boundary layer as expected from fluid dynamic considerations. The turbulent kinetic energy k shows two peaks that are due to the frictional stress

between water and water and near the wall.

2. The four finest meshes considered (Grid 4 to Grid 7 in Table 4.2) produced a substantially grid independence solution (Figure 4.5). This is clearly achieved in terms of the Reynolds averaged velocity field, whereas some residual mesh effect could be seen in terms of the turbulent kinetic energy. Nonetheless the result is acceptable because the ultimate goal is to assess erosion and thus impact statistics, and these are expected to be less influenced by k.

3. The solution is not significantly affected by the turbulence model (Figure 4.6). specifically there is some influence of the turbulence model on the value of k while the velocity field is not affected by the chosen turbulence model. However since impact statistics are the most relevant parameter in this context, the most significant variable is velocity, consequently differences on k are not relevant for the purposes of this thesis.

Hence these results can be used as a starting point for the subsequent 2D simulations to avoid unnecessary computations. In particular, only the Grids 4 to 7 and the $k-\varepsilon$ standard turbulence model will be used from this point onward.

At the same time, weaknesses exists in the study described in this section. These are mainly related with the impossibility to carry out a proper validation of the CFD results. In fact,

1. The possibility of carrying out an experimental validation was precluded due to the lack of a suitable facility.

2. Reference could only be made to CFD data reported in the literature. However, as much as it would be necessary to make a comparison with experimental data, it is not possible to do so in this context because no data were found in the literature. However, the comparison could be only partial and qualitative, owing to the lack of information that allowed reproducing the actual geometries simulated in the literature, and to intrinsic differences in the fluid dynamic models. Particularly, the simulations of Pelton turbines in the literature are always two-phase, whereas the model used here is a single-phase one.

In summary, it was not possible to have a proper validation of the model used. Moreover, the choice of the turbulence models affects the distribution of k, while doesn't affect other parameters like the velocity magnitude that is mainly correlated with the particles trajectories, it is possible to say that the significant variables are not particularly affected by the chosen turbulence model. In fact since the goal of the thesis is to go to predict

erosion, the significant parameters are those related to impact statistics, i.e., particle velocity rather than turbulent kinetic energy. Consequently, some confidence can be had in the CFD model for the single-phase part.

4.2. Free water jet (two-phase flow)

Having obtained satisfactory results for the submerged jet case, in the next step a free water jet in an air environment was considered. This a two-phase flow case, where the two phases involved are water and air. The geometry of the case study is identical to that of the previous case, shown in Figure 4.1 and summarized in Table 4.1. The only difference is that now the jet is not submerged but is free.

4.2.1. CFD set up

A literature review on the simulation of flows in Pelton turbines indicated that, for simulating the free water jet in air, homogeneous models are widely used, in particular the Volume Of Fluid (VOF), previously introduced in Section 2.3.2.

More advanced fluid dynamic models are available, such as the Eulerian multiphase ones, but they are not really necessary to this case, since the VOF solves only one velocity (and pressure) field and assumes a sharp interface between the phases. Conversely, Euler-Euler models compute two velocity fields (and sometimes two pressure fields) and consider mixing between phases. However, Euler-Euler models are not used in this thesis because they have higher computational cost and are less controllable. Moreover, it must also be said that for the case study, the VOF assumptions are reasonable, because there is high velocity difference between the two phases so that the interface is sharp and there is no mixing between the phases. In addition, Eulerian multi phase models require higher computing time, as explained in [20], and they involve a larger number of uncertain coefficients, sub-models and parameters, which make the solution uncertain and difficult to control. More details can be found in [18].

The standard $k - \varepsilon$ turbulence model was chosen based on the result of the analysis performed for the submerged jet case and presented in section 4.1. Additionally, the following modelling assumptions were initially made:

1. sharp interface modelling. In Ansys fluent is possible to choose between different configurations of the interface modelling: sharp interface, sharp dispersed and dispersed. Initially since sharp interface were the default fluent option it was chosen as starting point. In particular, this option is more appropriate when the interface between two fluids is sharp, i.e., there are no bubbles/mixing between the phases. Only a transition region is created between the two fluids where they mix slightly. In any case, a comparison w.r.t. modelling parameters will be made in Section 4.2.4.

2. negligible effect of the surface tension force at the water-air interface, as a result of

the high velocity of the water jet.

The two modelling choices here above were judged a reasonable first-attempt configuration. However, a sensitivity analysis will be presented in section 4.2.4, where alternative options were explored and their impact on the CFD results was assessed. The problem was simulated as steady.

The computational domain of this case is the same of the single-phase represented in Figure 4.2, with all the geometrical features described in Table 4.1. Also the boundary conditions remain the same with the addition of the volume fractions of water and air at the inlet. In fact, since we are solving for the VOF equations instead of the RANS, it must be also specified that the volume fraction of water at the inlet is equal to 1 (as a consequence the volume fraction of air is equal to 0). In the initialization panel, the volume fraction of water was set to 0 in all the domain, which basically means that the steady-state solution will be calculated from an initial configuration in which the domain consists only of air.

Then to solve the problem the method used in this case was the PRESTO! with second order upwind for both turbulent kinetic energy and turbulent dissipation rate. The other options were the default fluent options.

4.2.2. Physical consistency of the CFD solution

As for the previous single-phase case, the physical consistency of the solution was verified by inspecting the color plots of relevant fluid dynamic parameters. In this case, however, unlike the single-phase case, a third variable is added, namely, the volumetric fraction of water.

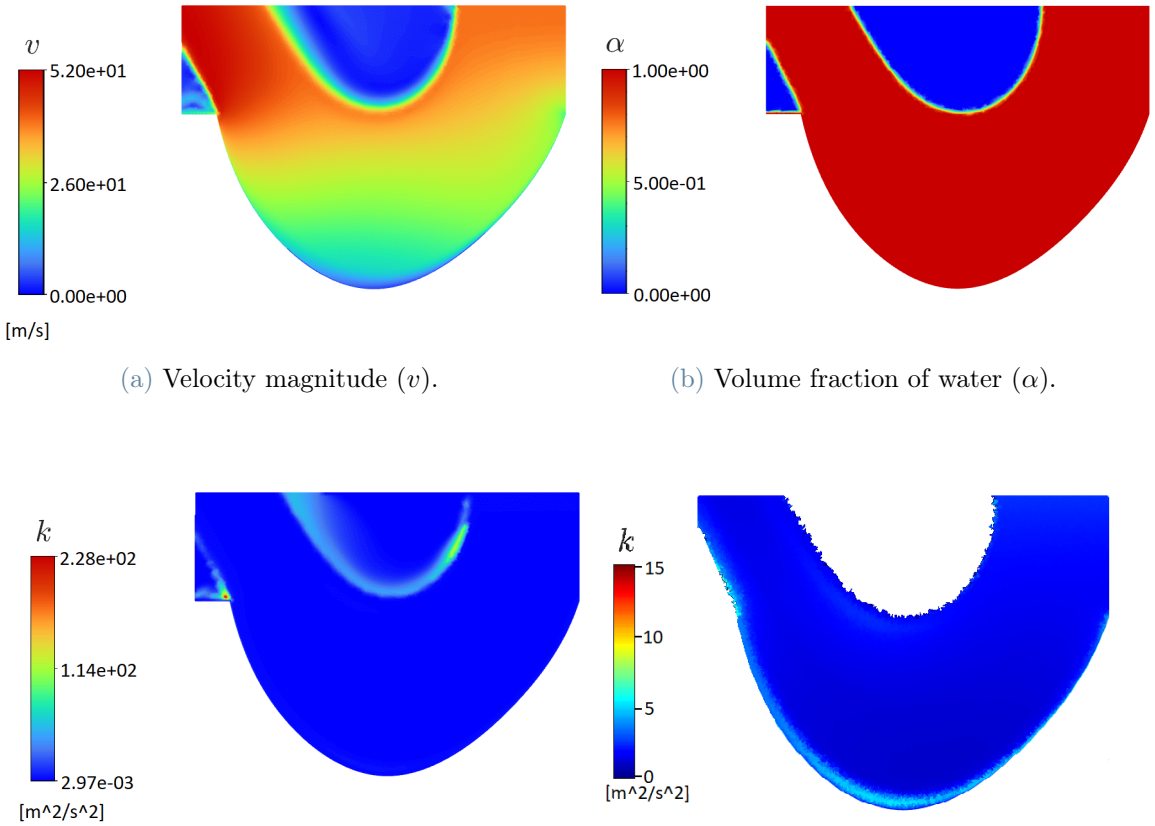

(a) Velocity magnitude (v).

(b) Volume fraction of water (α).

(c) Turbulent kinetic energy (k).

(d) Turbulence intensity considering only the water region (k).

Figure 4.10: Physical consistency VOF (results obtained with Grid 7).

In Figure 4.10 is possible to see that the results are similar to the previous case. In particular, the high velocity at the inlet implies that the surface tension between water-air or water-water does not significantly affect the velocity field. In this case another parameter of interest is the volume fraction of water. Yet at first glance there is a clear connection between the color plots of the velocity magnitude (Fig. 4.10a) and of the water volume fraction (Fig. 4.10b). This indicates that, not surprisingly, the highest velocities are those characterizing the water jet, which, in turn, mildly drags the surrounding air. Thus, as shown in figure 4.10a the water drops downward and then deflects laterally. This turns out to be zero at the wall due to the no slip boundary condition, and increases rapidly moving away from it. Thus, a boundary layer is observed, as expected from fluid mechanics considerations. At the same time, the volume fraction of water corresponds to the region where the velocity is not zero, because the air is stationary and the water is moving. Also in this case, the kinetic energy (Fig. 4.10c) turns out to be higher at the wall, due to the boundary layer between the water jet and the blade, and at the

interface between the water jet and the surrounding air, due to the inter-phase friction. However, the increase in turbulent kinetic energy near the wall is not visible in this plot. For this reason, the turbulent kinetic energy of water alone was also shown. In particular as it is possible to see in Figure 4.10d,where it is shown only the turbulent kinetic energy of the water, the value of k turns out to be higher near the wall, as expected from fluid dynamic considerations. So the numerical results are consistent with the underlying physical phenomenon.

4.2.3. Convergence assessment study

Like in the single-phase case a study was carried out to assess the numerical convergence of the simulation results, namely, focusing on both the convergence with respect to the iterative solution algorithm and the convergence with respect to the computational mesh. Also in this case the residuals are set to 10^{-5} and the maximum number of iterations to 5000 that is sufficient for the normalized residuals to fall below the chosen threshold for all meshes.

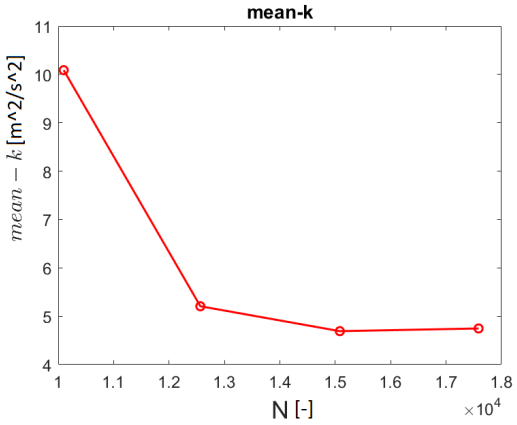

(a) Average value of k over the domain.

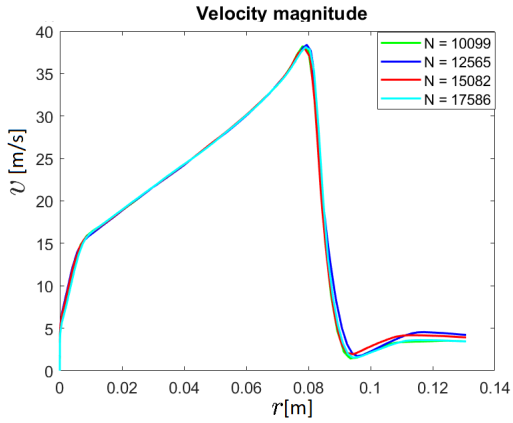

(b) Velocity magnitude over the n-axis (Grid 7).

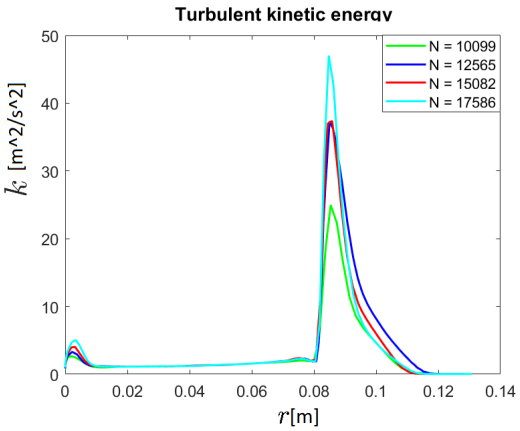

(c) Turbulent kinetic energy over the n-axis (Grid 7).

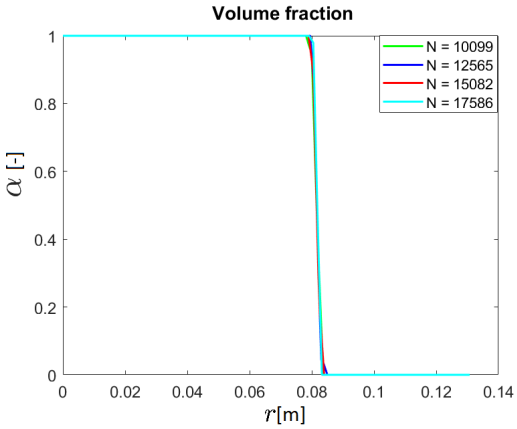

(d) Volume fraction of water over the n-axis (Grid 7).

Figure 4.11: Grid independence.

In Figure 4.11 are reported the plots for all the parameters of the grid independence study. It is possible to see that the mean value of k (Fig. 4.11a) over the entire domain reaches a stable value for the four finest meshes (from Grid 4 to Grid 7 introduced in Table 4.2).For the following considerations we will refer to the figure 4.2 in which both the n-axis and the r coordinate are introduced. The velocity along the n-axis (Fig. 4.11b) results to be very similar in all the meshes, while k along the same axis (Fig. 4.11c) shows the same trend but the maximum values does not reach a stable value. This happens because, as already explained in the single phase case in Section 4.1.3, the curve is very steep so that this value is strongly dependent on the mesh considered. Refining the grid, the peak in k is likely to be better captured. Compared to the single-phase case, in the present two-phase one another target parameter is taken into account, namely, the volume fraction of water

along the n-axis shown in Figure 4.11d. This plot shows that the volume fraction profiles are substantially indistinguishable for all the meshes. In conclusion it is possible to say that the Grids from 4 to 7 4.4 are grid independent w.r.t. all the parameters despite of k along the n-axis (Fig. 4.11c). However this value doesn't directly affect the impact statistics that are the relevant parameter for the computation of the erosion. In this way they can be considered grid independent. In the following sections they will be considered. All four will then be considered for further analysis.

4.2.4. Sensitivity of the CFD results on modelling parameters.

Having assessed that the numerical convergence of the CFD solution, its sensitivity upon difficult-to-decide settings and parameters of the VOF model must be investigated. Such an analysis is necessary to establish the impact of such critical modelling features, as a necessary step for guaranteeing the reliability of the numerical results. The sensitivity study was carried out in two steps, by considering two critical features of the VOF model one at a time. The first relates with the inclusion of the surface tension effects in the momentum equation. The options available in the Ansys Fluent code are:

1. no surface tension effects
2. surface tension with continuum surface force
3. surface tension with continuum surface stress

considering, for all this cases, the sharp interface modelling (as explained in Section 4.2.1). Afterwards, an analysis was carried out by varying the modelling of the water-air interface, considering the following options available in Ansys Fluent:

1. sharp
2. sharp/dispersed
3. dispersed

In all these cases, no surface tension effects have been accounted for.

Influence of the turbulence model

At this point, a turbulence model analysis would need to be performed again. The problem to be solved is different from the previous one so, in principle, all the analysis should be redone. However, looking at the results obtained for the velocity field and turbulent

kinetic energy in the single-phase an in the two-phase case, they do not particularly differ. Also in this case the trend is the same, and the first peak coincide. In conclusion, the single phase an the two-phase case do not show significantly different results, so that it can be expected that the comparison of the turbulence models in this case will show the same results of the previous case. As a result, in light of the sensitivity analysis carried out in Section 4.1.4, the turbulence model that will be considered here is he standard $k-\varepsilon$ without performing further analysis. Moreover it is recalled that the choice of the turbulence model does not practically affect the Reynolds-average velocity field, that is the most relevant parameter for the computation of the impact statistics necessary for the computation of the erosion.

Influence of accounting for surface tension effects

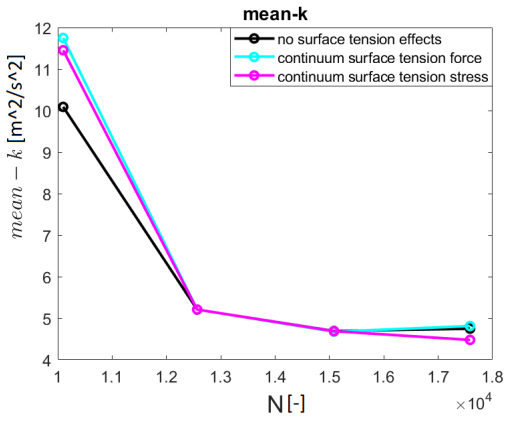

(a) Average value of k over the domain.

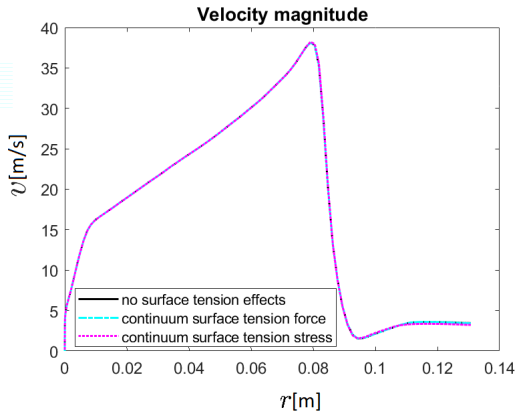

(b) Velocity magnitude over the n-axis (Grid 7).

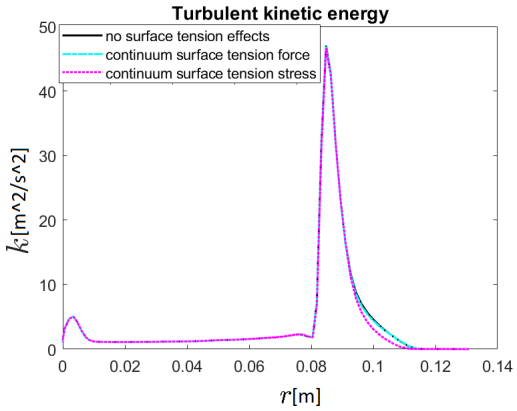

(c) Turbulent kinetic energy over the n-axis (Grid 7).

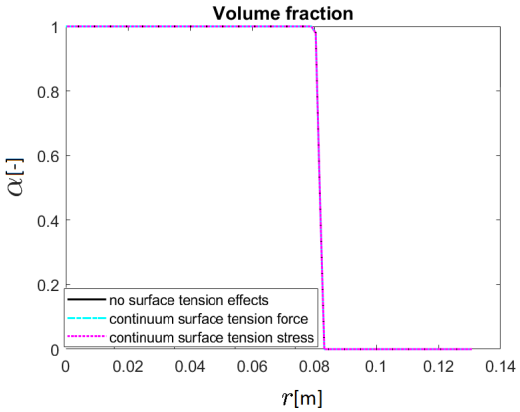

(d) Volume of fluid magnitude over the n-axis (Grid 7).

Figure 4.12: Comparison w.r.t. the surface tension modelling parameter.

In Figure 4.12 and in Figure 4.13 are reported the velocity magnitude, the turbulent kinetic energy and the volume fraction along the n-axis for Grid 7 (for graphical clarity). For the other Grids the values are reported in Appendix A, but the trend of this parameters is the same. The same considerations can be performed in this cases. In order to compare the surface tension models, including the absence of surface tension effects, the same target parameters of the grid independence study have been considered like the average value of k and the values of velocity magnitude, turbulent intensity and volume fraction over the n-axis (defined in Figure 4.2). In particular it is possible to see, considering the mean value of k (Fig. 4.12a) that the trend is the same and, for the most refined mesh, the values are very similar. The other parameters like the velocity magnitude, the turbulent kinetic energy and the volume fraction along the n-axis (Fig. 4.12b, 4.12c, 4.12d), are almost coincident. In particular in the Figures 4.12b and 4.12d they are indistinguishable. Only through magnification can the presence of the three curves be grasped. Thus it can be said that ignoring for surface tension effects or accounting for them through the two modelling options made available in Ansys Fluent does not produce any significant change to the solution. This further confirms that the high velocity difference between the two phases imply that the surface tension do not play a key role (this could be interpreted by the results obtained). Thus, in the following analyses, the effect of surface tension will be no longer considered.

Influence of the modelling of the air-water interface

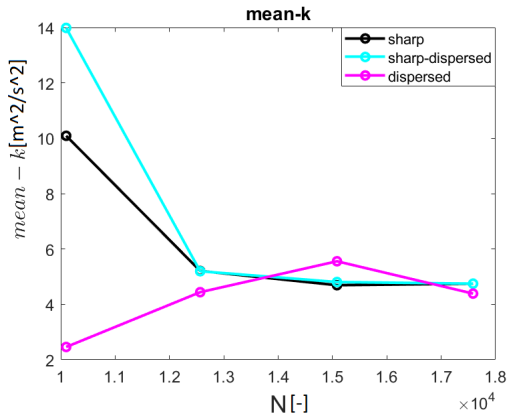

(a) Average value of k over the domain.

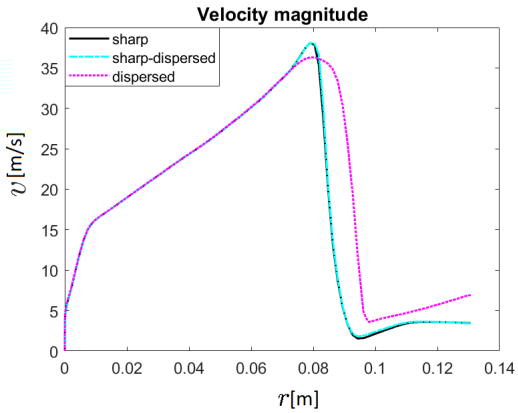

(b) Velocity magnitude over the n-axis.

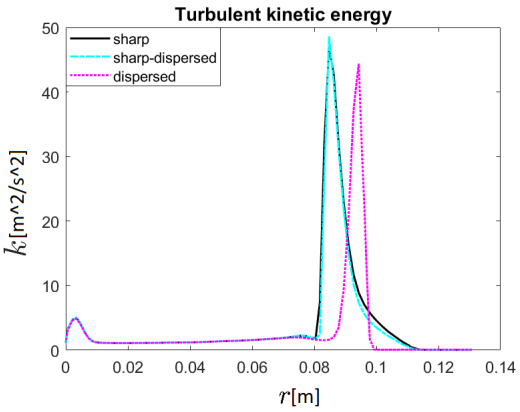

(c) Turbulent kinetic energy over the n-axis (Grid 7).

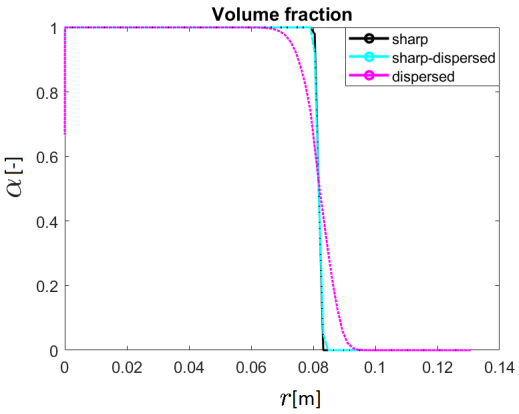

(d) Volume fraction of water over the n-axis (Grid 7).

Figure 4.13: Comparison w.r.t. the interface modelling parameter.

Figure 4.13 model comparison plots with different interface modeling are shown. Also in this case the results for the other Grids are reported in Appendix A. In Figures 4.13b, 4.13c, 4.13d are reported the velocity magnitude, the turbulent kinetic energy and the volume fraction along the n-axis. Here is possible to see that the VOF with sharp interface, and VOF with sharp-dispersed interface are comparable, while the VOF with sharp-dispersed interface shows in the values of velocity, kinetic energy and volume fraction along the n-axis a different behaviour. In order to select the most appropriate option even without experimental data for validation, reference was made to physical considerations. In this case, the two fluids are not one dispersed into the other, as it is possible to see from the volume fraction in Figure 4.10b, so the sharp interface appears the best choice from a modeling point of view, as explained in [8]. So, the choice will be the VOF with

sharp interface modelling.

4.2.5. Comparison against literature results

To validate this model it has been considered the Figure 4.8 compared with Figure 4.14.

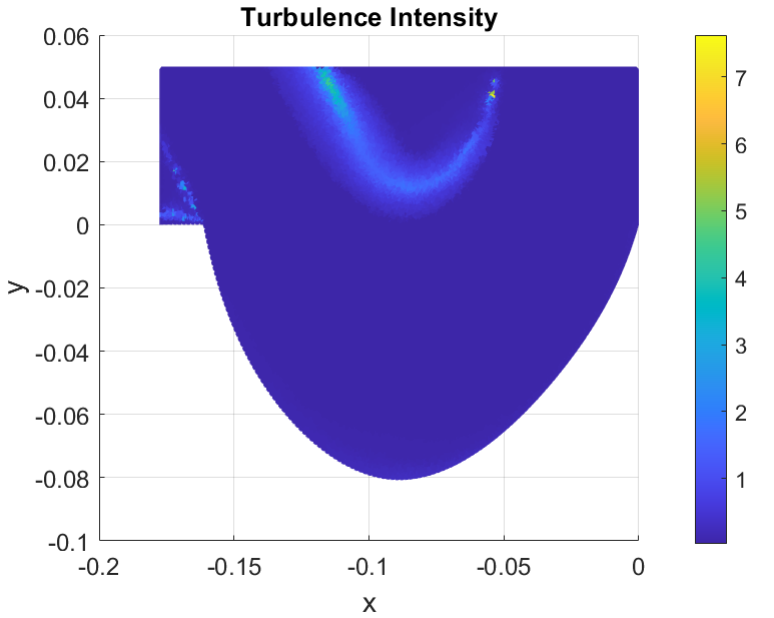

(a) Turbulence intensity of the whole domain.

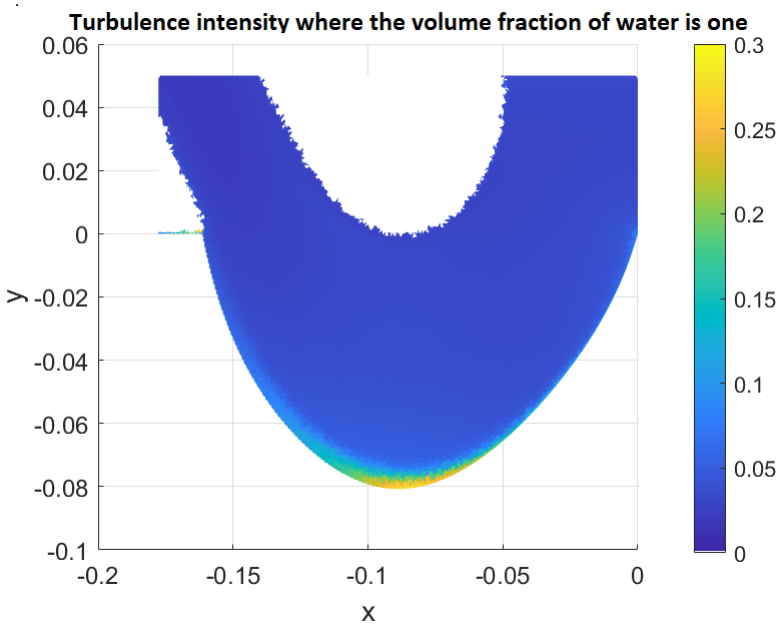

(b) Turbulence intensity where the volume fraction of water is one.

Figure 4.14: Turbulence intensity VOF.

Figure 4.14 shows both the turbulence intensity of the whole domain (Fig. 4.14a) and the turbulence intensity considering only the portion of the domain where the volume fraction of water is one (Fig. 4.14b). In this case, since the water jet is in air, turbulence is produced by the frictional stresses between water and air at the interface. Therefore, the turbulence intensity is greater near the interface than in the rest of the domain. In addition compared to the single-phase case here the peaks are higher both near the wall and near the water-air interface. In particular, near the interface is higher in the air region. This comparison can be seen from Figures 4.14 and 4.7. Then also the values near the wall are higher than the values in the internal region, because of the zero velocity at the wall (no slip boundary condition). However it is difficult to recognize the higher turbulence intensity in the near-wall region from Figure 4.14a, because the values are significantly lower than those close to the interface in the air-region. For this reason in Figure 4.14b the values have been restricted from 0 to 0.3. In this way it is possible to see the second peak of turbulence intensity near the wall. As a reference configuration for this features of the CFD solution, one could consider the results obtained by Leguizamon (Fig. 4.8) and already presented and discussed in the single-phase case. These values, however, although higher than in the single-phase case, are lower than the reference values (Fig. 4.8). This is probably again due to the difference in the fluid dynamic model used and the fact that in this case simulation occurs with the particles inside.

Reference could be made to the same literature results considered in the single-phase case also when referring to the velocity magnitude. In particular, Figure 4.10a can be compared with Figures 4.9 [2] and 4.8 [7]. In the Figure of Leguizamon, what we can infer from the plot is not the velocity of the fluid but that of the particles.

Also in this case the comparison between the results in [2] and those obtained in the present study could be only qualitative. In fact, it is possible to see that the water velocity distribution, that is shown in Figure 4.9 and Figure 4.10a, is qualitatively similar in the two cases, indeed it approaches to zero near the wall and increases rapidly moving away from it, due to the presence of a boundary layer.

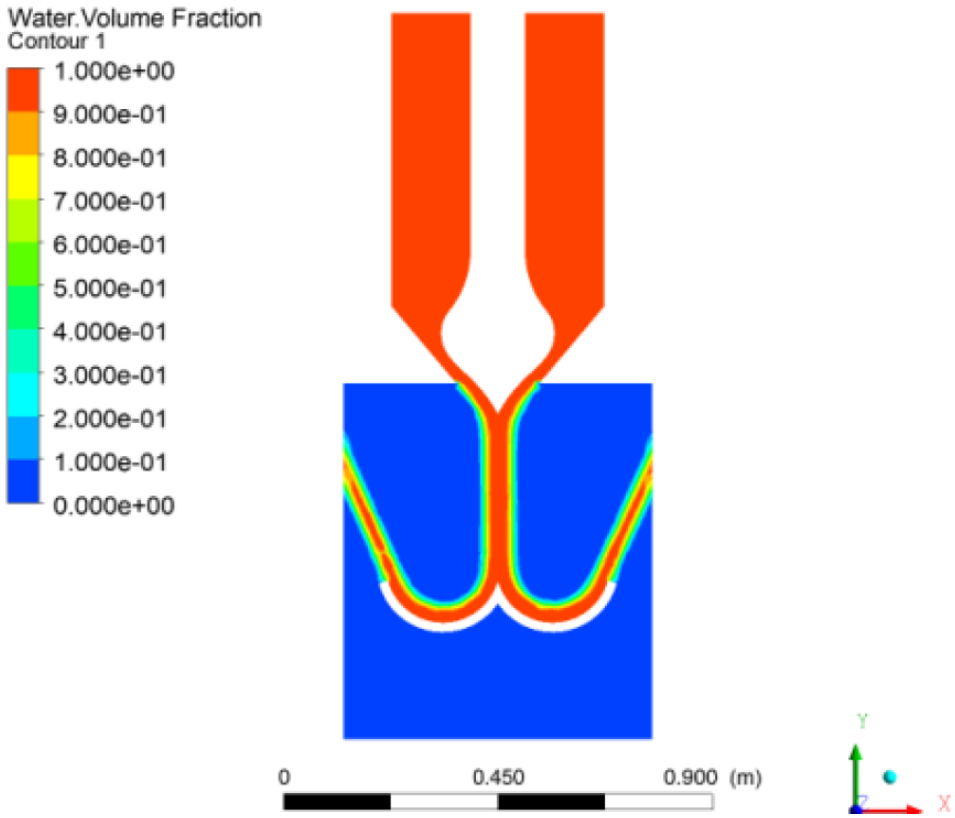

Figure 4.15: Volume fraction (picture from Adhikari et al. [1]).

Figure 4.15 from [2] shows the results for the volume fraction in the case explained in section 4.1.5 with all the features described in 4.3.

In the two phase case validation can also be done by considering the volumetric fraction. So, comparing Figure 4.15 with Figure 4.10b it is possible to see that these parameters is predicted in the same way in the two cases. Again this plot is taken from [2] and it was not considered in the previous case because the volume fraction is a specific parameter of the two-phase model. The pattern of the volume fraction is definitely not surprising. Since, furthermore, not enough information was given in [1] to reproduce the geometry simulated by those authors, no more than a qualitative validation could be made. Having said that, it appears that the VOF model is capable in providing reasonable prediction of the behavior of the water jet hitting the turbine blade.

4.2.6. Conclusion

As a conclusion of the two-phase flow study, the following considerations can be made.

1. From a qualitative point o view, the VOF solution is consistent with the underlying physical phenomenon. Indeed is possible to see in Figure 4.10 that the water comes

down and then deflects laterally. The velocity approaches to zero near the wall and then increases rapidly moving away from it. The turbulent kinetic k energy along the n-axis shows two peaks, near the wall and near the interface of water and air (In the region of the air). This is because air is stationary and is set in motion by water, and this mechanism generates turbulence.

2. The solution of the problem is grid independent for all the Grids considered (Table 4.4), as shown in Figure 4.11. So Grid 5 will be used in the following computations as a good compromise between accuracy and computational burden. Specifically in comparison with the single-phase case, no particular differences were found, either in the number of iterations required for convergence or in the choice of Grids (although in this case Grids 4 through Grid 7 were considered in Table 4.2).

3. The velocity results obtained in the two-phase 4.2.2 case are similar to the results obtained in the single-phase case 4.1.2. In fact, the velocity has the same profile qualitatively, and the maximum values are 51.8 m/s (Fig. 4.3a)in the single-phase case and 52 m/s 4.10a in the two-phase case. As for the turbulent kinetic energy, on the other hand, this turns out to be much higher in the two-phase case than in the single-phase case, although qualitatively the two profiles turn out to be similar. In fact, the maximum turbulent kinetic energy in the two-phase case (Fig. 4.10c) is reached in the region of air in contact with water and is 228 m^2/s^2 while in the single-phase case (Fig. 4.3b) it is reached in the region where still water is in contact with moving water and is 78 m^2/s^2.

4. The comparison between the solutions obtained with different modelling parameters indicated that including surface tension effects in the momentum equation is not necessary for the problem under consideration (Fig. 4.12). Similarly, the "sharp interface" modelling option seems the most appropriate one (Fig. 4.13)

5. Qualitatively, the VOF solution is comparable to that of other numerical simulations reported in the literature, although qualitative differences from the Leguizamon solution were found in terms of turbulent intensity.

In relation with the last comment, it might be taken into account that, as already remarked for the single-phase comparison, no experimental validation is possible owing to the lack of suitable experimental data. Thus, the comparison could be made only with respect to other numerical results. In addition, reproducing exactly another numerical case is not possible owing to the lack of necessary information.

In summary, it was not possible to have a proper validation of the model used, but it

is possible to have some confidence that the present two-phase fluid dynamic model is suitable for proceeding with the tracking of the sediment trajectories and the estimation of hydro-abrasive wear.

4.3. Sediment-laden, free water jet (three-phase flow)

As a final step, sediments are injected into the domain and their trajectories are tracked. As already explained in Section 3.3, the low sediment concentration considered in this test case, equal to 0.1% as typical of turbine wear events (the reference value was taken from [7]), enables the possibility to make one-way coupled Lagrangian tracking.

4.3.1. Particle tracking model and procedure

Owing to the one-way coupling regime assumption, particle tracking was performed injecting the particles over the VOF solution previously calculated, which was no longer changed. Particularly, the VOF solution obtained on Grid 5 (Table 4.2) was considered, as it proved adequate to produce grid-independent fluid dynamic results in both the single-phase and two-phase cases. However, as it will be mentioned later in the present section, additional mesh sensitivity studies were carried out to prove the suitability of the mesh for the reliable estimation of particle-related variables.

Steady particle tracking was carried out. In this case the particles equation of motion presented in Section 3.3 are steady state. The tracking of the particle trajectories was performed using the Discrete Particle Model (DPM) of Ansys Fluent, which solves the Lagrangian equations of motion for every computational particle, as already explained in Section (3.3). The considered forces acting on the particles were the drag force (3.19) and the pressure gradient force 3.20. A particle spherical coefficient of 0.76 was considered, because is a characteristic value of silica sands with intermediate sphericity.

The "File" injection option of Ansys Fluent was used to define the initial conditions from which the trajectories were calculated. This requires uploading to the software a file with the extension .inj in which the particle input conditions are entered. The initial positions of the particles were generated randomly with Matlab. Specifically for the stationary case, the spatial coordinates (x, y, z), inlet velocity (u, v, w) and mass flow must be entered in the injection file. In particular in a 2D case like the one under analysis the z and w are set to zero. However they are required in the injection 'File'.

The routine "Sample tracking" of Ansys Fluent was used to produce a file, with extension .dpm, containing some particle-related variables at the stage of their impingement against

the wall of the blade. These data includes the position of the impact and the particle velocity components. These data were then imported and post-processed using dedicated Matlab routines.

4.3.2. Physical consistency of the DPM solution and evaluation of the particle-wall impact statistics

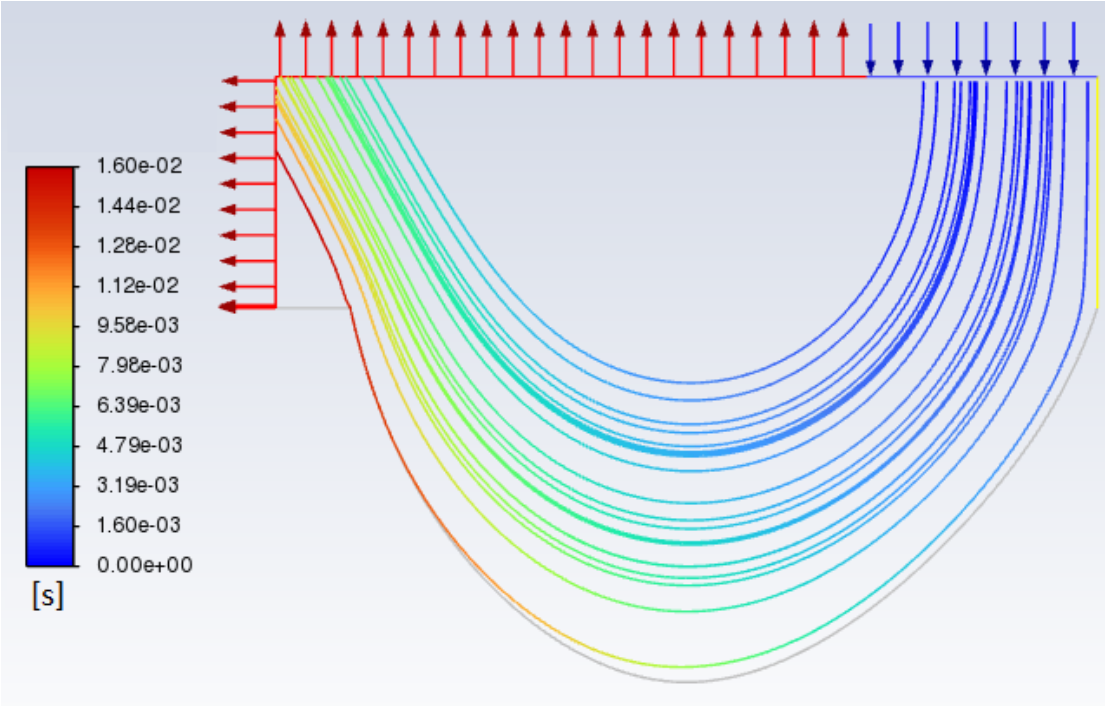

Figure 4.16: Particles trajectories. The variable under analysis is the particle residence time.

In Figure 4.16 is possible to visualize the particles trajectories computed using 50000 particles. Here is possible to see that particles follows the fluid motion.

However, the particle-related variables of most interest for the evaluation of hydro-abrasive wear are the particle-wall impact characteristics, namely, the location of the impacts (x_{imp}, y_{imp}), the impact velocities (v_p), and the impact angles (θ_p). Since erosion is the result of a high number of impacts, the particle-wall impact characteristics were estimated in a statistical manner. Statistics are calculated by dividing the wall into a number of Δs, that is, the wall is divided into N parts, each of which is Δs long. Within each Δs the average velocity and average angle are calculated, as well as the number of impacts. It is reiterated that, in the "one-way" coupling regime, the number of trajectories calculated is arbitrary because they represent parcels and not physical particles.

It is remarked that statistics should be presented in the form of bar graphs, because each value refers to a specific Δs. This representation was chosen for a more explanatory graphical display.

Initially, the wall of the blades was divided into 20 sections each one of length $\Delta s = 0.0121$ m and the number of calculated trajectories was 50000. The particle-wall impact statistics were calculated as follows:

1. The mean velocity is computed as mean of all the impact velocities along a Δs
2. The mean angle is computed as mean of all the impact angles along each Δs
3. Then the number of impact per linear metre is computed as the number of impacts in each section.

All these quantities was then divided by the number of trajectories traced.

The obtained results are shown in Figures 4.17, 4.18, 4.19.

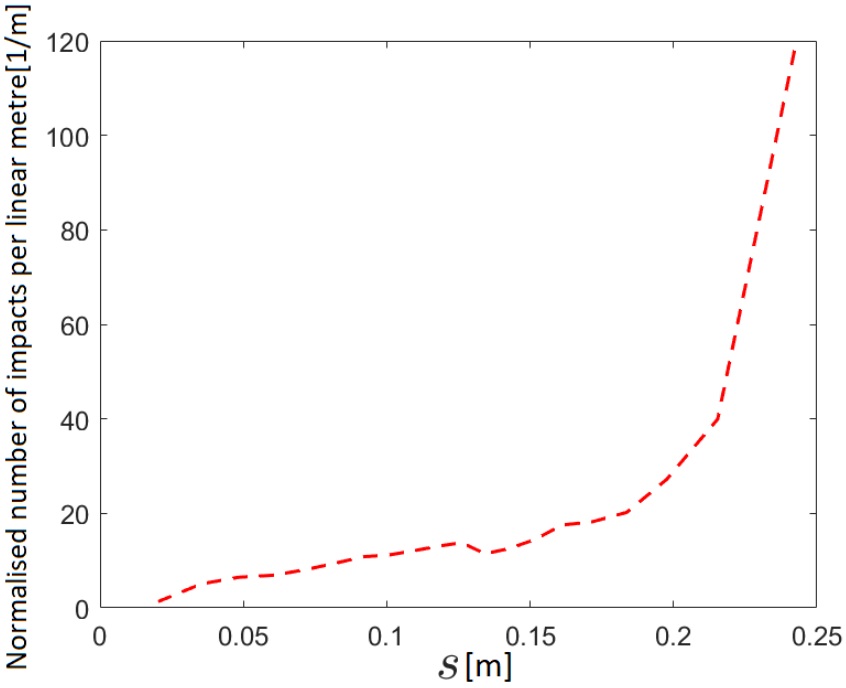

Figure 4.17: Comparison of the number of impacts per linear metre normalised to the number of particles and the Δs.

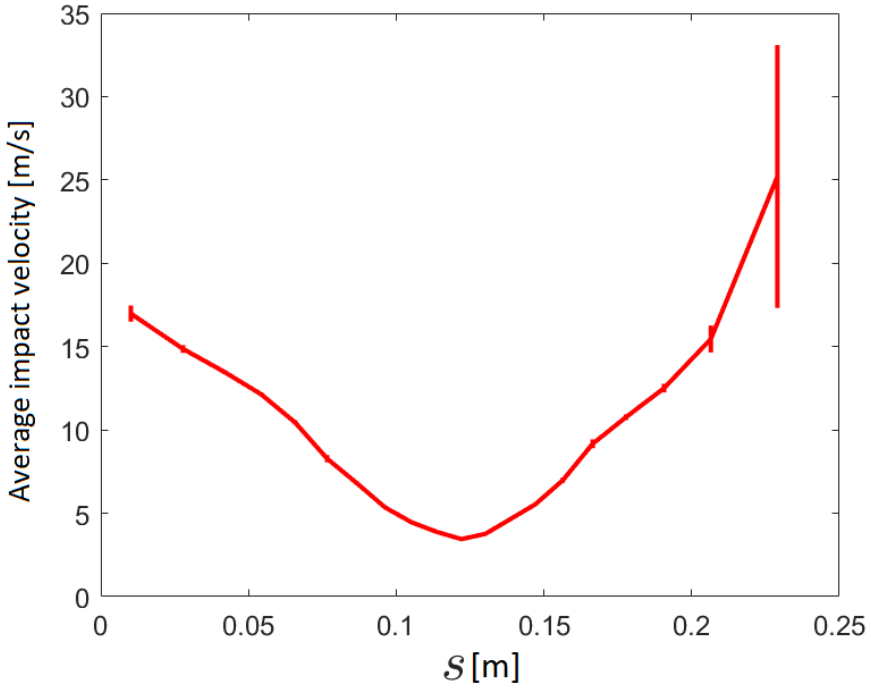

Figure 4.18: Behaviour of the mean modulus of impact velocity along the target wall.

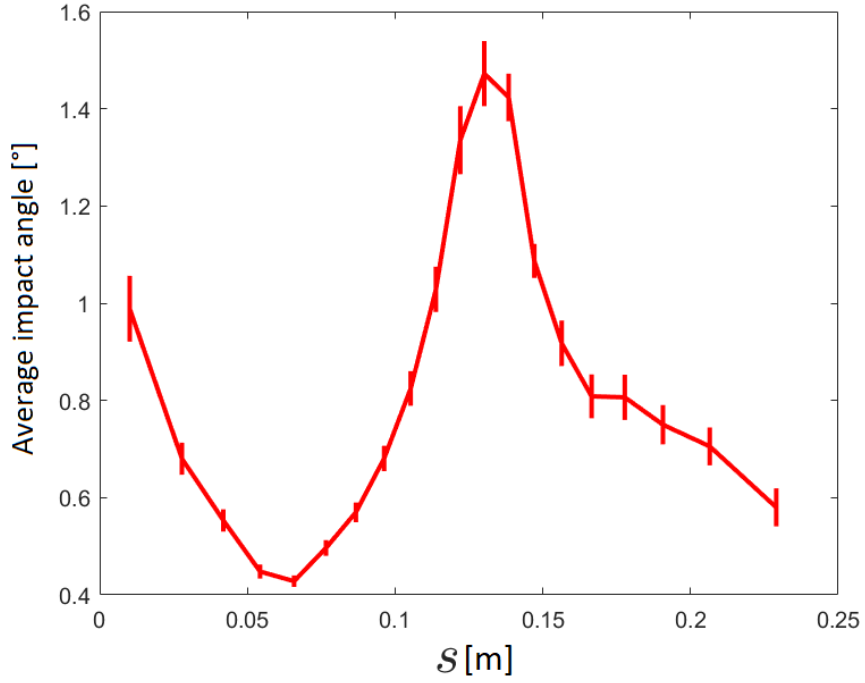

Figure 4.19: Behaviour of the mean impact angle along the target wall.

With regard to the number of impacts 4.17, it can be seen that this increases towards the

end, i.e. at the exit of the bucket.

The average impact velocity 4.18, on the other hand, decreases and then increases again at the exit of the bucket, in accordance with the fluid problem, where in particular the variance increases consistent with the fact that near the exit the number of impacts increases.

Finally, with regard to the impact angle 4.19, it can be seen that the average impact angle is low, i.e. the impacts are almost tangential. In particular, the angle is higher in the central region, where the slope of the wall changes.

4.3.3. Sensitivity of the particle-wall impact statistics with respect to numerical parameters

The significance of the particle-wall impact statistics was assessed by investigating their sensitivity upon numerical parameters.

These include, firstly, the computational mesh. It has already been proved that the used mesh (Grid 5 in Table 4.4) allows for a grid independent estimate of key fluid dynamic parameters such as mean velocity and volume fraction. However, for other parameters, such as k, no real grid independence was observed (the peak of k depends on the chosen grid, see Fig. 4.11c). So, to understand the actual impact of such residual grid dependence on the wear estimates, a preliminary analysis was carried out to investigate the effect of the mesh on the particle-wall impact statistics. Indeed, in order to ensure grid-independent impact statistics, the results obtained with Grid 4 in Table 4.4 have been reported in the Appendix B. Comparing the results obtained for Grid 4 and Grid 5 in Table 4.4, it is possible to see that the results are very similar so that the particle-wall impacts statistics are very similar for Grids 4 and 5, further confirming the adequacy of Grid 5.

The sensitivity analysis was then continued by assessing the influence of the number of tracked parcels and of the subdivisions of the wall boundary on the particle-wall impact statistics.

Effect of the number of tracked particles

Firstly, a sensitivity analysis with respect to the number of particles tracked was carried out, dividing the curved wall into 20 sections each one of length $\Delta s = 0.0121$.

In particular, the number of particles were equal to 10000, 20000, 50000 and 75000. The comparison for a particle number of 20000, 50000, 75000 is reported below.

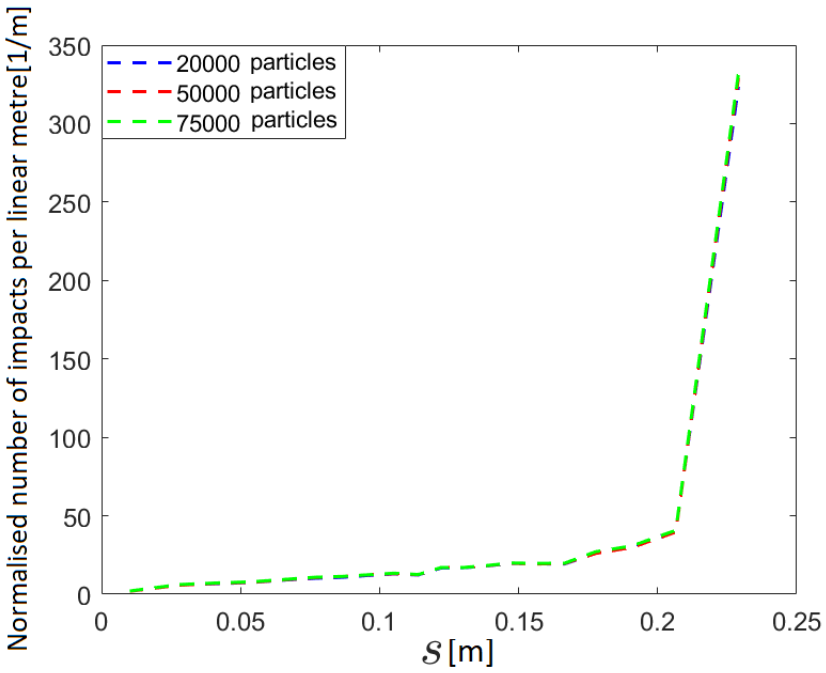

Figure 4.20: Comparison of the number of impacts per linear metre normalised to the number of particles and the Δs for different numbers of tracked parcel.

Figure 4.20 shows the results of the comparison in terms of number of impacts in each of the 20 wall segments divided by the length of the segment Δs and divided by the total number of tracked particles. Figures 4.21 and 4.22 are the analogous of Fig. 4.20 for the impact velocity and the impact angle, which are plotted as the locally mean values with their respective variances.

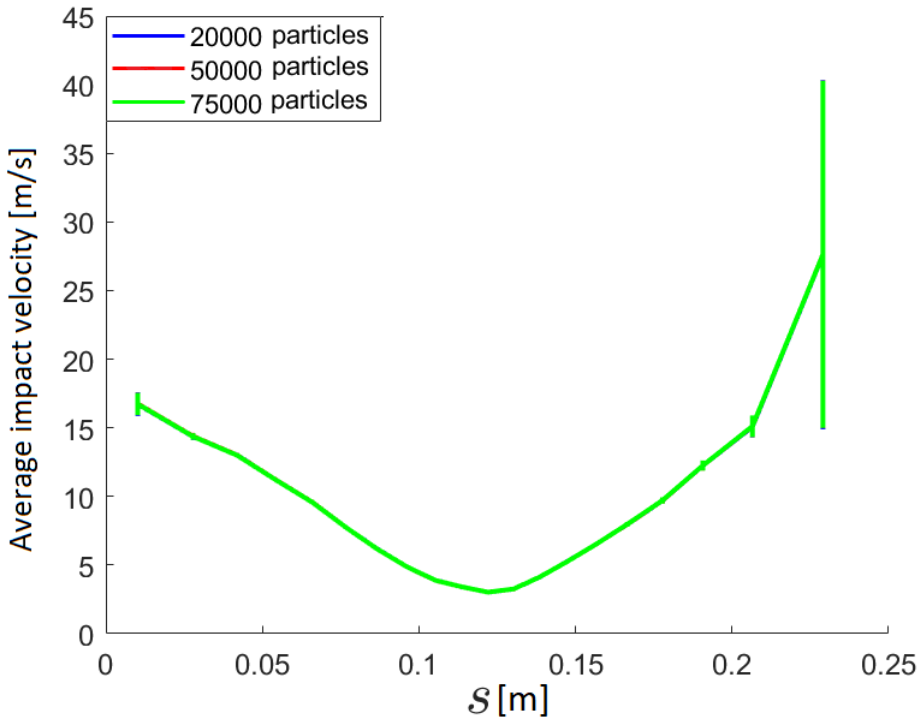

Figure 4.21: Behaviour of the mean modulus of impact velocity along the target wall for different numbers of tracked parcel.

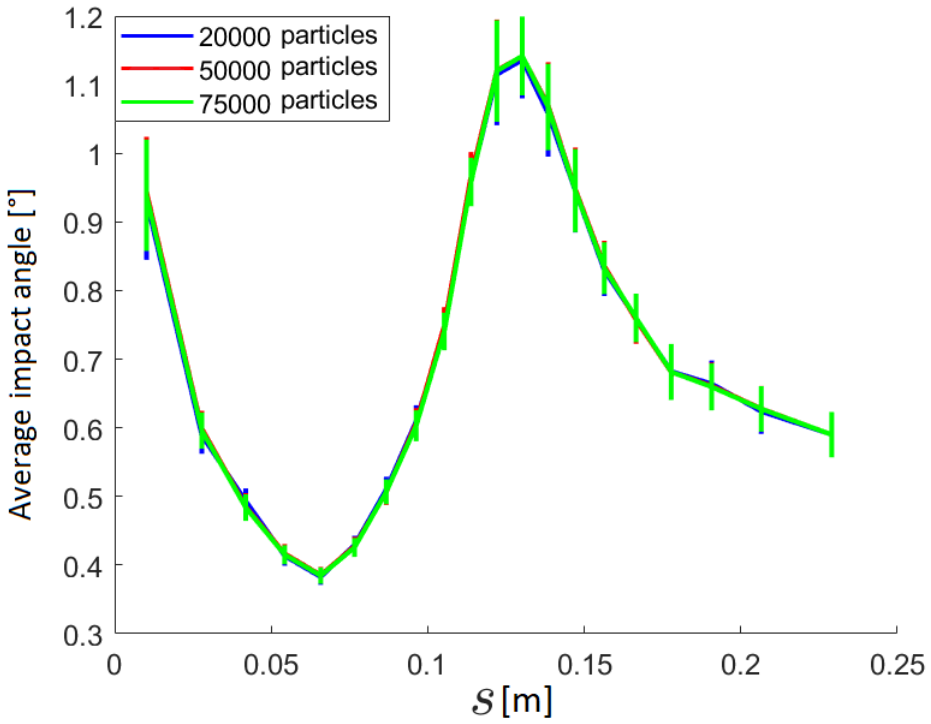

Figure 4.22: Behaviour of the mean impact angle along the target wall.

Comparing the three curves now in relation to the number of particles, it can be seen that they are almost coincident in terms of both mean values and variances. It is recalled that here the turbulent dispersion is not activated and, therefore, the trajectories have no random component. Consequently, the results are not at all surprising: the impact velocities and angles in each Δs will be reasonably very similar. Consequently, a particle number of 50000 was taken into consideration for the subsequent analysis, as it produced significant impact statistics.

Effect of the subdivision of the target wall

Then, the effect of changing the number of subdivisions of the target wall (or their length Δs) for a constant number of tracked particles, i.e. 50000, was investigated. The value of Δs value influences the statistics in two different ways. If Δs is small, the analysis will be more detailed, whereas if it is larger, the number of impacts in each Δs is higher, so that statistics are more significant.

In particular, the following subdivisions were considered:

Number of subdivisions	Δs
10	0.0243
20	0.0121
30	0.0081

Table 4.4: Number of subdivisions with the corresponding Δs.

A comparison of the statistics obtained in the three cases is reported, analysing the number of impacts per linear metre obtained for 50000 particles tracked, the average impact velocity and the average impact angle.

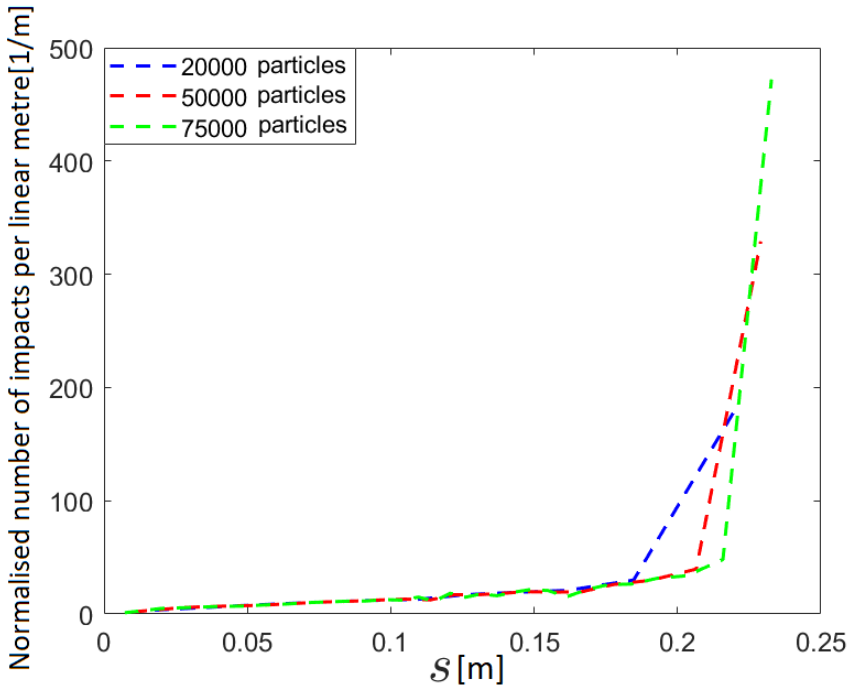

Figure 4.23: Comparison of the number of impacts per linear metre normalised to the number of particles and the Δs for different numbers of tracked parcel.

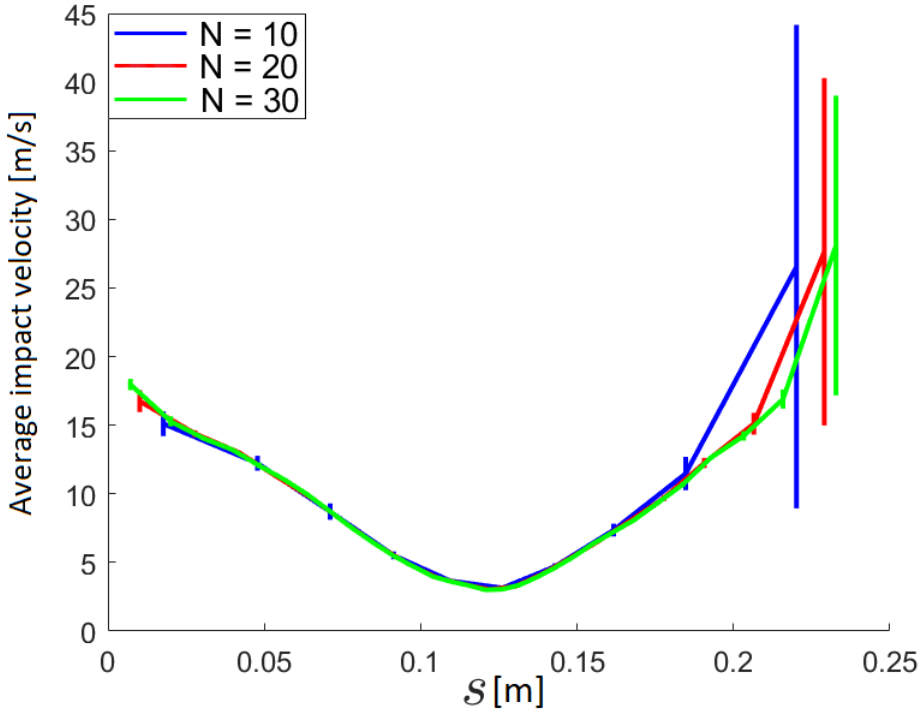

Figure 4.24: Behaviour of the mean modulus of impact velocity along the target wall for different numbers of tracked parcel.

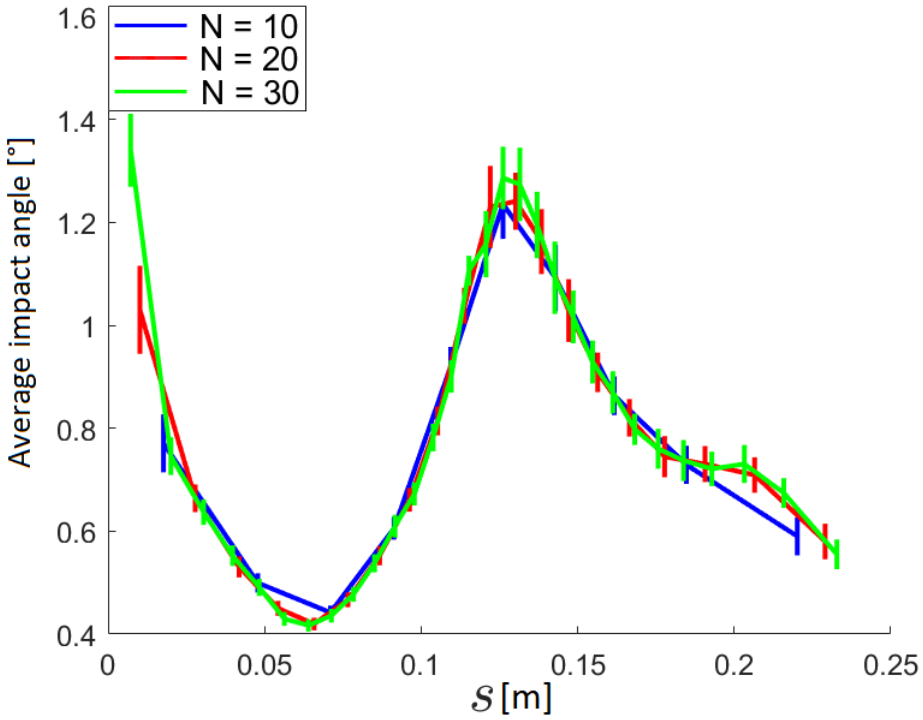

Figure 4.25: Behaviour of the mean impact angle along the target wall for different numbers of tracked parcel.

What can be seen is that by refining Δs in the three Figures 4.23 4.24 4.25 , the curves come closer together. In particular, the trend is very similar with 20 and 30 divisions. In these, for velocity and angle, the average trends are almost the same. The variance in the final region varies as it is the one characterised by the greatest number of impacts. Thus, the statistics can be considered significant for N greater than 20.

4.3.4. Conclusion

At the end of this chapter, conclusions can be drawn about particle tracking in the two-dimensional case.

1. The particles deflect carried by the jet and impact mainly near the blade outlet (Fig. 4.17).
2. The maximum velocity is reached at the blade outlet, in accordance with the fact that the water velocity is maximum in this region (Fig. 4.18).
3. The impact angles along the blade are very low. This means that erosion does not occur so much by impact as by abrasion and sliding (Fig. 4.19).

4. Despite the residual dependence of k on the grid, impact statistics appear relatively stable.
5. Impact statistics are not particularly affected by the number of trajectories (remember that turbulent dispersion is not activated) (Figures 4.21, 4.22, 4.20)
6. It is appropriate to set a number of subdivisions equal to 20 or 30, which corresponds to a Δs equal to 0.0121 m and 0.0081 m.

5 | Case study 2: hydro-abrasive wear of a Pelton blade

The second test case consist in the numerical prediction of the hydro-abrasive wear occurring on the Pelton blade due to the presence of sediments in the water jet. Compared to the previous 2D case, two step are made towards the real engineering problem. Firstly, the blade has been modeled as a 3D object. Secondly, the estimation of the hydro-abrasive wear has been made starting from the particle-wall impact statistics. So the representation of the blade is more realistic and is developed in its complexity, because the flow is markedly 3D and thus is more complex. Then the calculation of particle-wall impact statistics in the 3D case makes it possible to calculate erosion, which was not possible in the 2D case. This is because, even in the 2D case, Fluent treats the particles as spherical (and therefore with 3D shape) and this makes DPM incompatible with the evaluation of erosion on 2D boundaries. At the same time, some of the simplifications made in the previous 2D case have been not overcome. Particularly, the rotation of the blade is still ignored. This is clearly a simplification of the real case but allows to reduce considerably the computational burden as it enables steady-state modelling.

Furthermore, it was possible to exploit some of the results obtained in the 2D case and presented in Chapter 4 to reduce the number of simulations. As it will be discussed, it could be reasonable expected that some modeling choices did not depend on whether the system is 2D or 3D.

The present Chapter is organized as follows: firstly is reported how the geometry has been constructed and all the parameters of the problem (Section 5.1). Then all the settings for the CFD simulation, showing the computational domain, the boundary conditions, and the computation of the particle wall impact with the verification of the physical consistency of the solution (Section 5.2). In the end it has been performed a convergence assessment study, considering the effect of the mesh on the particle wall impact statistics, the effect of the number of particles on the particle-wall impact statistics and the effect of the mesh on the erosion prediction (Section 5.4).

5.1. Blade geometry and testing conditions

In order to build the numerical set up, reference was made to a similar case study reported in the PhD thesis by Leguizamon [7].

The blade considered by Leguizamon is visible in a picture reported in his thesis, reported here in Figure 5.1. The geometric and flow parameters of Leguizamon's case are also reported in the thesis, and they are summarized in Table 5.1.

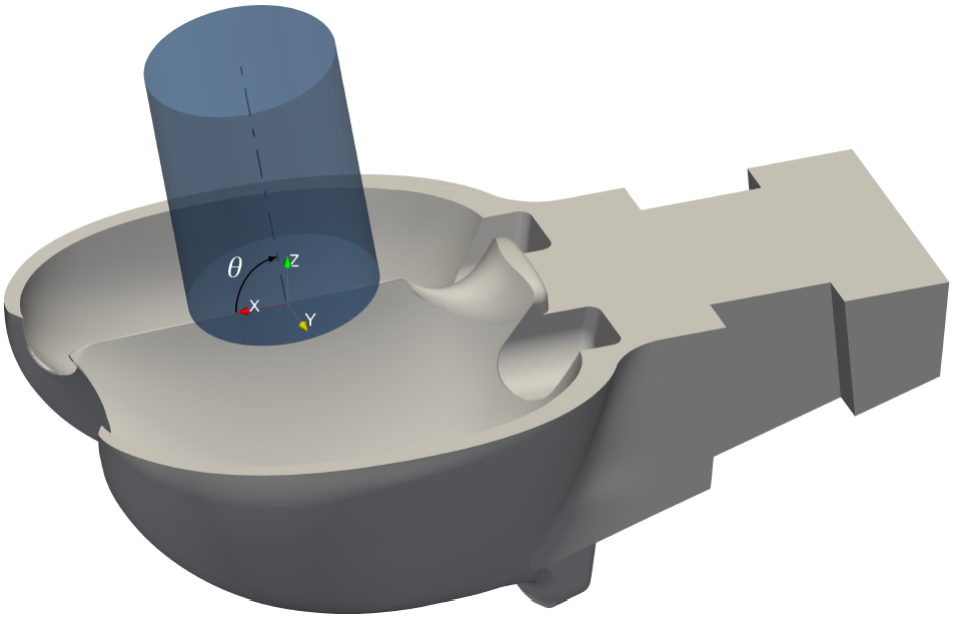

Figure 5.1: Picture from the PhD thesis of Leguizamon [7] representing the blade geometry in his case study.

Name	Parameter symbol	Value	Unit
Jet velocity	C_1	28.5	[m/s]
Jet Diameter	D_0	0.140	[m]
Jet length	L_j	0.201	[m]
Bucket width	B_2	0.375	[m]
Jet impingement angle	Θ	80	[°]
Sediment concentration	C	0.1%	[$\%_w$]
Particle diameter	d	0.0001	[m]
Particle density	ρ	2650	[kg/m^3]

Table 5.1: Geometric and flow conditions from the PhD thesis by Leguizamon [7]

The computational domain was obtained from a given geometry found in the web in association with the image 5.3. All the data of the problem are reported in Table 5.1 taking as reference value the one reported in the thesis of Leguizamon [7]. The basic idea was to reproduce the 3D case reported in the thesis of Leguizamon for which, however, no geometry was available. The geometry was found in Internet and corresponded to an entire impeller with all the blades as shown in Figure 5.2, which consequently had to be processed in Design Modeler. First, it was necessary to eliminate the impeller and all but one of the blades. Secondly, the geometry has been scaled in order to have the same bucket width of the geometry reported in Figure 5.1. In this way the geometry is as similar as possible to the domain considered by Leguizamon reported in Figure 5.1. As a result there is a good correspondence that however is not complete.

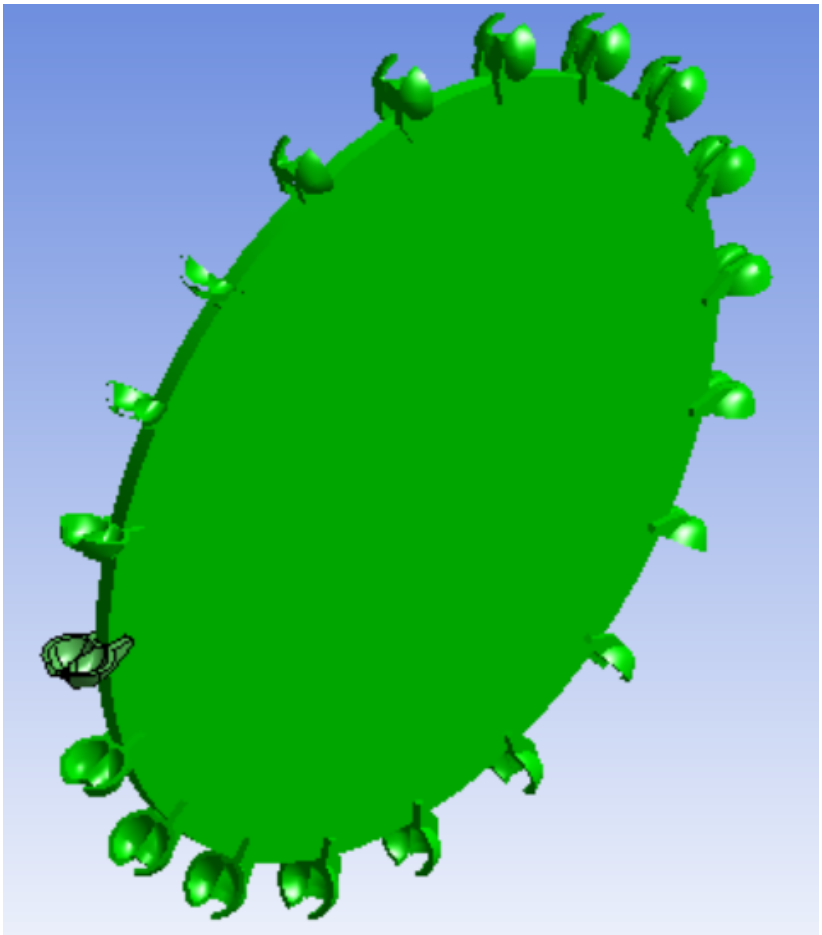

Figure 5.2: Impeller.

5.2. CFD set up

All the information needed to set up the numerical simulation are reported below. In particular, the fluid dynamic model, the computational domain, the boundary conditions, and the calculation methods for particle-wall impact statistics and hydro-abrasive wear will be given.

5.2.1. Fluid dynamic models and simulation strategy

As in the previous 2D case, the one-way coupling regime was assumed between the sediments and the free jet due to the low sediment concentration of 0.1% Thus, the free water jet in air was first simulated using the Volume of Fluid model. Afterwards, the calculation of the sediments trajectories was performed over the steady-state VOF solution, which was not changed. Finally, the wear of the blade was estimated from the particle-wall impact statistics using the erosion model by Det Norske Veritas [19].

In the simulation of the free water jet, RANS-based formulation of the VOF coupled with standard $k-\varepsilon$ turbulence model were used. A comparison of turbulence models was not performed, owing to the findings reported in Section 4.1.4 for the previous 2D case, which indicated that the choice of the turbulence model was not going to affect the velocity field, that is the principal variable for determining impact statistics. The effect of the surface tension between water and air was neglected, and the water-air interface was modeled as sharp. This was made, once again, by exploiting the results of the sensitivity analysis performed for the 2D case and reported in Section 4.2.4. In fact, it was expected that, since the physical phenomenon is the same, the change from two-dimensional to three-dimensional does not affect these modelling settings. In fact, from a physical point of view, the choice of modelling sharp interface depended on the fact that we are considering two fluids that do not mix to form bubbles, but remain separated by a rigid interface with little mixing, and that the surface tension between water and air is negligible for the high speeds that characterize the water jets of Pelton turbines.

Like in the previous case, the tracking of the particle trajectories is performed in steady-state mode, so that the computational cost is reduced. The solved Lagrangian equation of motion is 3.3 considering pressure gradient force, spherical particles and particle turbulent dispersion. Unlike the previous case, the particles were to be spherical because the results provided by non-spherical particles implied an extremely low number of impacts. The pressure gradient was considered in the same way as in the previous case, and in this case the particle turbulent dispersion was activated to generate more meaningful impact

statistics.

The procedures for evaluating the particle-wall impact statistics and the abrasive wear from the output of the DPM calculations are described later in Section 5.2.3.

5.2.2. Computational domain, boundary conditions, computational mesh, and other solution settings

The representation of the blade and of the cylinder of inlet of the case under analysis is reported in Figure 5.3. Note that this is not the computational domain since here are shown both the solid part of the blade and the fluid part of the water that is injected into the system. Indeed, the computational domain was created as a complement to the solid part as shown in Figure 5.4 Finally, the boundary conditions (Fig, 5.5) applied to the computational domain were an inlet condition (blue boundary) with velocity $C_1 = 28.5$ m/s and turbulent kinetic energy and length scale, that were the same of the 2D case, namely, turbulent kinetic energy of 3.25 % and turbulent length scale of $0.03D_0$. At the outlet (red boundary) was set a relative pressure of zero and at the wall (grey boundary) a no-slip boundary condition.

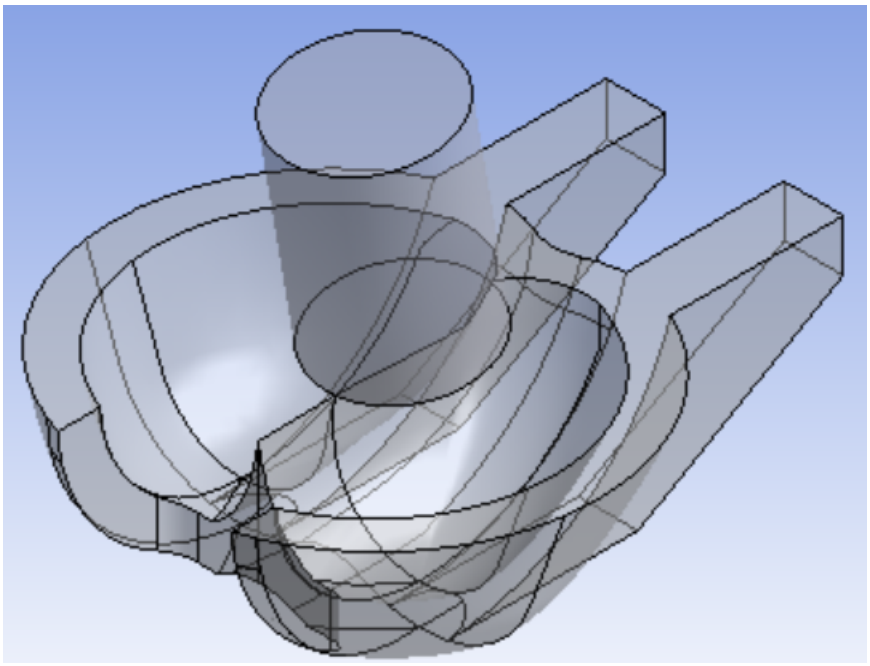

Figure 5.3: Blade with the cylinder of the injection of water.

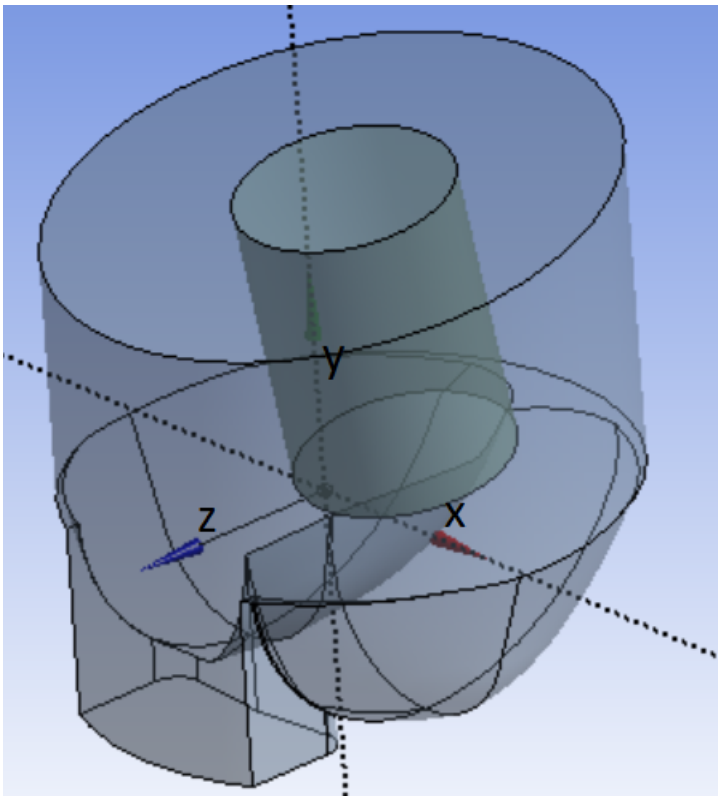

Figure 5.4: Computational domain of the 3D Pelton blade.

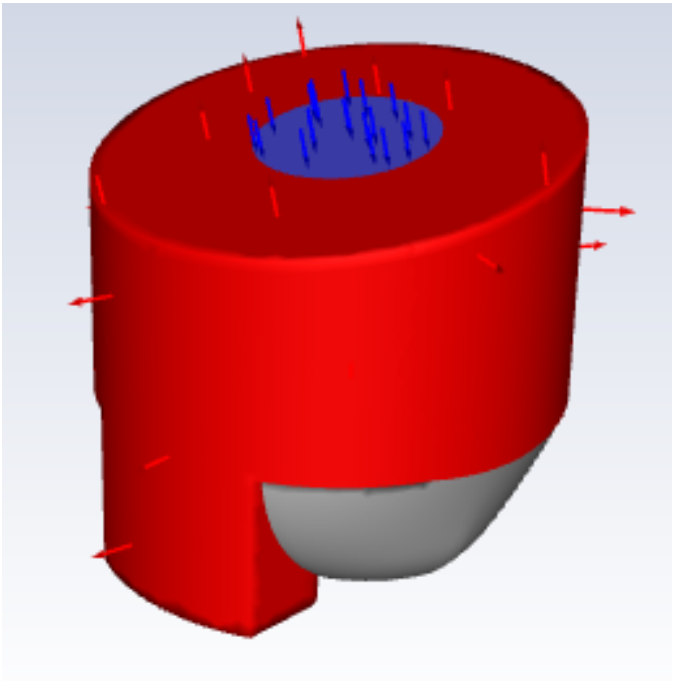

Figure 5.5: Boundary conditions of the 3D domain: the blue boundary corresponds to the inlet, the red boundary to the outlet, the grey boundary to the wall.

The fluid domain was then discretized using a tetrahedral grid, without an inflation layer.

The numerical settings in this 3D case are the same as in the 2D case with regard to the fluid dynamic solver as reported in Section 4.2.1. When it comes to the DPM settings these turn out to be the same except for the fact that spherical particles were considered in this case.

5.2.3. Calculation of the particle-wall impact statistics and of the hydro-abrasive wear

The following procedure was carried out to calculate the impact statistics. First, a boundary mesh of the blade was created (Fig. 5.6).

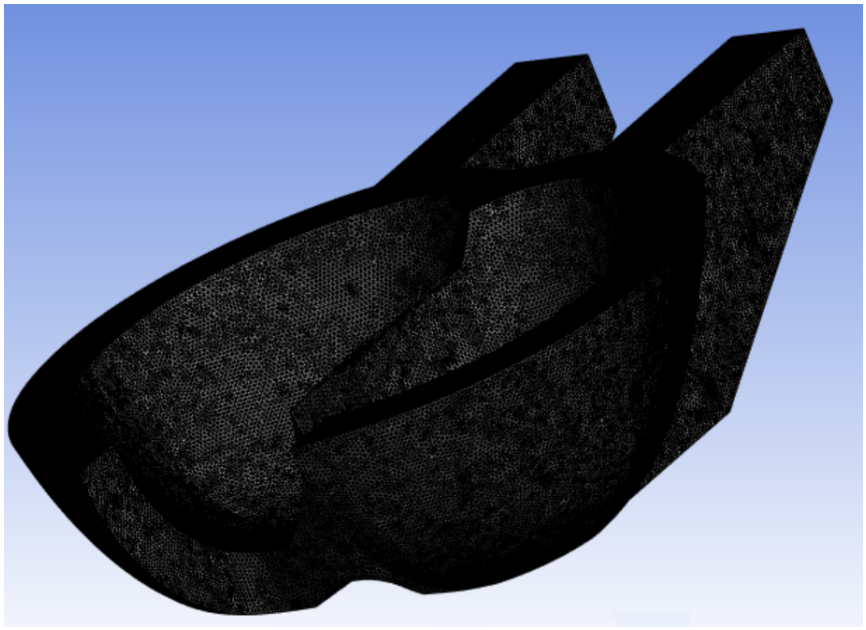

Figure 5.6: Boundary mesh.

Next, .dpm files containing the positions and velocities of the impacts of all particles, obtained as a result of injecting the particles into the fluid, were generated by Fluent. Next, the boundary mesh was imported and the coordinates of all blade cell centroids and relative area were calculated. At this point the .dpm file is read into Matlab, saving all the impact parameters. From the impact coordinates $(x_{imp}, y_{imp}, z_{imp})$, it is then calculated which centroid of the boundary mesh they are closest to, and each impact is then asscociated to the corresponding centroid. Impact velocity and impact angle are then calculated and associated with the corresponding centroid. In this way each centroid is associated with all the velocity values of the impacts occurring closest to it as well as

for the angles. In this way, by averaging these values, impact velocity and impact angle are calculated, as well as the number of impacts on each cell. Erosion on each cell is then calculated through the DNV model explained in 3.4). Finally, the calculated values are represented graphically by plotting the corresponding average value on each cell.

5.3. Physical consistency of the numerical solution

Like in the previous chapter an analysis of the physical consistency of the solution have to be performed. The physical consistency of the VOF solution was performed by inspecting the velocity magnitude and volume fraction fields over the xy and yz planes in Fig. 5.4 The results are shown in Figure 5.7, and they refer to Grid 2 in the following Table 5.2.

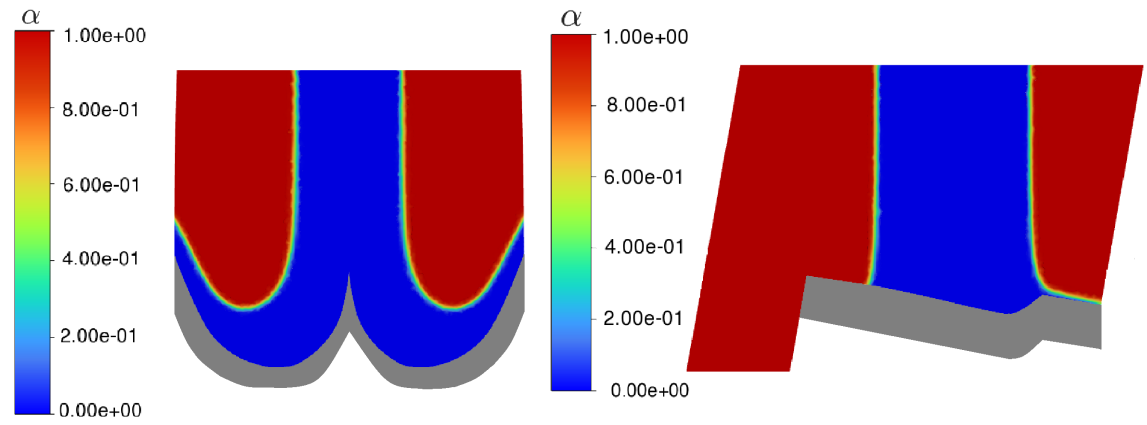

(a) Volume fraction in the xy plane (α).

(b) Volume fraction in the yz plane (α).

(c) Velocity magnitude in the xy plane (v).

(d) [Velocity magnitude in the yz plane (v).

Figure 5.7: 3D: Physical consistency VOF

The volume fraction of air, represented in Figures 5.7a and 5.7b, allows clear identification of the behavior of the water jet. Not surprisingly, the jet comes down from the inlet and

then is deflected laterally, finally leaving the blade. The field of the velocity magnitude, see from pictures 5.7c and 5.7d, is fully coherent with the physical phenomenon. The velocity is about 28.5 m/s near the inlet (as it is the value imposed), is zero near the wall and then increases rapidly in the boundary layer.

Now it is possible to compare these results with the one of the 2D case. First of all comparing Figure 5.7a and Figure 4.10b it is possible to see that the volume fraction is similar in the two cases, even considering that the two problems have different parameters. Then, comparing Figure 5.7c and Figure 4.10a, it can be seen that qualitatively the two solutions are similar, in fact, the velocity turns out to be zero at the wall, and increases rapidly moving away from it. Notably, the velocity increases again at the exit in both cases.

Color plots of the turbulent kinetic energy are not shown, since this variable turned out to be rather grid-dependent. This assumption was made on the basis of the results obtained in the two-dimensional case. However, it will be shown that the particle-wall impact statistics are substantially independent of the grid, which suggests that the effect of the mesh on k does not affect the wear estimates.

Finally, it is interesting to show the trajectories of the particles. An example is shown in Figure 2.4. Here it can be seen that the trajectories of the particles follow the motion of the fluid, that is, they descend downward and then deviate laterally.

In Figure 5.8 are reported the impact velocity angle and number of impacts for Grid 2 considering 300000 particles injected into the system.

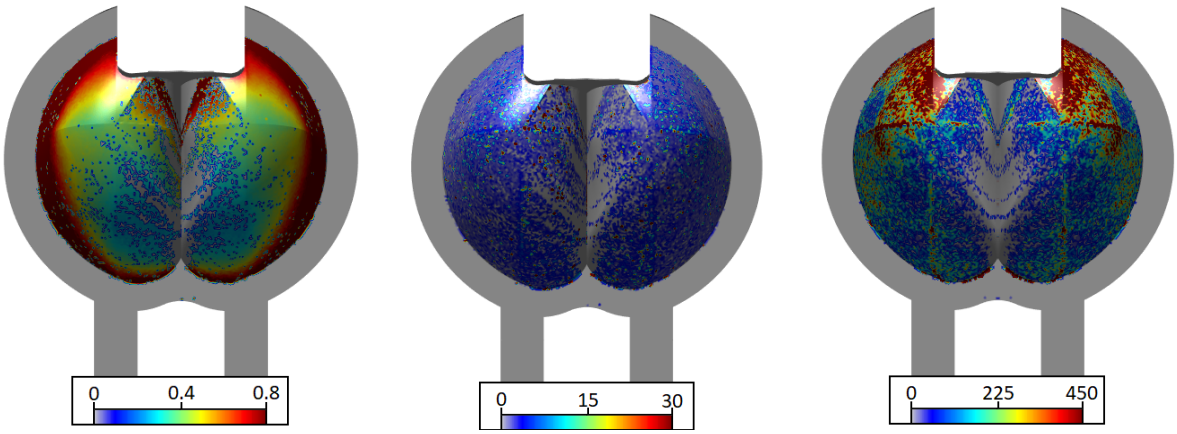

(a) Impact velocity normalized w.r.t the impact velocity.

(b) Impact angle.

(c) Number of impact per cell.

Figure 5.8: Parameters for studying grid independence with Grid 2.

As can be seen from Figure 5.8a (here is reported the impact velocity normalized with respect to the inlet velocity of 28.5 m/s), is possible to see that the impact velocity follows the fluid behaviour, in particular it increases near the outlet. The angle of impact in Figure 5.8b ranges between 0 and 30 degrees assuming mainly low values. Finally, the number of impacts in Figures 5.8c, are higher near the outlet and lower in the internal region of the blade. This comparison with particle trajectories 2.4, is consistent because particle trajectories hit the blade many times near the exit, and little in the inner region, namely near the splitter and on the bottom of the blade.

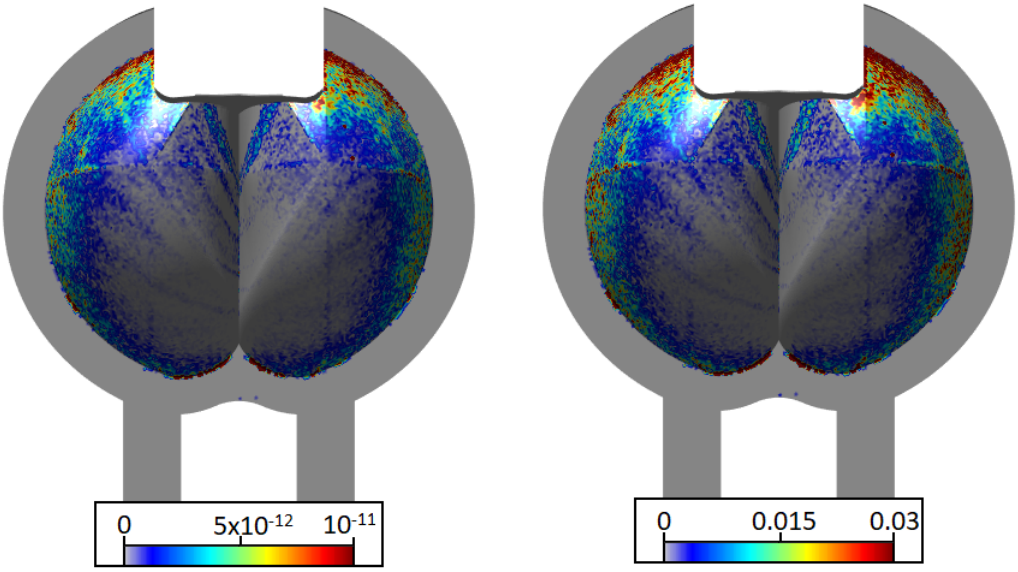

(a) Erosion rate. (b) Penetration rate.

Figure 5.9: Erosion rate and penetration rate, computed with 300000 particles with Grid 2.

Next, erosion rate and penetration rate were considered, again for the configuration with Grid 2 and 300000 particles injected as shown in Figure 5.9. They were computed accordingly with the DNV model presented in Section 3.4. In particular, the regions where the erosion ratio is higher (Fig. 5.9a) correspond to those where the number of impacts and the velocity (Fig. 5.8a and Fig. 5.8b) are higher, which is consistent with the erosion process. As a result, the penetration rate is also higher in that region (Fig. 5.9b). Specifically, there is correspondence between the most eroded zones and the zones where both the impact velocity is higher and the number of impacts is higher. However, the DNV model is not the most appropriate for predicting erosion because it was developed for impact erosion (at relatively high angles) while the calculated angles are extremely low and show an abrasion-erosion type of erosion.

5.4. Convergence assessment study

The solver considered in this case was the same as in the two-phase case with the same options. The main difference in this case was the number of iterations required for convergence. In fact, a larger number of iterations was required in this case, amounting to 10000 for the first two Grids and 20000 for the third Grid. In particular, for Grids 1 and 3 the value on the moment of 0.2 was put in the "Controls" section while the other options were the default ones. Thus, in general, the number of iterations required compared with the 2D case was greater.

The convergence assessment study was made by considering the particle-wall impact statistics and the erosion-related parameters as target variables, as these are the essential information for the purpose of the modelling framework. The effect of computational mesh and number of tracked particles was considered, as explained in the following subsections. There would be a third parameter to consider, which is the resolution of the boundary mesh, but it was not considered due to time constraints.

5.4.1. Effect of the mesh on the particle-wall impact statistics

Three different meshes were created. Keeping the same mesh structure already explained and shown in Section 5.2.2, the degree of thickening and thus the number of cells was changed. The number of elements of each computational grid are reported in Table 5.2. As a side note, it is remarked that significant challenges arose from the design of the mesh in the 3D case. Particularly, the curved surface of the blade created issues in the generation of tetrahedra with consequent problems in the convergence of the solver. In fact, due to the semi-elliptical shape of the blade, the geometry is characterised by areas with changes in curvature, which implies a demand for grid refinement that leads to the creation of cells that are very small.

Mesh	**Number of Elements**
Grid 1	717407
Grid 2	1573102
Grid 3	2166186

Table 5.2: Number of cells in each computational grid.

The Grid that represents Grid 2 is reported in Figure 5.10. In particular it has been considered three different regions (as represented in Figure 5.10) in order to refine the

mesh only where it was really necessary. Region 1 and Region 2 that are the one near the inlet and near the wall, are the most refined considering the same cell size. This procedure was maintained for all the Grids.

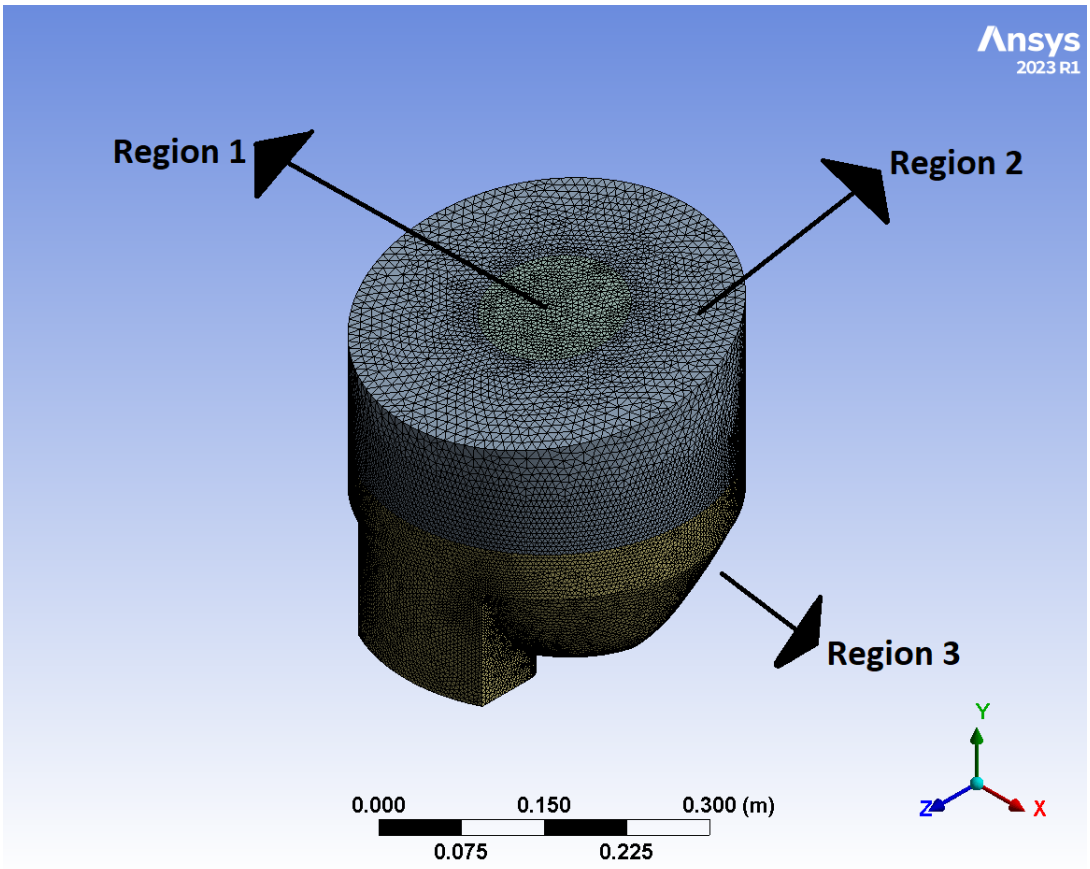

Figure 5.10: Grid 2.

To compare the three Grids, the average impact velocities and impact angle on the cells and the number of impacts per cell were then considered. In this case, the impact statistics were calculated based on the injection of 300000 particles. The boundary mesh considered for all the three cases was the same ad is the one reported in Figure 5.6.

Graphic representations of the particle-wall impact statistics for Grid 1, Grid 2, and Grid 3 is given in Figs. 5.11, 5.8, and 5.12, respectively. Only a qualitative comparison could be made from these pictures and, at first glace, the results appear reasonably similar. The distributions of impact velocities normalized with respect to the inlet velocity (Figs. 5.11a, 5.8a, 5.12a), impact angles (Figs. 5.11b, 5.8b, 5.12b) and number of impacts (Figs. 5.11c, 5.8c, 5.12c) are coherent, as well as the position of the maxima, which are of the same order of magnitude. As result, the grid that has been chosen was Grid 2, because it produced a grid-independent solution without any excess in mesh resolution.

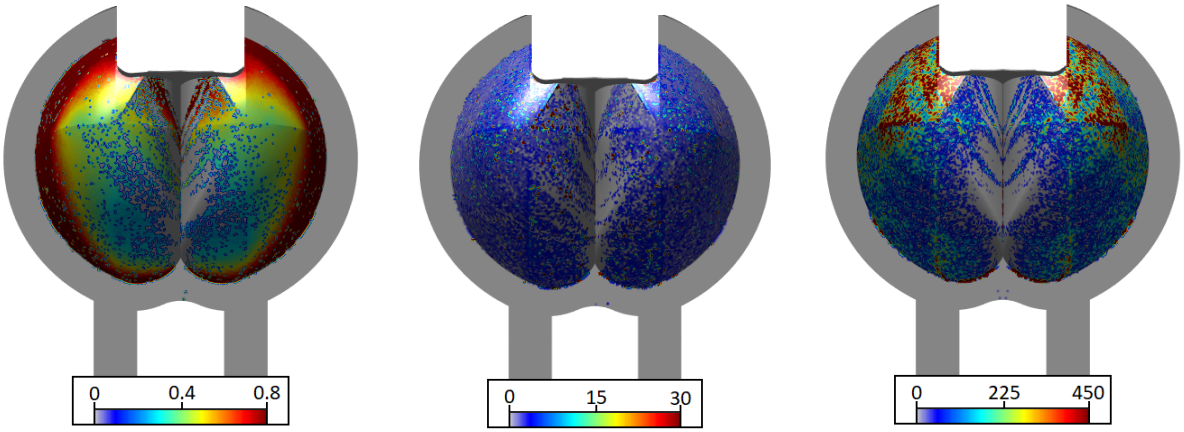

(a) [Impact velocity normalized w.r.t the impact velocity.

(b) Impact angle.

(c) Number of impact per cell.

Figure 5.11: Parameters for studying grid independence with Grid 1.

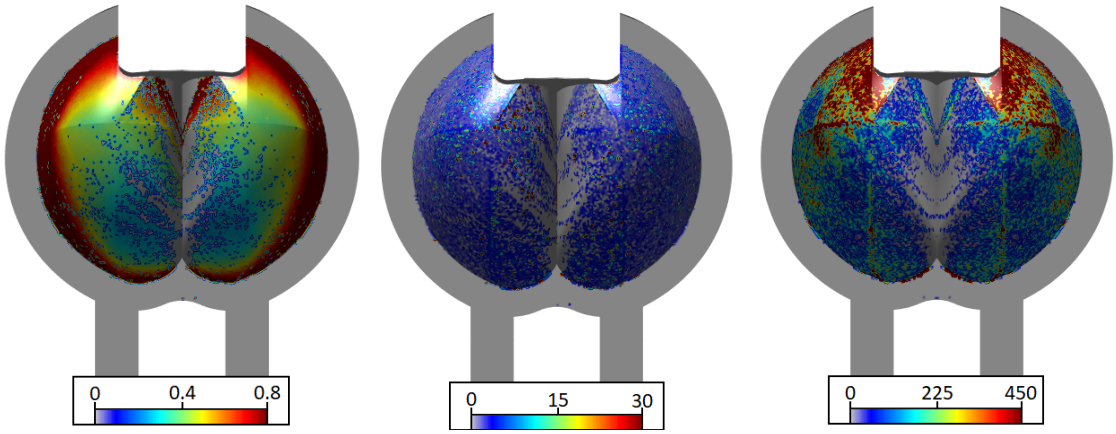

(a) Impact velocity normalized w.r.t the impact velocity.

(b) Impact angle.

(c) Number of impact per cell.

Figure 5.12: Parameters for studying grid independence with Grid 3.

5.4.2. Effect of the number of particles on the particle-wall impact statistics

To perform steady particle tracking, a number of particles of 100000, 200000, 300000, was considered for each computational grid. The impact velocity, angle, and number of impacts for each cell were considered as target parameters. The results with 300000 particles are reported in Section 5.4. The comparison has been performed using the following options in the injections: pressure gradient force, spherical particles and turbulent

dissipation rate. Here are reported the results for Grid 2 (Table 5.2), while the one for Grid 1 and Grid 3 can be found in Appendix B. It is recalled that particle turbulent dispersion is active in this case and therefore the trajectories have a random component, so the analysis of the effect of the number of trajectories is more significant than in the 2D case where particle turbulent dispersion was not activated.

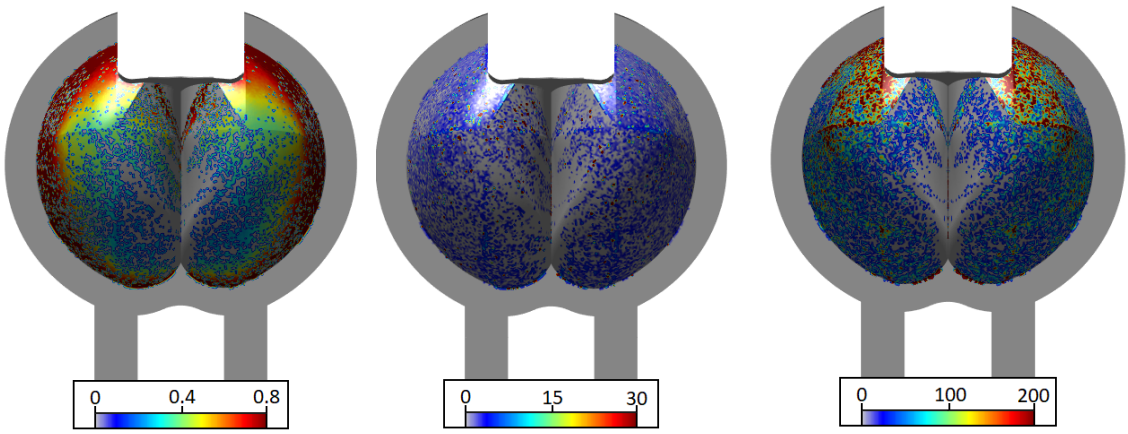

(a) Impact velocity normalized w.r.t the impact velocity

(b) Impact angle.

(c) Number of impact per cell.

Figure 5.13: Impact statistics obtained with Grid 2 and 100000 particles.

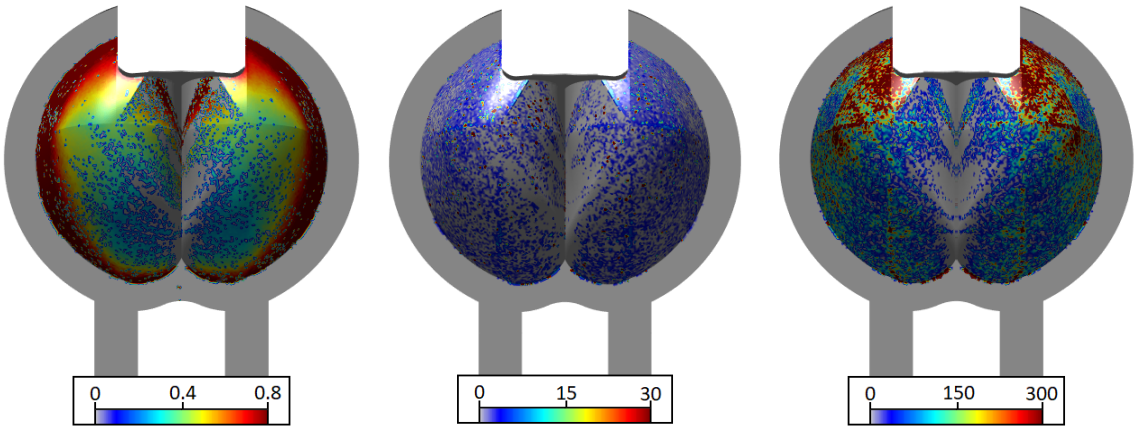

(a) Impact velocity normalized w.r.t the impact velocity.

(b) Impact angle.

(c) Number of impact per cell.

Figure 5.14: Impact statistics obtained with Grid 2 and 200000 particles.

As can be seen in Figures 5.13 and 5.14 for both velocity and angle of impact and number of impacts, the behavior is the same with different numbers of particles and also for all the different Grids. So comparing the impact velocity normalized with respect to the inlet

velocity (28.5 m/s) in Figures 5.13a, 5.14a and 5.8a is possible to see that also it ranges between 0 to 0.8 and assumes its maximum values near the outlet, and approaches to zero in the internal region of the blade.

Comparing then the angles of impact in figures 5.13b, 5.14b and 5.8b, it can be seen that in this case the angles take predominantly low values throughout the blade, ranging between 0 and 30.

In particular, comparing Figures 5.13c, 5.14c and 5.8c, it can be seen that as the number of particles increases, the number impacts increases consequently. In any case, the most affected areas remain the same, showing the same pattern but assuming different values.

5.4.3. Effect of the mesh on the erosion predictions

Finally, after setting the number of particles at 300000 a comparison was made on the erosion prediction with the three different Grids 5.2.

In Figures 5.15, 5.9, 5.16 are reported the graphs of the eroded mass with the penetration rate for Grid 1, Grid 2 and Grid 3 respectively, using the DNV model as explained in Section 3.4.

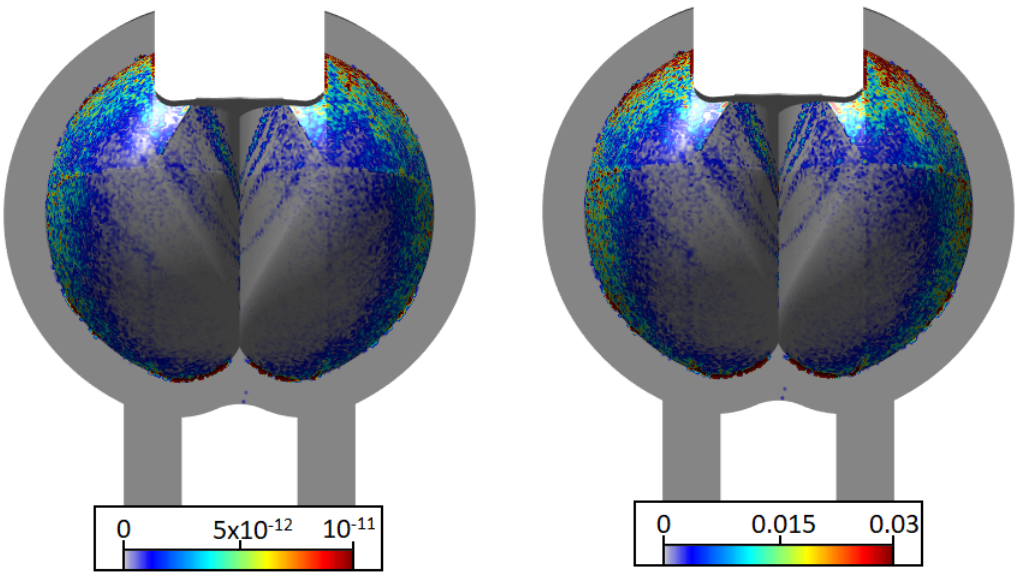

(a) Erosion rate. (b) Penetration rate.

Figure 5.15: Erosion rate and penetration rate, computed with 300000 particles with Grid 1.

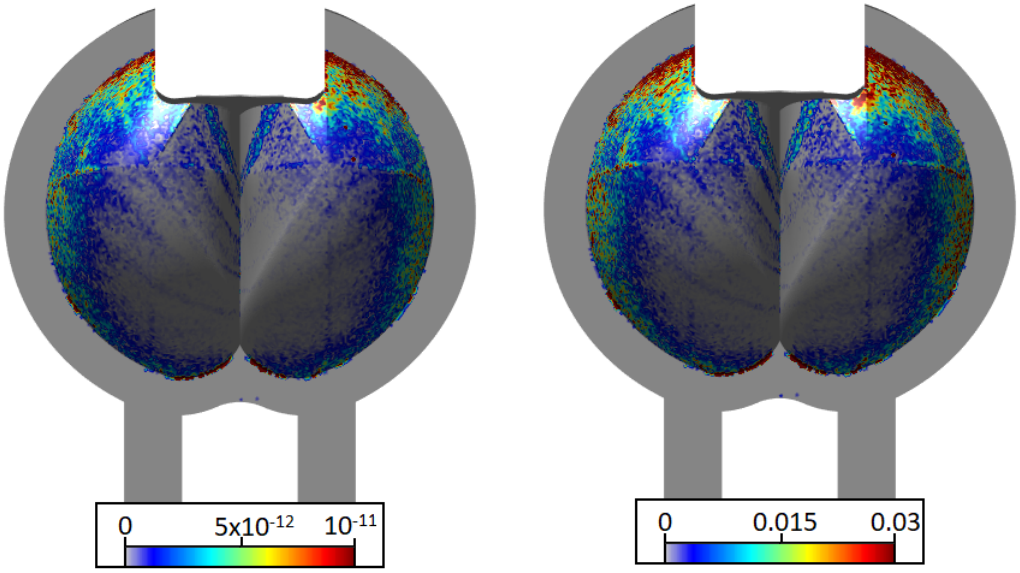

(a) Erosion rate. (b) Penetration rate.

Figure 5.16: Erosion rate and penetration rate, computed with 300000 particles with Grid 3.

In particular comparing the Figures 5.15, 5.9 and 5.16 is possible to see that both the erosion and the penetration rate are predicted in the same way in the three different Grids. Specifically, the erosion rate for all the Grids is higher near the outlet where both the impact velocity and the number of impact is higher (Figs. 5.9a, 5.15a, 5.16a). The erosion rate is indeed highest near the blade outlet and practically nonexistent at the bottom of the blade and near the splitter. The erosion pattern also turns out to be the same for the three Grids, even taking values that assume the same order of magnitude. Correspondingly, the penetration rate results to be higher in the same region (Figs. 5.9b, 5.15b, 5.16b). In conclusion, it is possible to say that the chosen grid has no effect on erosion prediction.

It is intended to remark that the chosen erosion model, i.e., DNV, will go to predict the erosion pattern, however, having possible shortcomings from the point of view of the assumed numerical values, as already explained in Section 3.4.

5.4.4. Comparison against literature results

The comparison was made referring to some pictures reported in the PhD thesis of Leguizamon [7]. As already mentioned, the parameters of the case study of Leguizamon are the same of those considered here except for the shape of the blade, which has

the same width but slightly different geometry. Thus, a quantitative comparison was not possible.

Figure 5.17 could be used to partially validate the predicted water velocity magnitude. Note that the jet velocity at the nozzle outlet is the same in the study of Leguizamon and the present simulation, equal to 28.5 m/s. The velocity values near the bucket outlet are about 24 m/s in the case in analysis (Figures 5.7d and 5.7c) and about 27.5 m/s in the case of Leguizamon (Figure 5.17).

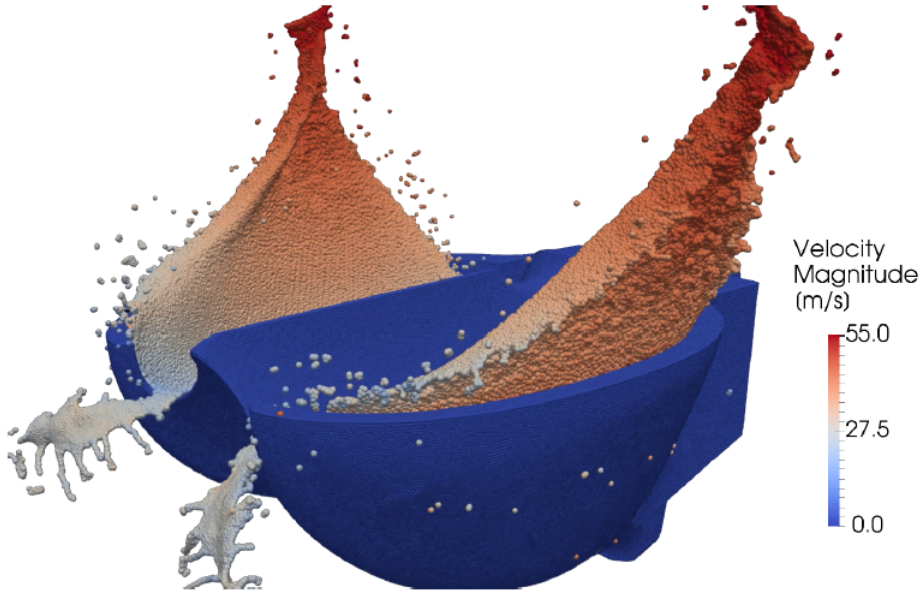

Figure 5.17: Water jet hitting the bucket colored by the velocity magnitude, as reported in Leguizamon [7].

Another comparison can be performed through the impact statistics, considering Figs. 5.11 5.8 with respect to Fig. 5.18 from [7]. In both simulations, the impact velocity assumes the highest values near the exit from the bucket, i.e. around 30 m/s (this value is provided in the output of Matlab, and can be inferred by Figure 5.18, since the maximum value of velocity normalized with respect to the inlet velocity is equal to 0.8), whereas it is relatively low in the central area of the blade. Also, looking at the Leguizamon figure shows a second (lower) peak near the splitter, which is not detected in the simulations. This could be due to differences in fluid dynamics models, but also to differences in blade geometry or boundary mesh construction, since the Leguizamon one is not known. On the other hand, the impact angle turns out to have values ranging approximately from zero to 30 degrees assuming mostly low values along the entire domain (Fig. 5.17). Conversely, as it can be seen in Fig. 5.8a, the present simulation does not indicate any impingement

occurring over the splitter (thus, no impact angle is calculated there) and, in the outer part of the bucket, the impact angles seem lower than those predicted by Leguizamon [7].

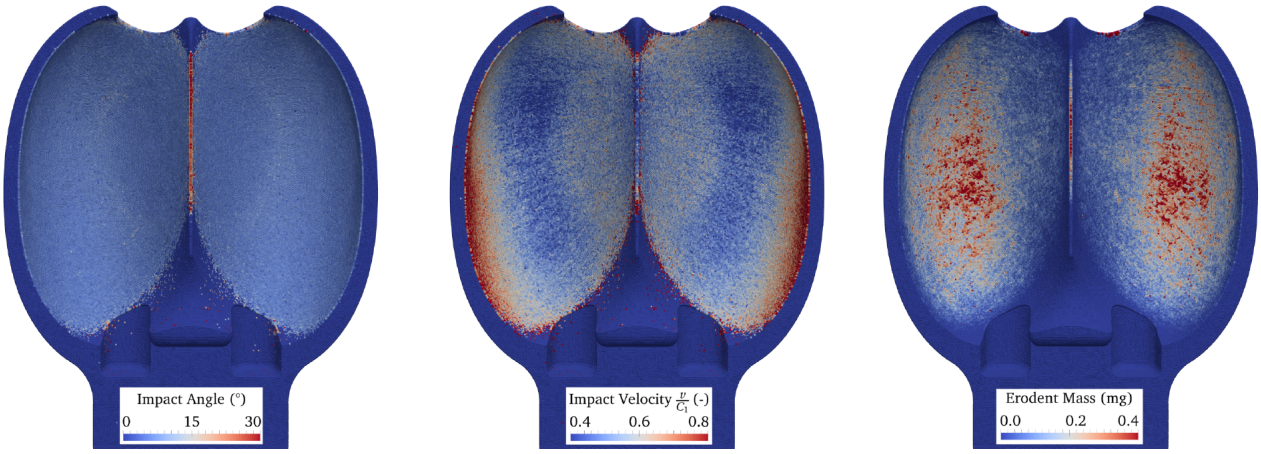

Figure 5.18: Particle-wall impact angles and dimensionless particle-wall impact velocities over the surface of the blade, as reported in Leguizamon [7].

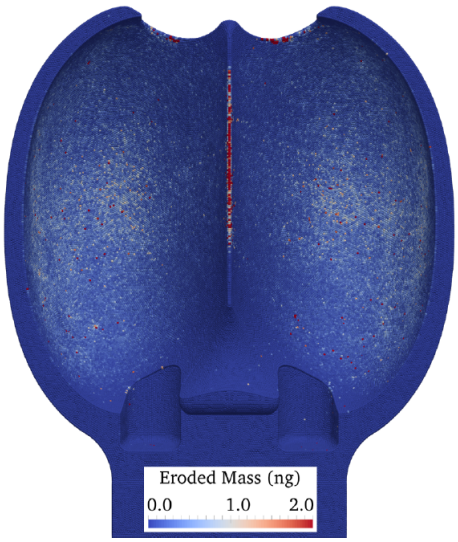

Figure 5.19: Eroded mass over each surface element, as reported Leguizamon [7].

Finally, Figure 5.19 can be used to compare the erosion estimates previously reported in Fig. 5.9a. Actually, Leguizamon [7] reported the eroded mass from each surface cell at the end of the physical time simulated, which was equal to 3,180 hours. Conversely, the variable produced as output of the present simulation is the eroded mass flow rate. As for the erodent mass and the number of impacts in every surface cells, also the eroded mass distribution obtained by Leguizamon cannot be directly compared with the erosion rate distribution reported in Fig. 5.9a since the two boundary meshes are different (specifically

the one of Leguizamon is not known), as well as the erosion model and the geometry of the blade. However, a qualitative comparison between the two plots could be reasonably made. It could be observed that the erosion pattern predicted by Sebastian fairly follows that of the erodent mass, that is, the number of impacts. Since there are differences between Sebastian's impact distributions and those obtained, there will also be differences in the estimation of the erosion pattern. In fact, unlike the case of Leguizamon, in the simulations under analysis much erosion is predicted at the top of the blade, and no erosion is predicted at the splitter. Moreover despite of the simulations performed, Leguizamon predicts some erosion over the bottom of the blade. However, there are also similarities, in fact in both cases little erosion is estimated in the central part of the blade (although Sebastian notes erosion of the splitter despite the results obtained) and some erosion in the outer part of the blade itself.

In summary, there are differences between the results obtained and those of Leguizamon, which could be due to the different fluid dynamic model, but also to the different blade configuration (for instance the bucked width is the same but nothing is known about the depth of the blade) and the erosion model. However, there are also similarities, especially in relation to the distributions of impact velocities (and, to a lesser extent, also angles). This indicates that, given all the limitations of the case and the available data, there are positive elements in the comparison.

5.5. Conclusion

The following considerations could be made about the findings of the present case study.

1. The solution is consistent with the underlying physical processes (Figure 5.7). In particular, the results obtained on the cross section appear to be consistent with the results obtained in the 2D case.

2. The particle-wall impact statistics are coherent with the fluid dynamic solutions. As it can be seen in Figs. 5.8a and 5.8b. It is remarked that the impact angles are low.

3. The erosion pattern can be explained from the particle-wall impact statistics considering the functional dependencies of the DNV erosion model (Eq. 3.4). In particular, the erosion map is consistent with impact statistics, and the DNV model is consistent in terms of location and severity of erosion.

4. The particle-wall impact statistics and the erosion pattern were found to be substantially independent from the mesh (considering Grid 1 to Grid 3 in Table 5.2) and

from the number of calculated trajectories (which was varied between 100000 and 300000). However, this conclusion was argued only based on the visual inspection of color maps, without performing a more quantitative comparison.

5. The model showed similarities and differences from the numerical results reported in the Phd thesis of Leguizamon [7]. In Particularly, there are similarities in the values and the pattern assumed by the impact velocities, while for the impact angle there is only a similarity in the pattern but not in the numerical values, which turn out to be lower. Comparing also the erodent mass with the number of impacts, these are found to be comparable, thus showing that in both cases the particles impact more in the same regions. However, there are also differences in that neither impact velocity nor erosion is predicted near the splitter. This could be due to differences in the modeling choices made. Indeed, is shall be noted that a direct comparison between the two sets of data is not possible due to the differences in the geometry, in the erosion model, and in other key numerical settings such as the discretization of the surface of the blade.

6 | Concluding remarks and future developments

The development of this thesis focused on the preliminary development of a CFD framework for simulating the hydro-abrasive wear of Pelton turbine working in a sediment-laden environment. The final goal is to produce a tool useful for the optimized design and management of hydro-power systems. A step-by-step analysis was conducted, starting from the simplest model and adding a new element of complexity at a time. In this perspectives, different test cases have been considered in the development of the simulation model. Thus, it might be claimed that the broad objective of this thesis is to build a methodology for the engineering prediction of turbine wear, trying to find the best compromise between accuracy and computational cost.

The thesis was organized as follows. In Chapter 1, the problem of erosion in Pelton turbines was introduced underlining the need for further research on this topic. In Chapter 2, all the elements of complexity of the problem were analysed. In Chapter 3, the mathematical models employed in the work were introduced. Afterwards, two test cases were investigated. The first, described in Chapter 4, focuses on a 2D slice of the blade. Initially, a submerged water jet was simulated using a single-phase model. Then, the water jet was modelled as free using the Volume of Fluid (VOF) two-phase models. In particular, analyses were carried out to choose the turbulence model and the VOF modelling parameters. Finally, the sediments were injected and their Lagrangian trajectories were determined over the VOF solution previously calculated, under the assumption of one-way coupling regime. The statistics of the impacts of the sediments against the blade profile were analysed. The second test case consists in the evaluation of the hydro-abrasive wear over a single blade, assumed fixed. This required a 3D domain and higher computational burden. In order to calculate the erosion, the development of the sediment-laden jet and the particle-wall impact statistics were calculated.

It is then pointed out that in the three-dimensional case, special difficulties were encountered in mesh generation due to convergence and tetrahedra generation problems.

The choice of the turbulence model, namely $k - \varepsilon$ turbulence model and the choice of the interface modelling, namely sharp interface with no surface tension, were suited for the prediction of the erosion wear. Indeed, the choice of the turbulence model has an impact on the prediction of the turbulent kinetic energy, but just a minor influence on the Reynolds-averaged velocity field. As a result, the particle-wall impact statistics are substantially unaffected by the choice of the turbulence model.

In general terms, the results obtained in the two case studies are consistent with the basic physical processes and, up to a certain extent, comparable with reference solutions in the literature. The comparison was made with numerical cases from the literature because no experimental data were available. In addition, the comparison is only qualitative because all the information needed to reproduce the numerical cases was not available. In any case, the comparison is positive regarding the fluid velocity field and impact velocities, in fact they are similar from a qualitative point of view with the one of Leguizamon. On the other hand, differences from the thesis of Leguizamon were observed with regard to impact location and erosion estimation. However, considering all the elements that can explain these differences (e.g., the difference in the fluid dynamic model, differences in the geometry, differences in the boundary mesh), the result of the analysis can be considered satisfactory.

The results obtained in this thesis can be a starting point for future research. As a first recommendation, it would be important to overcome some problems encountered in particle tracking on fine meshes, as the generated .dpm file showed anomalies with respect to the analysed cases and with respect to the generated fluid field.

Then, effort could be directed towards approaching further the real engineering case. In particular, the motion of the blade could be accounted for by, firstly, imposing a fixed rotational speed. one can start with a two-dimensional case with a moving blade profile, then moving on to the three-dimensional blade case with constant rotation. The findings will be useful to understand whether the imposition of a constant rotation leads to significantly different results on blade erosion compared to the fixed blade case addressed here. This is necessary in order to understand whether the higher computational burden of the unsteady case is actually worthy for engineering purposes. As a matter of fact, setting up the unsteady case would require putting effort in defining the moving mesh and the unsteady particle tracking.

Another element that would be best investigated is the characterization of the erosion pattern since, the low impact angles mainly suggest an abrasion erosion mechanism rather than impact erosion.

Another analysis that can be performed is to vary the diameter of the particles impacting against the blade. In fact, in reality, the characteristics of these sediments are not exactly known, so it is crucial to understand the effect these factors have on blade erosion.

Bibliography

[1] O. E. Adedeji, L. Zhang, N. R. Sarker, D. E. Breakey, and R. S. Sanders. Characterization of the hydrodynamics within a toroid wear tester. *The Canadian Journal of Chemical Engineering*, 100(8):1941–1953, 2022.

[2] N. Adhikari, A. Pandey, A. Subedi, and N. Subedi. Design of pelton turbine and bucket surface using non-uniform rational basis spline and its analysis with computational fluid dynamics. *Journal of the Institute of Engineering*, 16(1):41–50, 2021.

[3] S. Bhattarai, P. Vichare, K. Dahal, A. Al Makky, and A. Olabi. Novel trends in modelling techniques of pelton turbine bucket for increased renewable energy production. *Renewable and Sustainable Energy Reviews*, 112:87–101, 2019.

[4] Z. Chongji, X. Yexiang, Z. Wei, Y. Yangyang, C. Lei, and W. Zhengwei. Pelton turbine needle erosion prediction based on 3d three-phase flow simulation. In *IOP Conference Series: Earth and Environmental Science*, volume 22, page 052019. IOP Publishing, 2014.

[5] X. Ge, J. Sun, Y. Zhou, J. Cai, H. Zhang, L. Zhang, M. Ding, C. Deng, M. Binama, and Y. Zheng. Experimental and numerical studies on opening and velocity influence on sediment erosion of pelton turbine buckets. *Renewable Energy*, 173:1040–1056, 2021.

[6] L. Han, G. Zhang, Y. Wang, and X. Wei. Investigation of erosion influence in distribution system and nozzle structure of pelton turbine. *Renewable Energy*, 178: 1119–1128, 2021.

[7] S. C. Leguizamón Sarmiento. *Multiscale Modeling and Simulation of Erosive Wear in Pelton Turbines*. PhD thesis, 2019.

[8] U. Manual. Ansys fluent 12.0. *Theory Guide*, 2009.

[9] H.-B. Matthias and O. Promper. *Numerical simulation of the free surface flow in Pelton turbines*. na, 2004.

[10] G. V. Messa and S. Malavasi. The effect of sub-models and parameterizations in the simulation of abrasive jet impingement tests. *Wear*, 370:59–72, 2017.

[11] G. V. Messa, S. Mandelli, and S. Malavasi. Hydro-abrasive erosion in pelton turbine injectors: A numerical study. *Renewable energy*, 130:474–488, 2019.

[12] M. Minozzo, R. Bergamin, M. Merelli, and M. Galbiati. Cfd study of a pelton turbine runner. *Comparison between Traditional Eulerian and Novel Lagrangian Approaches, Engisoft*, 2021.

[13] M. Padhy and R. Saini. Study of silt erosion mechanism in pelton turbine buckets. *Energy*, 39(1):286–293, 2012.

[14] M. K. Padhy and R. Saini. A review on silt erosion in hydro turbines. *Renewable and sustainable Energy reviews*, 12(7):1974–1987, 2008.

[15] A. Panagiotopoulos, A. Židonis, G. Aggidis, J. S. Anagnostopoulos, and D. Papantonis. Flow modeling in pelton turbines by an accurate eulerian and a fast lagrangian evaluation method. *International Journal of Rotating Machinery*, 2015, 2015.

[16] G. Panico. Modellazione euleriano-lagrangiana di flussi turbolenti liquido-solido con diversi regimi di accoppiamento tra le fasi. Master's thesis, Politecnico di Milano, 2020.

[17] A. Perrig, F. Avellan, J.-L. Kueny, M. Farhat, and E. Parkinson. Flow in a pelton turbine bucket: numerical and experimental investigations. 2006.

[18] A. Santolin, G. Cavazzini, G. Ardizzon, and G. Pavesi. Numerical investigation of the interaction between jet and bucket in a pelton turbine. *Proceedings of the Institution of Mechanical Engineers, Part A: Journal of Power and Energy*, 223(6):721–728, 2009.

[19] D. N. Veritas. Recommended practice rp o501 erosive wear in piping systems. *DNV Recommended Practice*, 4:1–43, 2007.

[20] C. Zeng, Y. Xiao, Y. Luo, J. Zhang, Z. Wang, H. Fan, and S.-H. Ahn. Hydraulic performance prediction of a prototype four-nozzle pelton turbine by entire flow path simulation. *Renewable Energy*, 125:270–282, 2018.

[21] A. Židonis, A. Panagiotopoulos, G. A. Aggidis, J. S. Anagnostopoulos, and D. E. Papantonis. Parametric optimisation of two pelton turbine runner designs using cfd. *Journal of Hydrodynamics, Ser. B*, 27(3):403–412, 2015.

A | Appendix A

Graphs paragraph 4.1.3 - Meshes for convergence analysis.
Here are reported all the meshes used for the convergence analysis.

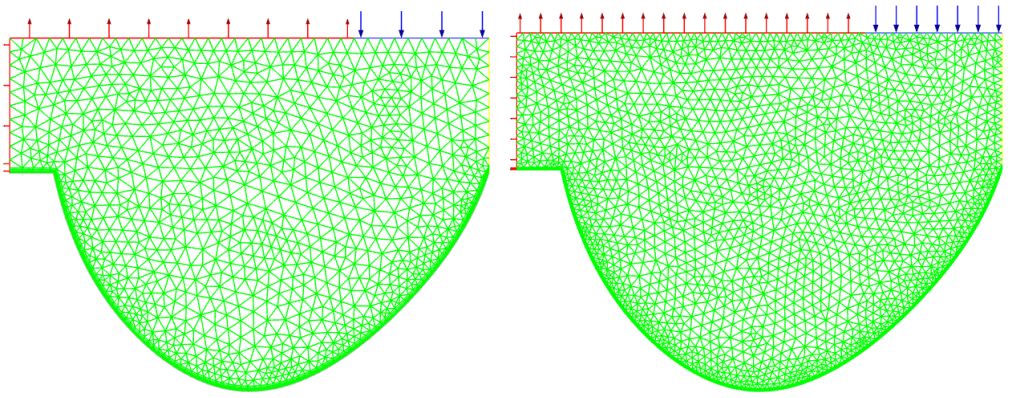

(a) N = 2381.

(b) N = 5039.

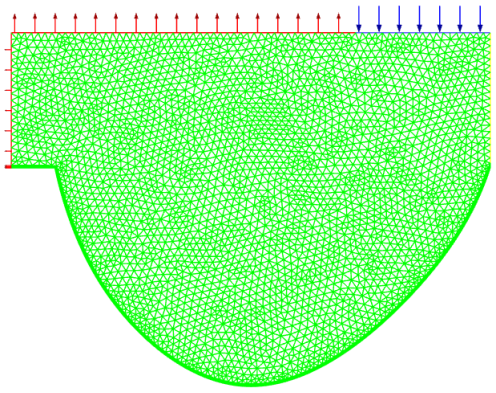

(c) N = 7619.

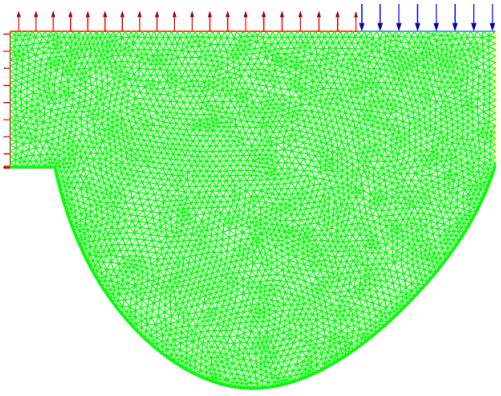

(d) N = 10099.

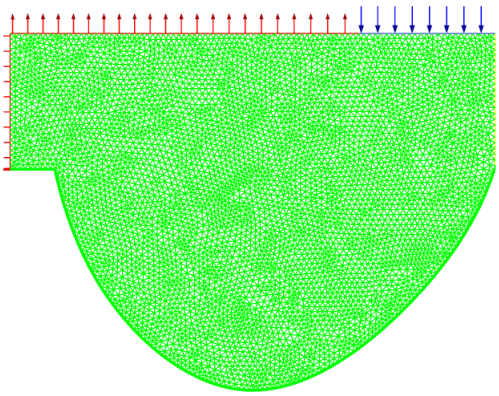

(e) N = 12565.

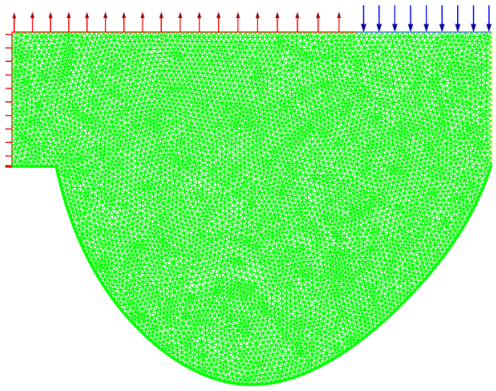

(f) N = 15082.

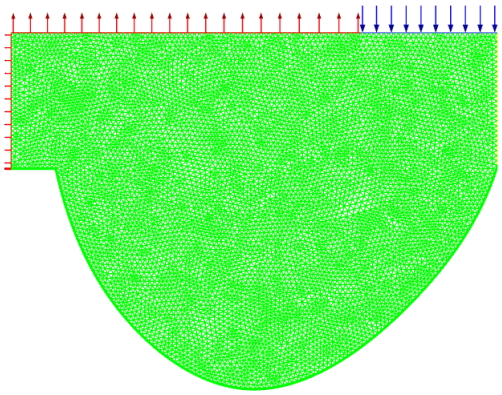

(g) N = 17586.

Graphs paragraph 4.1.4 - Sensitivity turbulence model analysis.
Here are reported the pictures of velocity magnitude and k along the n-axis of the blade considering Grid 4, 5, 6.

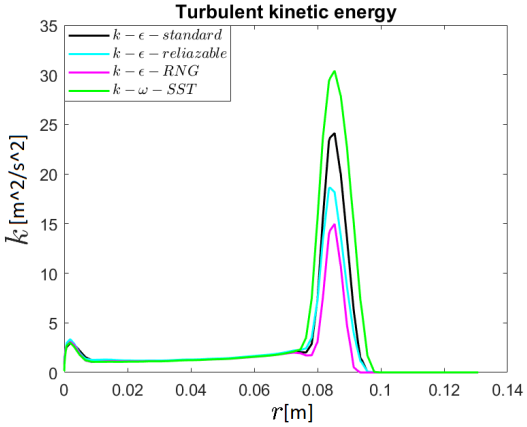

(h) Turbulence kinetic energy N = 10099.

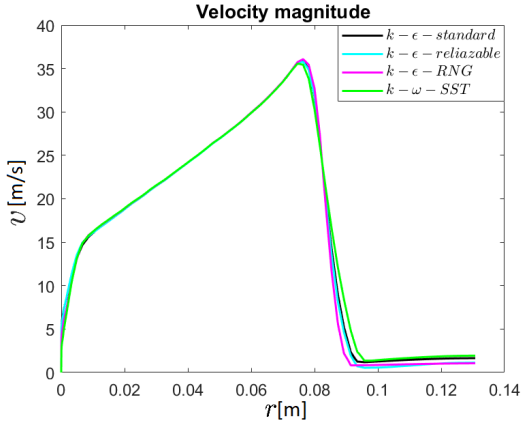

(i) Velocity magnitude N = 10099.

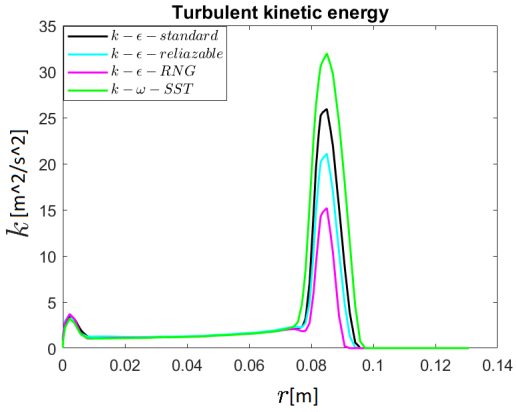

(j) Turbulence kinetic energy N = 12565.

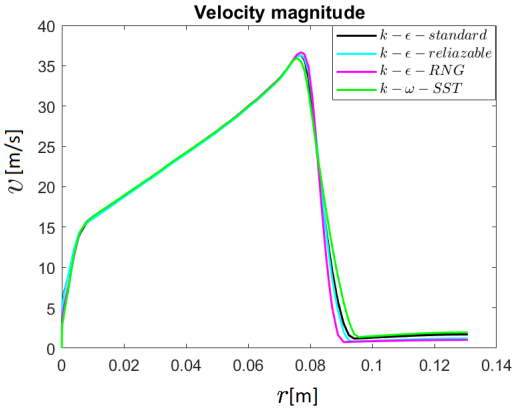

(k) Velocity magnitude N = 12565.

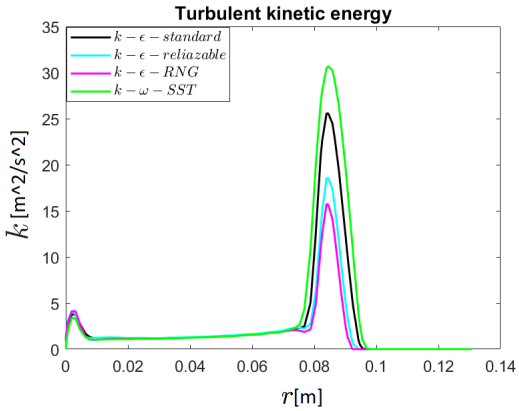

(l) Turbulence kinetic energy N = 15082.

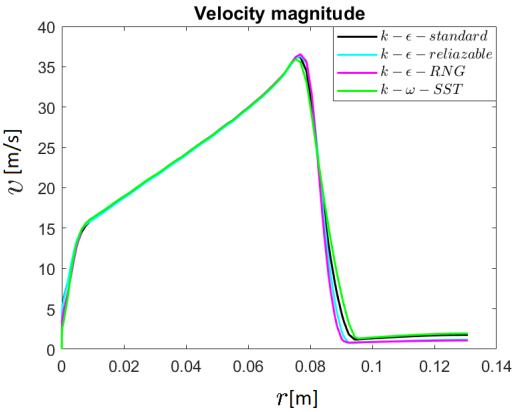

(m) Velocity magnitude N = 15082.

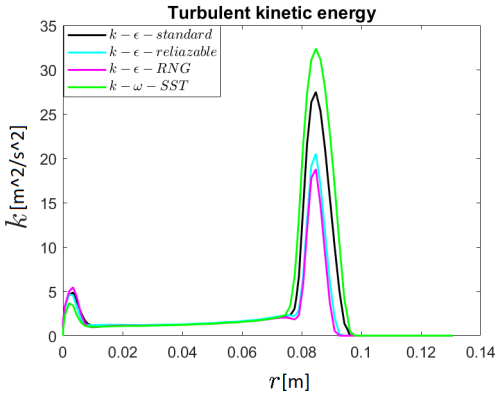

(n) Turbulence kinetic energy N = 17586.

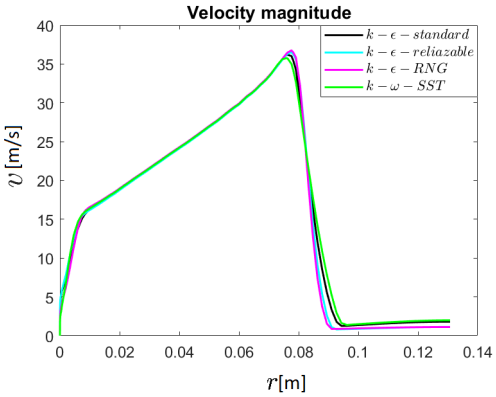

(o) Velocity magnitude N = 17586.

Graphs paragraph 4.2.4 - Sensitivity analysis w.r.t modelling parameters. Here are reported the velocity magnitude, Turbulent kinetic energy and volume fraction of the n-axis considering Grid 4, 5, 6 4.4 for both surface tension modelling comparison and interface modelling.

Surface tension modelling

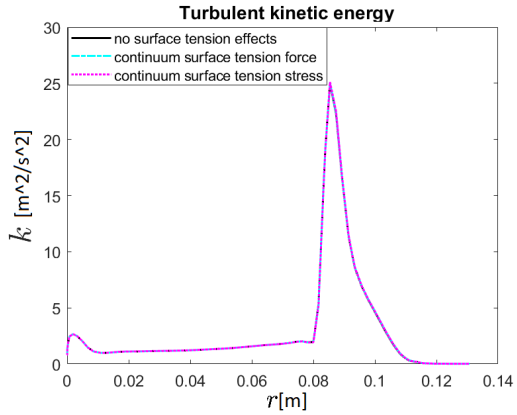

(a) Turbulence kinetic energy N = 10099.

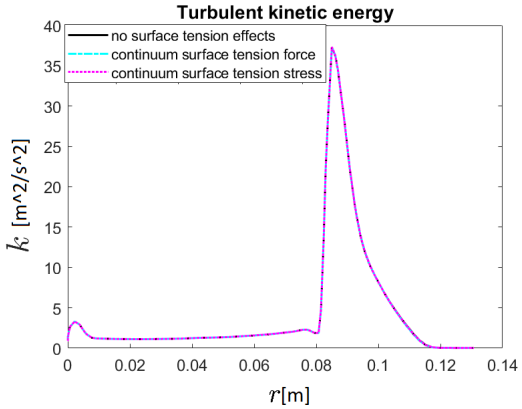

(b) Turbulence kinetic energy N = 12565.

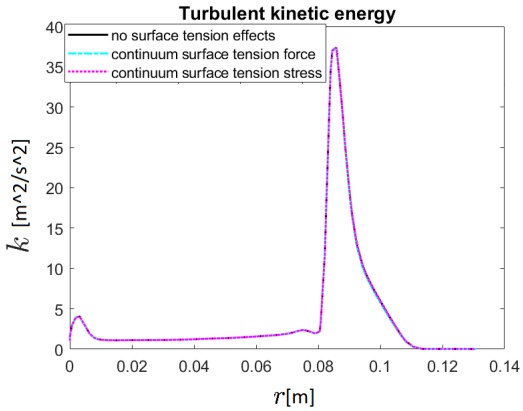

(c) Turbulence kinetic energy N = 15082.

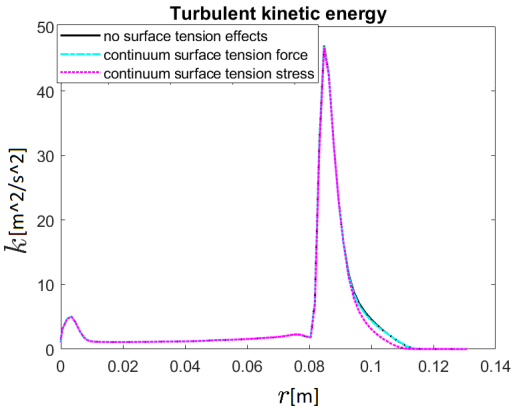

(d) Turbulence kinetic energy N = 17586.

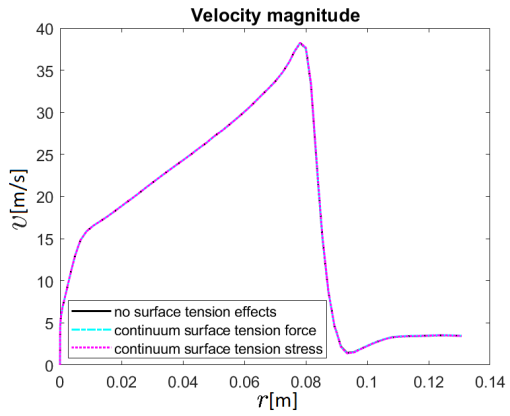

(e) Velocity Magnitude N = 10099.

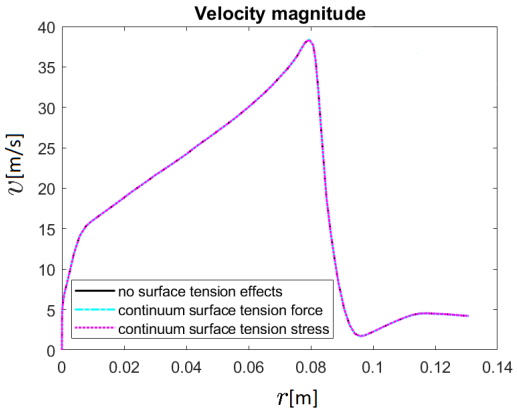

(f) Velocity Magnitude N = 12565.

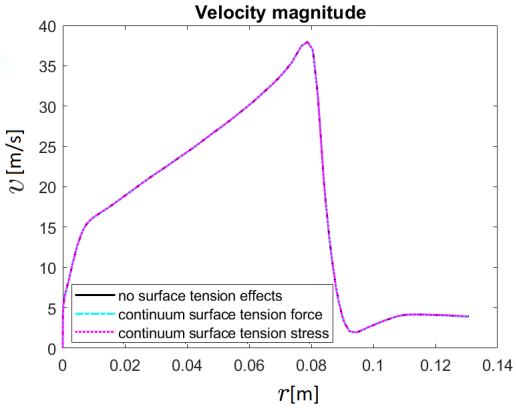

(g) Velocity Magnitude N = 15082.

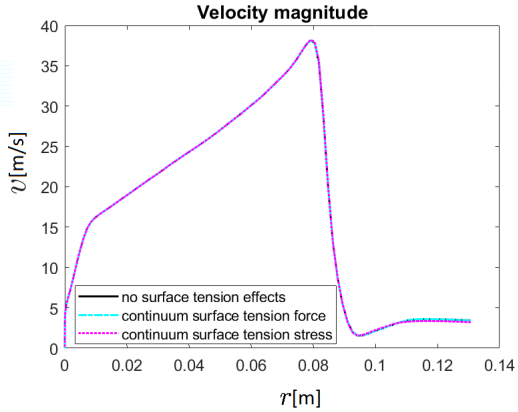

(h) Velocity Magnitude N = 17586.

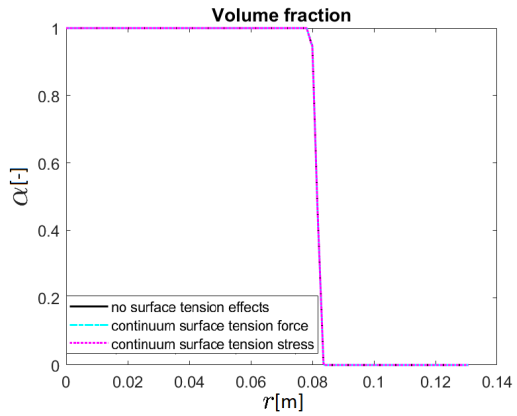

(i) Volume fraction N = 10099.

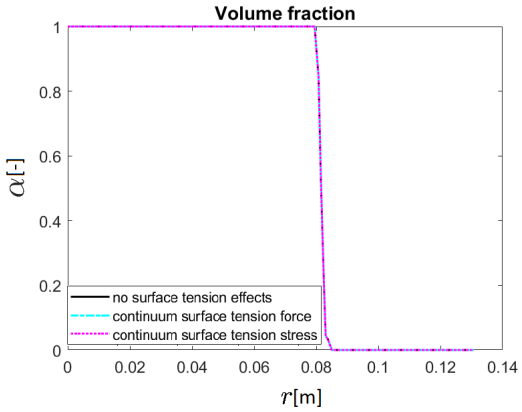

(j) Volume fraction N = 12565.

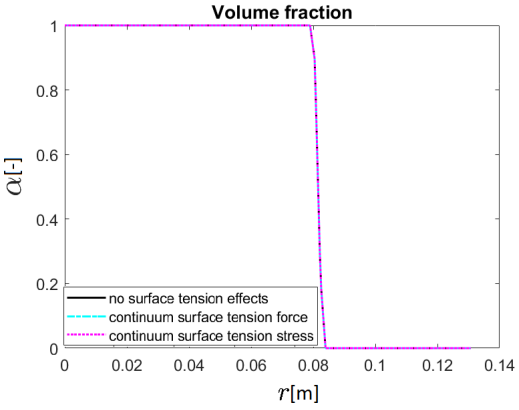

(k) Volume fraction N = 15082.

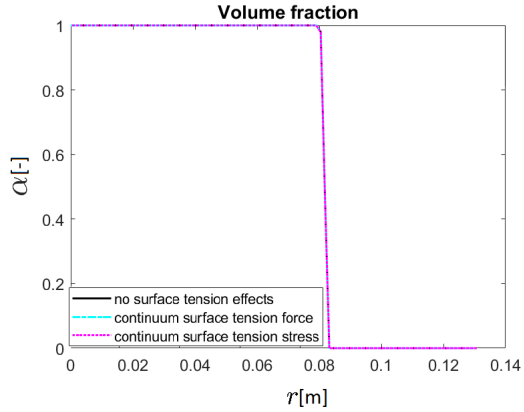

(l) Volume fraction N = 17586.

Interface modelling

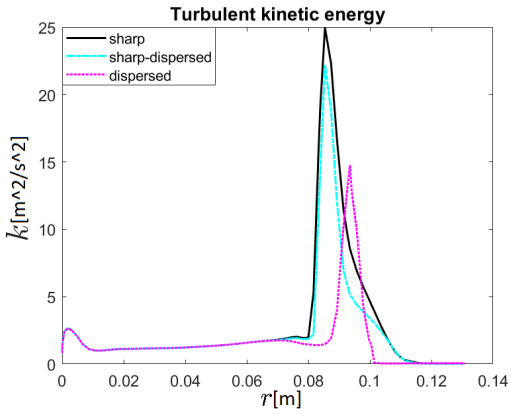

(m) Turbulence kinetic energy N = 10099.

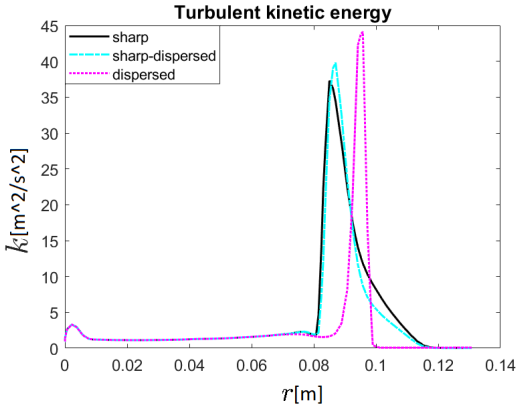

(n) Turbulence kinetic energy N = 12565.

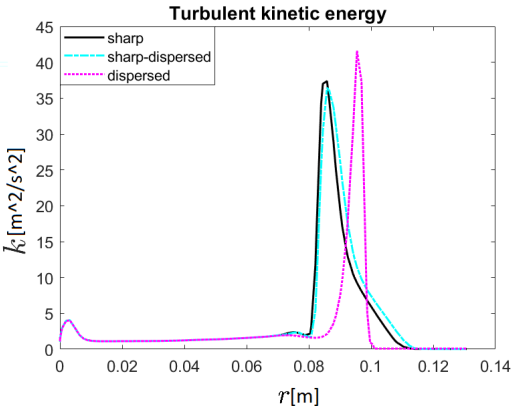

(o) Turbulence kinetic energy N = 15082.

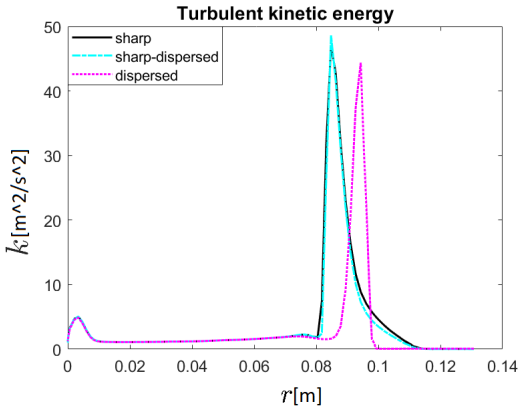

(p) Turbulence kinetic energy N = 17586.

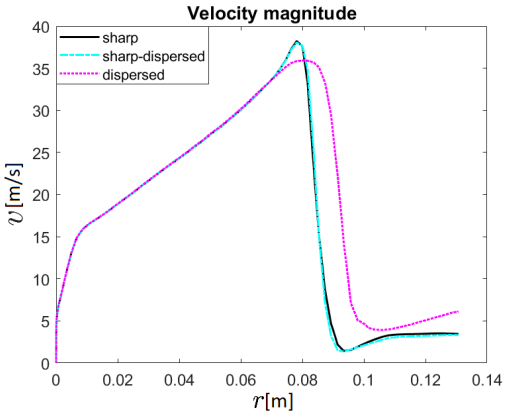

(q) Velocity Magnitude N = 10099.

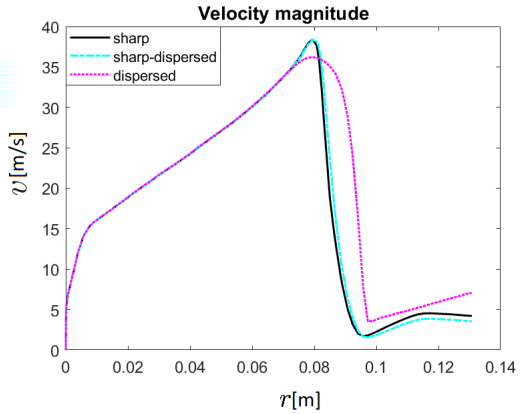

(r) Velocity Magnitude N = 12565.

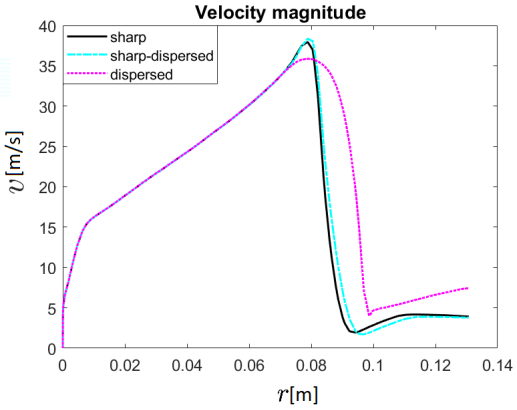

(s) Velocity Magnitude N = 15082.

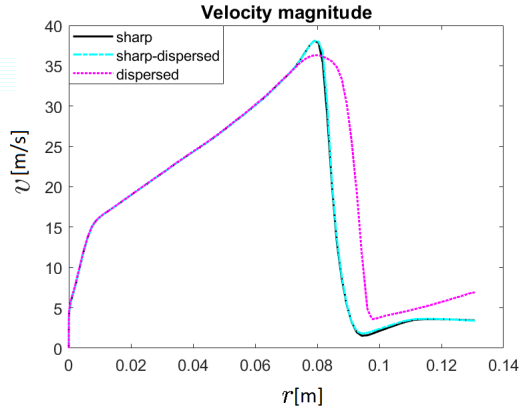

(t) Velocity Magnitude N = 17586.

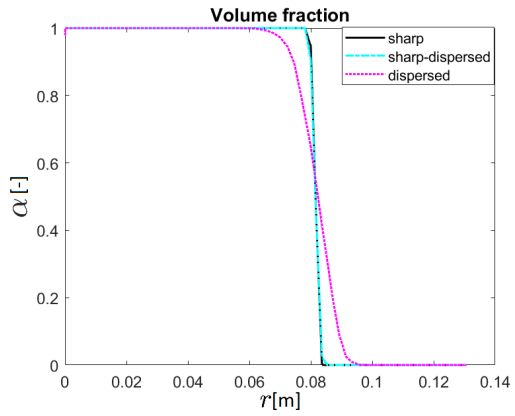

(u) Volume fraction N = 10099.

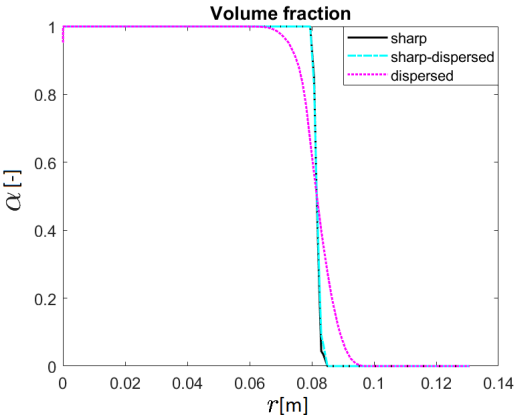

(v) Volume fraction N = 12565.

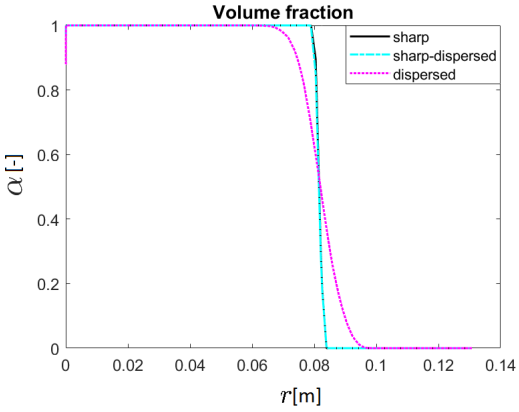

(w) Volume fraction N = 15082.

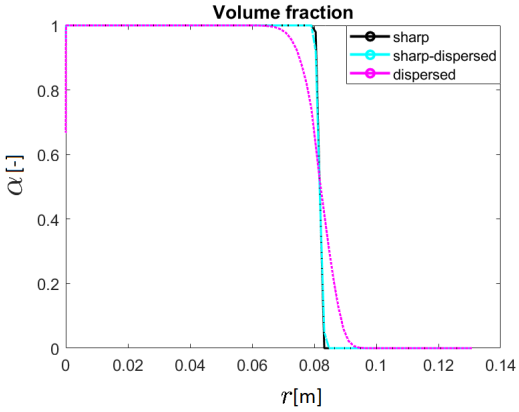

(x) Volume fraction N = 17586.

B | Appendix B

Graphs paragraph 4.3.1 - Steady particle tracking.

Here are reported the impact statistics obtained with the fourth grid for the steady particle tracking in the two-dimensional case.

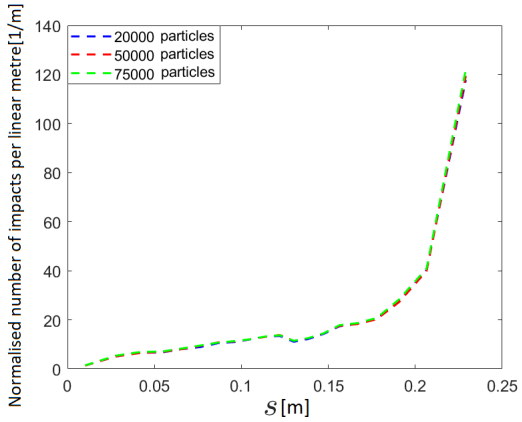

(a) Comparison of the number of impacts per linear metre normalised to the number of particles and the Δs.

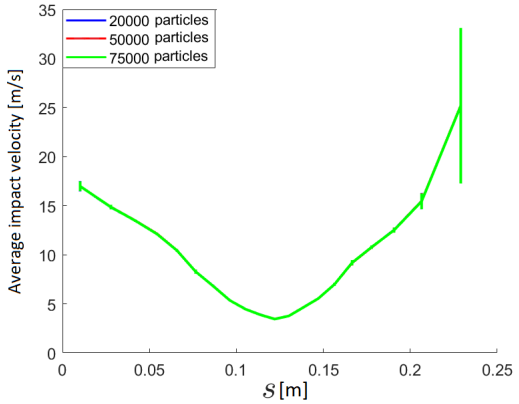

(b) Behaviour of the mean modulus of impact velocity along the target wall.

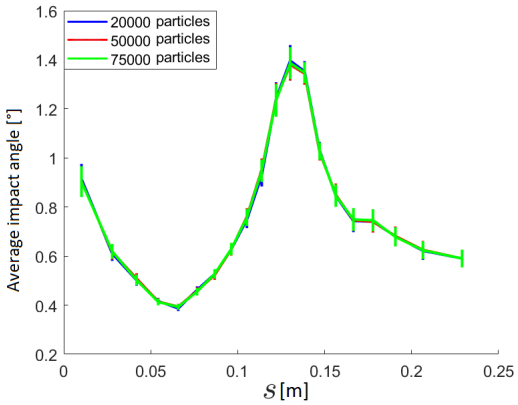

(c) Behaviour of the mean modulus of impact angle along the target wall.

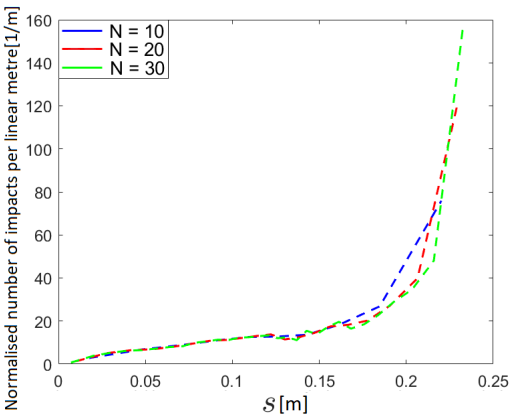

(d) Comparison of the number of impacts per linear metre normalised to the number of particles and the Δs.

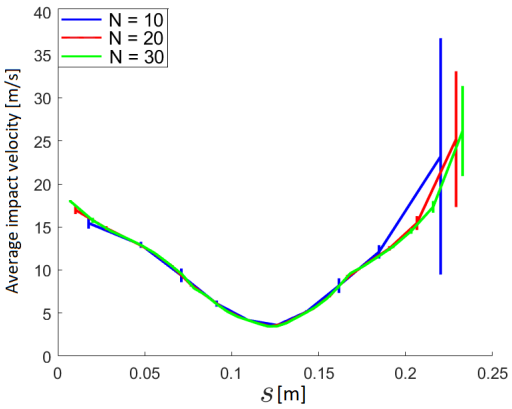

(e) Behaviour of the mean modulus of impact velocity along the target wall.

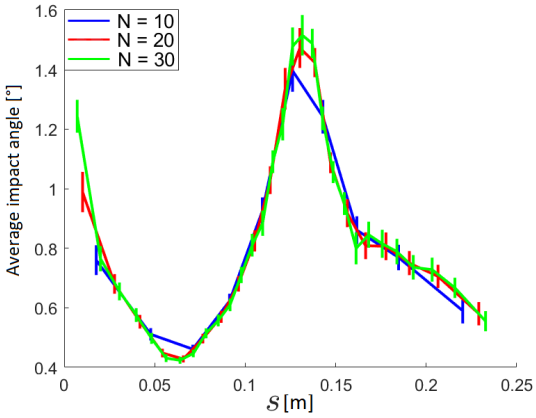

(f) Behaviour of the mean modulus of impact angle along the target wall.

Graphs paragraph 5.4.2 - Impact statistics.

Here are reported the impact statistics obtained with the with Grid 1 and Grid 3 for the erosion calculation with 100000 and 200000 particles.

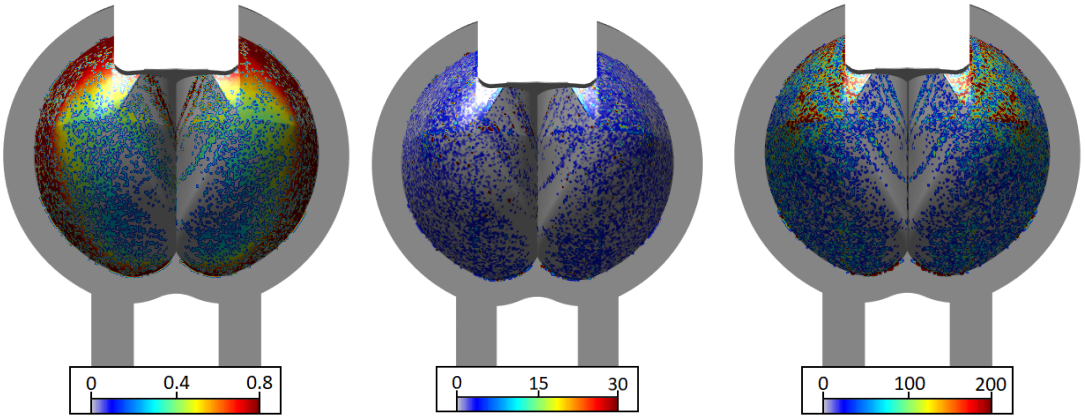

(g) Impact velocity normalized w.r.t the impact velocity

(h) Impact angle.

(i) Number of impact per cell.

Figure B.1: Impact statistics obtained with Grid 1 and 100000 particles.

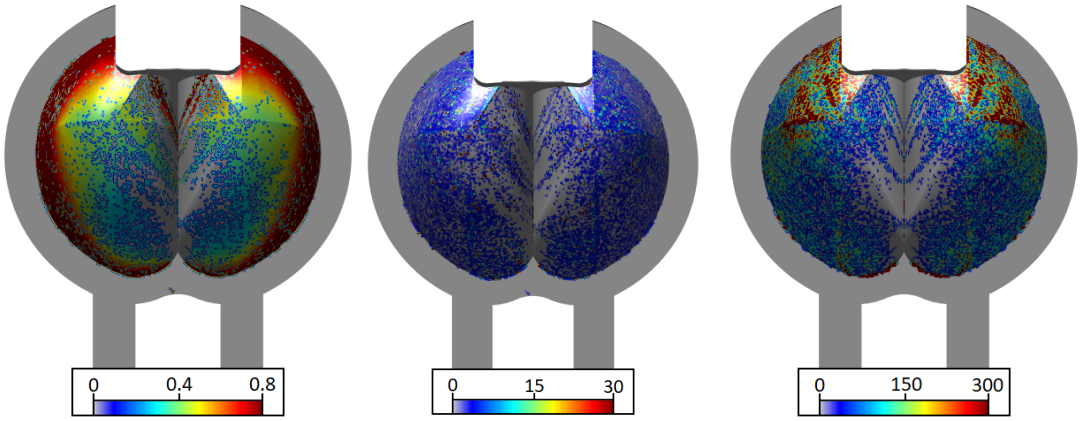

(a) Impact velocity normalized w.r.t the impact velocity

(b) Impact angle.

(c) Number of impact per cell.

Figure B.2: Impact statistics obtained with Grid 1 and 200000 particles.

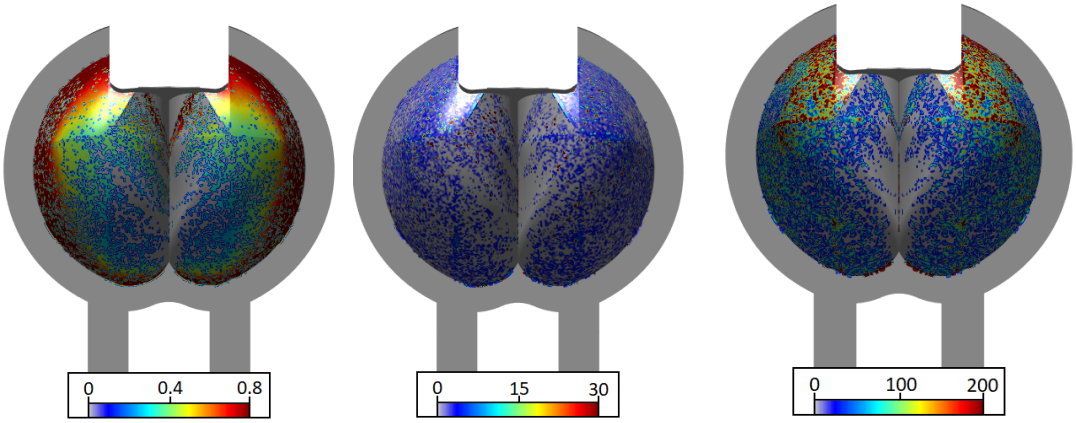

(a) Impact velocity normalized w.r.t the impact velocity (b) Impact angle. (c) Number of impact per cell.

Figure B.3: Impact statistics obtained with Grid 3 and 100000 particles.

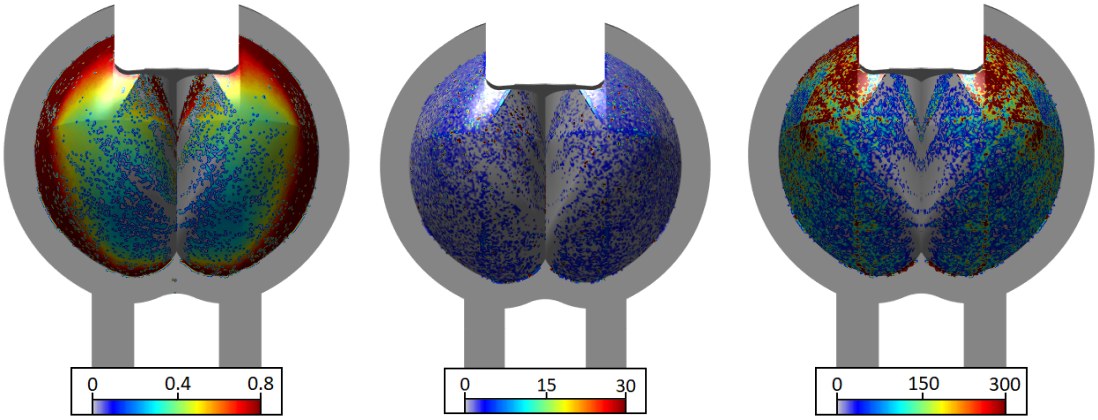

(a) Impact velocity normalized w.r.t the impact velocity (b) Impact angle. (c) Number of impact per cell.

Figure B.4: Impact statistics obtained with Grid 3 and 200000 particles.

List of Figures

1.1 Irena hydropower plant in Abu Dhabi (picture from irena.org). 2
1.2 Process of erosion of a Pelton turbine blade. Different jet velocities, silt sizes and concentrations are considered in the two cases. The blade is shown at different time instants (picture from Ge et al. [5]). 3
1.3 Examples of Pelton Turbines. 5
1.4 Pelton runner with one injector (picture from Leguizamon [7]). 6
1.5 Impact jet on the blades of a rotating turbine (picture from Leguizamon [7]). 7
1.6 An example of experimental setup for testing turbine erosion (picture from Ge et al. [5]). 9
1.7 Another example of experimental setup for testing turbine erosion (picture from Padhy [13]). 10

2.1 Shown on the right is the microscopic scale of the problem of particle impact causing surface erosion, which is solved with a solid mechanics model. On the left, the mascroscopic scale is shown where the flow of water with particles inside is represented, which is solved with a fluid-dynamic model. 14
2.2 Multi-scale nature of the hydro-abrasive wear of a Pelton turbine (picture from Leguizamon [7]). 15
2.3 Sediment-laden-river (picture from hydrosustainability.org). 16
2.4 Trajectories of sediments. In this Figure the variable under analysis is the particle residence time. 18
2.5 Micro-scale process of erosion. 20
2.6 Velocity and impact angle (adapted from Panico [16]). 20
2.7 Example of sediments with different size and shape (picture from nps.gov). 22

4.1 Sketch of the case study and relevant parameters. 32
4.2 Computational domain and boundary conditions. The blue boundary corresponds to the inlet, the red one to the outlet, the grey one to the wall and the yellow one to the symmetry. 34
4.3 Some simulation results obtained. 35

4.4 Exemplary meshes used in the convergence analysis. 37
4.5 Some results of the grid independence study. 38
4.6 Comparison turbulence. 40
4.7 Distribution of the turbulence intensity obtained in the present CFD simulations. 42
4.8 Distribution of the turbulence intensity as reported in the PhD thesis of Leguizamon [7]. 43
4.9 Velocity magnitude (picture from Adhikari et al. [2]). 44
4.10 Physical consistency VOF (results obtained with Grid 7). 50
4.11 Grid independence. 52
4.12 Comparison w.r.t. the surface tension modelling parameter. 54
4.13 Comparison w.r.t. the interface modelling parameter. 56
4.14 Turbulence intensity VOF. 57
4.15 Volume fraction (picture from Adhikari et al. [1]). 59
4.16 Particles trajectories. The variable under analysis is the particle residence time. 62
4.17 Comparison of the number of impacts per linear metre normalised to the number of particles and the Δs. 63
4.18 Behaviour of the mean modulus of impact velocity along the target wall. . 64
4.19 Behaviour of the mean impact angle along the target wall. 64
4.20 Comparison of the number of impacts per linear metre normalised to the number of particles and the Δs for different numbers of tracked parcel. . . 66
4.21 Behaviour of the mean modulus of impact velocity along the target wall for different numbers of tracked parcel. 67
4.22 Behaviour of the mean impact angle along the target wall. 67
4.23 Comparison of the number of impacts per linear metre normalised to the number of particles and the Δs for different numbers of tracked parcel. . . 69
4.24 Behaviour of the mean modulus of impact velocity along the target wall for different numbers of tracked parcel. 69
4.25 Behaviour of the mean impact angle along the target wall for different numbers of tracked parcel. 70

5.1 Picture from the PhD thesis of Leguizamon [7] representing the blade geometry in his case study. 74
5.2 Impeller. 75
5.3 Blade with the cylinder of the injection of water. 77
5.4 Computational domain of the 3D Pelton blade. 78

5.5 Boundary conditions of the 3D domain: the blue boundary corresponds to the inlet, the red boundary to the outlet, the grey boundary to the wall. . 78
5.6 Boundary mesh. 79
5.7 3D: Physical consistency VOF 80
5.8 Parameters for studying grid independence with Grid 2. 81
5.9 Erosion rate and penetration rate, computed with 300000 particles with Grid 2. 82
5.10 Grid 2. 84
5.11 Parameters for studying grid independence with Grid 1. 85
5.12 Parameters for studying grid independence with Grid 3. 85
5.13 Impact statistics obtained with Grid 2 and 100000 particles. 86
5.14 Impact statistics obtained with Grid 2 and 200000 particles. 86
5.15 Erosion rate and penetration rate, computed with 300000 particles with Grid 1. 87
5.16 Erosion rate and penetration rate, computed with 300000 particles with Grid 3. 88
5.17 Water jet hitting the bucket colored by the velocity magnitude, as reported in Leguizamon [7]. 89
5.18 Particle-wall impact angles and dimensionless particle-wall impact velocities over the surface of the blade, as reported in Leguizamon [7]. 90
5.19 Eroded mass over each surface element, as reported Leguizamon [7]. 90

B.1 Impact statistics obtained with Grid 1 and 100000 particles. 111
B.2 Impact statistics obtained with Grid 1 and 200000 particles. 111
B.3 Impact statistics obtained with Grid 3 and 100000 particles. 112
B.4 Impact statistics obtained with Grid 3 and 200000 particles. 112

List of Tables

4.1 Geometric parameters case 1. 32
4.2 Characteristics of the meshes used in the grid independence study. 36
4.3 Geometric parameters from [2]. 45
4.4 Number of subdivisions with the corresponding Δs. 68

5.1 Geometric and flow conditions from the PhD thesis by Leguizamon [7] . . . 74
5.2 Number of cells in each computational grid. 83

List of Symbols

Latin characters

Variable	Description	SI unit
B_2	Maximum internal width of a Pelton bucket	[m]
B_3	Bucket depth	[m]
C	Sediment concentration	[$\%_w$]
C_1	Absolute jet velocity	[m/s]
$C_{1\varepsilon}$	Turbulence model parameter	[-]
$C_{2\varepsilon}$	Turbulence model parameter	[-]
C_μ	Turbulence model parameter	[-]
C_d	Drag coefficient	[-]
d	Particle size	[m]
$\bar{\bar{D}}$	Strain rate tensor	[s^{-1}]
D_0	Jet diameter	[m]
D_1	Pitch diameter of a Pelton runner	[m]
e_r	Erosion ratio	[mg/kg]
$\vec{F}$	Surface tension force	[N]
$\vec{F}_{pr}$	Pressure gradient force	[N]
g	Gravitational acceleration	[m/s^2]
k	Turbulence kinetic energy	[m^2/s^2]
L_j	Jet Length	[m]
m_p	Particle mass	[kg]
$\dot{M}_p$	Mass flow rate	[kg/s]
N_p	Number of particles	[-]
P	Averaged pressure field	[Pa]
T	Time	[s]

Δs	Rectangle length in wall	[m]
x_{imp}	x-position of the impact	[m]
y_{imp}	y-position of the impact	[m]
z_{imp}	z-position of the impact	[m]
U_{imp}	Impact velocity	[m/s]
v	Velocity magnitude	[m/s]
$\vec{v}$	Fluid velocity	[m/s]
$\vec{v}_p$	Particle velocity	[m/s]
$\vec{V}$	Averaged velocity vector field	[m/s]
W_p	Particle volume	[m^3]
z_0	Number of jets	[-]
z_b	Number of buckets	[-]

Greek characters

Variable	Description	SI unit
α	Volume fraction	[-]
α_q	Volume fraction of fluid q	[-]
$\phi^{\bar{\bar{R}}e}$	Reynolds stresses tensor	[m]
ε	Dissipation rate of turbulence kinetic energy	[m^2/s^{-3}]
σ_k	Turbulence model parameter	[-]
σ_ε	Turbulence model parameter	[Pa s]
ρ	Density	[kg/m^3]
θ_{imp}	Impact angle	[°]
μ	Dynamic viscosity	[Pa s]
μ_{turb}	Turbulent viscosity	[Pa s]
ν	Poisson coefficient	[-]
ν_{turb}	Cinematic turbulence viscosity	[kg/ms]

Acronyms

CFD	Computational Fluid Dynamics
CSM	Computational Solid Mechanics
DPM	Discrete Phase Modelling
VOF	Volume of Fluid

Acknowledgements

Desidero esprimere i miei più sinceri ringraziamenti a tutte le persone che mi hanno sostenuto durante questi anni, contribuendo in modo significativo al compimento del mio percorso accademico.

Innanizitutto vorrei ringraziare i miei genitori che mi hanno sempre sostenuta credendo in me, ma soprattutto crescendomi forte e determinata affinchè riuscissi a raggiungere tutti i traguardi che mi ero prefissata.

Ringrazio mia sorella Elena che mi ha supportata, motivata, credendo in me più di quanto facessi io.

Ringrazio mio cugino Davide che ha contribuito alla realizzazione del mio percorso facendomi vivere momenti di leggerezza e divertimento.

Ringrazio mia cugina Giorgia, le mie zie e i miei nonni per essermi stati vicino.

Ringrazio Giulia, Alessia, Sophia, Camilla e Vanessa per essere le migliori compagne di danza che potessi avere.

Ringrazio i miei compagni di università Elisabetta, Lara, Lorenzo, Jacopo, Alberto, Roberto, Roberto, Velentina, Luca, Valentina

Giuseppe e Federico. Ognuno di voi ha fatto parte del mio percorso e vi ringrazio per aver condiviso questi bellissimi anni.

Un sentito grazie anche al mio relatore, che mi ha dedicato il suo tempo e la sua competenza per aiutarmi a sviluppare il mio lavoro.